MULTIPHOTON PROCESSES FOR HIGH-SPEED OPTICAL DIAGNOSTICS

by

David Shekhtman

A DISSERTATION

Submitted to the Faculty of the Stevens Institute of Technology
in partial fulfillment of the requirements for the degree of

DOCTOR OF PHILOSOPHY

David Shekhtman, Candidate

ADVISORY COMMITTEE

Nicholaus J. Parziale, Chairperson Date

Kevin Connington Date

Vladimir Lukic Date

Jason Rabinovitch Date

Hamid Hadim Date

STEVENS INSTITUTE OF TECHNOLOGY
Castle Point on Hudson
Hoboken, NJ 07030
2022

MULTIPHOTON PROCESSES FOR HIGH-SPEED OPTICAL DIAGNOSTICS

ABSTRACT

Non-intrusive flow diagnostic techniques are applied in the hypersonic flow regime, due to their fast response time, low influence on flow, and off-surface measurement capability. The means for studying high speed, high enthalpy flow, using Krypton Tagging Velocimetry (KTV), are explored and developed. Using KTV, a test campaign was conducted in the freestream of the T5 Caltech Piston-Driven Reflected-Shock Tunnel. Major efforts were made to (1) optimize the signal-to-noise ratio (SNR) of emitting, tagged Kr atoms and (2) minimize image-processing difficulties of tagged features due to background noise, flow luminosity, and laser-induced wall ablation on test articles. Additionally, a hollow-cylinder flare was designed for future KTV work, which will take advantage of the SNR optimization and image-processing techniques developed herein.

Author: David Shekhtman

Advisor: Nicholaus J. Parziale

Date: April 29, 2022

Department: Mechanical Engineering

Degree: Doctor of Philosophy

This thesis is dedicated to my entire family (my mother, my father, my sister Rachel , and my cousin Dan) and the entire lab (which consists of Ahsan Hameed, Ammar M. Mustafa, Roshan, Alex Dworzanczyk, Ben Segall, and my advisor Professor Parziale). Many innovative ideas were inspired by being around these great people. My family and colleagues gave me invaluable support during the dark days of my research, which included paper rejections, parts not fitting together, late parts, and a pandemic; and they celebrated with me the finer moments, such as the commissioning of the Stevens Shock Tunnel, paper acceptances, and functioning equations stretching across the page. In particular, I am grateful to my advisor, who gave me tools and patience to solve mind-boggling problems and mature as a researcher and a person. I am also thankful for the stronger sense of identity and inner peace, which the Stevens Doctoral program has helped me achieve.

Acknowledgments

I would like to aknowledge the support of my advisor Nick Parziale and my family, who both held a lantern through tough times. I also acknowledge the funding support of ONR grants N00014-19-1-2523, N00014-20-1-2549, and N00014-20-1-2637 for which Eric Marineau is program manager. I am also thankful to Professor Lukic for introducing me to perturbation theory and to Professor Connington for showing me the advantages of power method techniques for finding eigenvalues in sparse, poorly conditioned, rank deficient linear systems. I am grateful to Wesley Yu and Professor Austin for their collaboration in the T5 Caltech KTV campaign.

Table of Contents

List of Tables

List of Figures

Chapter 1
Introduction

Hypersonics is the crossroads of many physical disciplines, such as compressible fluid dynamics, statistical mechanics, atomic physics, plasma physics, non-equilibrium thermodynamics, and fundamental physics [1]. Our understanding of the hypersonic flow regime remains incomplete due to the abundance, complexity, and interaction of different physical phenomena, which can have serious effects on the flow fields over hypersonic vehicles. According to Anderson [1], the hypersonic regime for a gas flow is characterized by high Mach number, the occurrence of chemical reactions, and/or the excitation of molecular and atomic degrees of freedom of different gas species. Additionally, new instabilities, such as the second-mode instability, can become the dominant mechanism for transition to turbulence [2–4].

Our understanding of flow physics in the hypersonics flow regime is incomplete. Traditional computational fluid dynamics (CFD) codes have difficulty predicting flow structures and heat-transfer rates over test articles in hypersonic wind tunnels [5], particularly in the wall-layer regions, separated regions, and shock-wave-boundary-layer interaction regions. For example, artificial viscosity, a necessary numerical tool used to stabilize CFD codes, can influence the fidelity of a transient flow simulation [6]. Additionally, RANS turbulence models average out dynamics of the Navier-Stokes Equations [7], which means they may not accurately predict all parameters in complicated flows, such as separated regions.

Knowledge of the hypersonic regime is important for vehicle design, which demands having more complete transition and turbulence models. Ground-test facilities, such as impulse facilities, attempt to fill this knowledge gap by allowing researchers

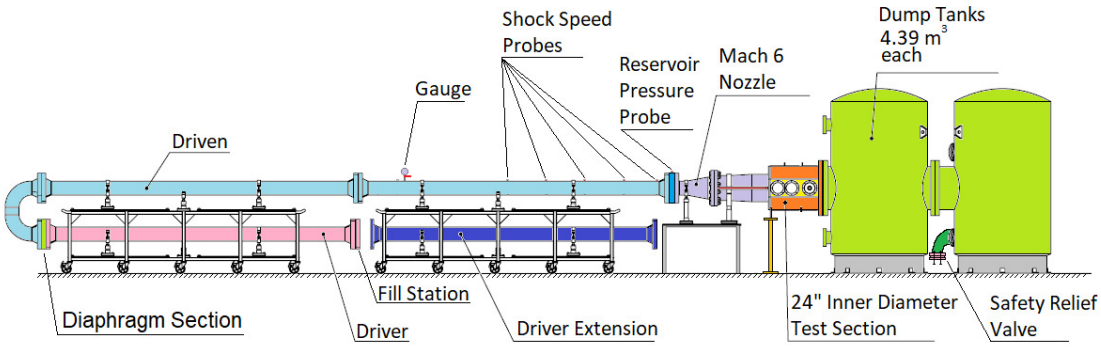

Figure 1.1: Schematic of Stevens Shock Tunnel.

to replicate hypersonic flight-conditions in a laboratory setting. Shock tunnels generate high speed, high enthalpy flow for millisecond test times [8, Ch. 16]. Different facilities exist to simulate different flow conditions: flight enthalpy, Reynolds number, speed, Mach number, and freestream pressure [9–12]. One such tunnel currently resides in the Stevens Institute of Technology: the Stevens Shock Tunnel, as shown in Fig. 1.1. This tunnel generates free flight conditions for high-speed vehicles [13]. It primarily consists of a shock tube whose reflected shock region establishes a reservoir for a nozzle, which expands high temperature gas into a test section at Mach 5.8 - 6.0 and unit Reynolds number 0.35 - 8.1 $\times$ 10^6 m^{-1}.

The test section of a typical hypersonic tunnel, such as the one in 1.1, offers optical access to non-intrusively probe hypersonic flow. There exist numerous non-intrusive flow diagnostic techniques that can yield freestream Mach number, freestream temperature, velocity profiles, shock angles, and even the frequency content of these quantities. These techniques include schlieren photography [14], laser-induced schliere anemometry [15], laser-induced-fluorescence (LIF), planar-laser-induced-fluorescence (PLIF), laser absorption spectroscopy (LAS), molecular-tagging-velocimetry (MTV), atomic-tagging-velocimetry (ATV), and Focused Laser Differential Interferometry (FLDI) [12, 16–18]. Non-intrusive, off-surface experimen-

tal techniques minimally interfere with a flow and have fast response times. Hence they are (1) excellent in evaluating the performance of a CFD code on canonical flows and (2) useful for preparing new computational flow models. The information they provide complements surface measurements.

MTV and ATV are attractive applications of laser-induced-fluorescence, which rely on vibrational, rotational, or electronic excitation of tracer species. Unlike Laser Doppler Velocimetry (LDV) and Particle Image Velocimetry (PIV) [8], which have insufficient particle response times in shock tunnels due to high Knudsen number[1] MTV and ATV are attractive applications of laser-induced-fluorescence, which rely on vibrational, rotational, or electronic excitation of tracer species. Unlike Laser Doppler Velocimetry (LDV) and Particle Image Velocimetry (PIV) [8], which have insufficient particle response times in shock tunnels due to high Knudsen number and hence slip in low density flow [20–23], MTV and ATV are not limited by timing issues associated with tracer injection or reduced particle response due to the small inertia and size of tracer particles. Methods of tagging velocimetry include krypton tagging velocimetry (KTV) [24–33], VENOM [34–38], APART [39–41], RELIEF [42–46], FLEET [47, 48], STARFLEET [49], PLEET [50], argon [51], iodine [52, 53], sodium [54], acetone [55–57], NH [58] and the hydroxyl group techniques [59–62], among others [63–68].

Researchers have applied various velocimetry techniques to impulse facilities.

[1]The Knudsen number is $Kn = \frac{\lambda}{L}$, where λ is the mean free path and L is the length scale of the flow [7]. For a spherical particle of diameter D in a gas, $L = D$ and $\lambda = \frac{1}{\sigma_o \frac{N}{V}}$. From statistical mechanics [19], the viscosity of a gas is $\mu = \frac{1}{\sigma_o}\sqrt{\frac{mk_bT}{\pi}}$, where T is the gas temperature, m is the mass of a gas molecule, k_b is the Boltzmann constant, and σ_o is the collision cross-section in the gas. From this definition of viscosity and assuming an ideal gas $\frac{N}{V} = \frac{P}{k_bT}$, Knudsen number is calculated as $Kn = \frac{\mu}{DP}\sqrt{\frac{\pi RT}{2}}$.

McIntosh [69] used spark tracer and magnetohydrodynamic methods to measure the velocity of the gas in the freestream of a high-enthalpy shock tunnel; the measurements have large uncertainty and require a complex experimental setup. Wagner et al. [70] used PIV to measure the impulsively started flow over a cylinder in a shock tube. Parker et al. [71] used a line-of-sight-integrating method to measure freestream velocity via nitric oxide (NO) tagging in the CUBRC LENS I facility. Danehy et al. [72] used NO as a tracer to measure shear flows in the T2 and T3 reflected-shock tunnels; those measurements used a mixture of approximately 97-99% N2 and 1-3% O2 in the driven section to "produce an amount of NO sufficient to produce good fluorescence but that would minimize the amount of the gases (O_2, O, and NO) that are efficient quenchers." de S. Matos et al. [73] made velocity measurements in unseeded hypersonic air flows in a reflected-shock tunnel at an enthalpy of approximately 6 MJ/kg. Their work presents a strategy where a reference image was taken before the test, which is not possible in some impulse facilities due to vibration.

Krypton Tagging Velocimetry is a recent velocimetry technique, being among several possible existing multiphoton noble gas velocimetry techniques, such as argon tagging velocimetry [51, 74] and potentially xenon tagging velocimetry [75]. Unlike tracers like nitric oxide, hydroxyl, and acetone, noble gases are chemically stable, noncorrosive, and nontoxic. Of the commercially available noble gases, krypton was selected because it has the second lowest ionization energy [76, Chapter 18]. Presently, there are three strategies to krypton tagging: (a) generation and excitation of the krypton metastable state, (b) resonant-enhanced-multiphoton-ionization (REMPI), and (c) a combination of approaches a and b. The use of a metastable noble gas as a tagging velocimetry tracer was first suggested by Mills et al. [77] and Balla and Everheart [78]. In experimental schemes relying on krypton metastable state excitation, a pulsed dye-laser was used perform the write step at 214.769 nm to form a write

line and photosynthesize the metastable Kr tracer; and after a prescribed delay, an additional pulsed dye-laser was used to re-excite the metastable Kr tracer at 760.2 nm to track displacement. Two-laser KTV has been successfully demonstrated for 1) an underexpanded jet (the first KTV demonstration) [24]; 2) mean and fluctuating turbulent boundary-layer profiles in a Mach 2.7 flow [25]; 3) seven simultaneous profiles of streamwise velocity and velocity fluctuations in a Mach 2.8 shock-wave/turbulent boundary-layer interaction [26]; 4) the freestream of the large-scale AEDC Hypervelocity Tunnel 9 at Mach 10 and Mach 14 [28]; and 5) Mach 2.8 shock-wave/turbulent boundary-layer interactions over 8°, 16°, 24° and 32° wedges [79].

Recently, (2+1) REMPI has been used to excite krypton via two-photon excitation and subsequently ionize the resulting excited Kr species via one-photon ionization. For nanosecond excitation at intensities of order 10^{11-14} W/cm^2, (2+1) REMPI dominates [80, 81]. (2+1) REMPI has resulted in simplified KTV schemes, which use a single laser to produce write lines and can also use a laser diode to re-excite the krypton metastable state generated from recombination and decay processes to increase the signal strength of the fluorescence lines. Such KTV schemes have been demonstrated in an underexpanded jet configuration [30], flow following the incident shock in a shock tube [32], and freestream flow in the T5 Reflected-Shock Tunnel at Caltech [82]. KTV has been used to characterize canonical flows over fundamental geometries, such as supersonic, turbulent flows over a flat plate [25], a wedge [79], and a hollow-cylinder [83].

The successes of KTV aroused interest in the optimization of its laser excitation schemes: single-laser, dual-laser, and diode-assisted laser schemes. Longer fluorescence lifetimes and more reliable Kr fluorescence are desired. Ch. 2 attempts to address these interests. In single-laser and write-laser-dominated excitation schemes, large intensities on the order of 10^{11} W/cm^2 are used with laser fluences on the order

of 1 - 10 J/cm^2 on a test article surface. Resulting laser ablation plumes obscured the camera field of view and decreased near-wall resolution of the KTV signal. In Chapters 3 and 4, new KTV schemes and methods resulted in unorthodox ablation mitigation methods as byproducts of research; and more importantly, these schemes demonstrated the use of KTV in high speed flow generated in impulse facilities. Ch. 4 demonstrates the implementation of KTV in high speed, high enthalpy flow in the T5 Caltech Reflected-Shock Tunnel. In Appendix C, several wall-ablation mitigation solutions are proposed, tailored to the needs of krypton tagging velocimetry. Ch. 5 proposes the next major KTV project: probing the flow over a hollow-cylinder-flare. In Ch. 6, the benchmark results of this work for KTV are listed, and future KTV development and applications are discussed.

Three peer-reviewed journal articles ([33, 82, 83]) were written during the course of this work, forming the backbone of Chapters 2, 3, and 4, respectively. In each of these chapters, additional supporting material is presented to further demonstrate the capabilities of KTV.

Chapter 2

Current State of Krypton Tagging Velocimetry

Krypton Tagging Velocimetry (KTV) is a time-of-flight flow visualization technique that has shown great promise in nonintrusive hypersonic flow diagnostics. When compared to macroscopic flow visualization particles, Kr atoms with their low inertia and small size provide more accurate tracking of high speed flow that incorporates shocks and large flow discontinuities. The chemical inertness of Kr [84] is advantageous for observing chemically reacting flow in high-speed air. Kr tagging allows an experimentalist to track flow velocity and flow structure. The development of KTV rests on excitation techniques and technology; the experimental setup for a test article; and the ground-test facility characteristics (which include background noise, flow luminosity, suspended particulate). This thesis explores these KTV design requirements and factors to increase the maturity of the technique. In this chapter, line optimization is conducted for single-laser KTV and a 769.45 nm continuous-wave (CW) diode-assisted scheme. In Section 2.1, theoretical two-photon excitation cross-sections are calculated via first-order perturbation theory to determine an optimal single-laser excitation line and understand underlying physics that could be used to improve future excitation schemes for Kr and other noble gases. In Section 2.5, experimental fluorescence data for the diode-assisted scheme are mapped to a pressure-time parameter space for different excitation lines and are used in the selection of a line for KTV in the T5 Piston-driven Reflected-Shock Tunnel (Ch. 4).

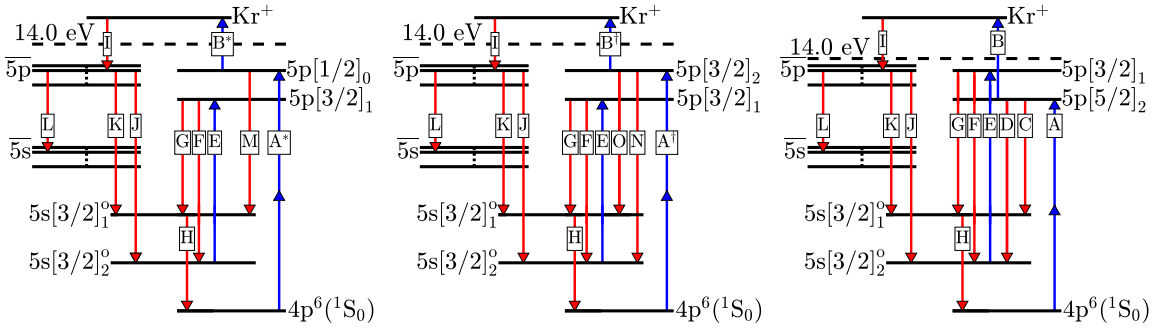

(a) 212.556 nm Excitation (b) 214.769 nm Excitation (c) 216.667 nm Excitation

Figure 2.1: Energy diagrams (not to scale) with Racah nl[K]$_J$ notation for the three excitation schemes. (a) 212.556 nm. (b) 214.769 nm. (c) 216.667 nm. Transition details are in Table 2.1. States $\overline{5p}$ and $\overline{5s}$ represent the numerous 5p and 5s states (tabulated in Mustafa et al. [32]) that are created by the recombination process, I. Transitions J, K and L represent the numerous transitions in the 5p-5s band. 14.0 eV marks the ionization limit of Kr.

Table 2.1: Relevant NIST Atomic Spectra Database Lines Data [85] with labels matching Fig. 2.1. Racah nl[K]$_J$ notation. Transition I is not listed because it represents the recombination process. Transitions J/K/L, which represent numerous transitions in the 5p-5s band, have ranges and order of magnitude estimates as entries. Subscripts i and j denote the upper and lower energy levels respectively.

Transition	λ_{air} (nm)	Nature	Lower Level	Upper Level	A_{ij} (1/s)	E_j (cm^{-1})	E_i (cm^{-1})
A	216.670	Two-Photon	$4s^24p^6$, $^1S_0$	$5p[5/2]_2$	(-)	0	92307.3786
A†	214.769	Two-Photon	$4s^24p^6$, $^1S_0$	$5p[3/2]_2$	(-)	0	93123.3409
A*	212.556	Two-Photon	$4s^24p^6$, $^1S_0$	$5p[1/2]_0$	(-)	0	94092.8626
B	216.667	Single-Photon	$5p[5/2]_2$	Kr+	(-)	92307.3786	112917.62
B†	214.769	Single-Photon	$5p[3/2]_2$	Kr+	(-)	93123.3409	112917.62
B*	212.556	Single-Photon	$5p[1/2]_0$	Kr+	(-)	94092.8626	112917.62
C	877.675	Single-Photon	$5s[3/2]_1$	$5p[5/2]_2$	2.2×10^7	80916.7680	92307.3786
D	810.436	Single-Photon	$5s[3/2]_2$	$5p[5/2]_2$	8.9×10^6	79971.7417	92307.3786
E/F	769.454	Single-Photon	$5s[3/2]_2$	$5p[3/2]_1$	4.3×10^6	79971.7417	92964.3943
G	829.811	Single-Photon	$5s[3/2]_1$	$5p[3/2]_1$	2.9×10^7	80916.7680	92964.3943
H	123.584	Single-Photon	$4s^24p^6$, $^1S_0$	$5s[3/2]_1$	3.0×10^8	0	80916.7680
J/K/L	750-830	Single-Photon	$\overline{5s}$	$\overline{5p}$	$10^6 - 10^7$	80000.0000	90000.0000
M	758.950	Single-Photon	$5s[3/2]_1$	$5p[1/2]_0$	4.31×10^7	80916.7680	94092.8626
N	760.364	Single-Photon	$5s[3/2]_2$	$5p[3/2]_2$	2.732×10^7	79971.7417	93123.3409
O	819.230	Single-Photon	$5s[3/2]_1$	$5p[3/2]_2$	1.1×10^7	80916.7680	93123.3409

Three major excitation lines for Krypton Tagging Velocimetry are 212.556 nm, 214.769 nm, and 216.667 nm, assuming vacuum wavelengths. They (1) are accessible

with commercially available optics and laser systems, (2) have sufficiently high two-photon excitation cross-section, and (3) produce the Kr metastable state. Excitation levels for two-photon excited states of Kr in the 200-220 nm range are denoted in Table 2.3. Details and two-photon excitation cross-section calculations for each Kr scheme are provided in [33, 86]. Energy level diagrams for each scheme are shown in Fig. 2.1, and transitions are Table 2.1. Transitions A, $A^{\dagger}$, A^{*} denote two-photon excitation transitions. Transitions B, $B^{\dagger}$, B^{*} denote one-photon ionization transitions. All other transitions, except for electron-ion recombination, are one-photon transitions from which light is observed.

For the 212.556 nm line, spectroscopy was performed to show the types of Kr states resulting from electron-ion recombination. The resulting spectrum is shown in Fig. 2.2 and listed in Table 2.2. The experiments were conducted in a 5 torr quiescent flow of 99% N_2/1% Kr gas mixture. The write-laser system was a frequency doubled Quanta Ray Pro-350 Nd:YAG laser and a frequency tripled Sirah PrecisionScan Dye Laser (DCM dye, DMSO solvent). The Nd:YAG laser pumped the dye laser at a wavelength of 532 nm. The dye laser was tuned to output a 637.7 nm beam, and frequency tripling (Sirah THU 205) of the dye-laser output resulted in a 212.6 nm beam, with 3 mJ energy, 1350 MHz linewidth, and 7 ns pulse width at a repetition rate of 10 Hz. The write beam was focused into the test section of the Stevens Shock Tube with a 200 mm focal-length, fused-silica lens. The Kr fluorescence was imaged onto the slit of an Oriel MS257, 25 cm spectrograph prior to being imaged by a Princeton Instruments PIMAX-4 (PM4-1024i-HR-FG-18-P46-CM) camera. The lens used was a Nikon NIKKOR 24-85mm f/2.8-4D with a 0.5 inch lens tube positioned at the spectrograph exit. This experimental setup was calibrated with a Kr pen lamp (Newport 6031) [32]. The spectrum can be used to prove that (2+1) REMPI at 212.556 nm produces the krypton metastable state for an excitation scheme that would otherwise

be unable to generate metastable state with just two-photon excitation. It shows that much of the Kr fluorescence lies between 750-850 nm, a fact that is crucial for the KTV work performed in a high-background-luminosity environment like that at the Caltech Reflected-Shock Tunnel [82].

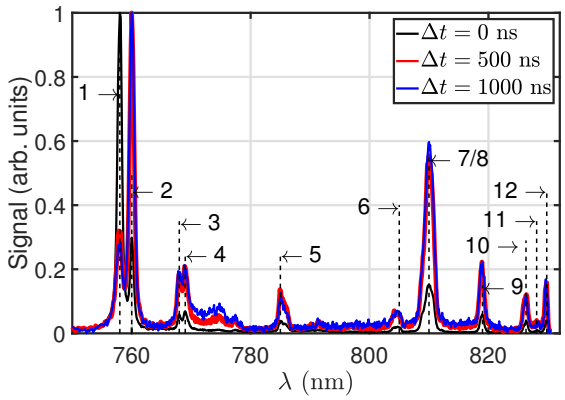

Figure 2.2: Emission spectra for (2+1) REMPI process using $\lambda = 212.6$ nm excitation in a 99% N_2/1% Kr mixture. Line identification is presented in Table 2.2. Intensities normalized by maximum intensity at each time step.

Table 2.2: NIST Atomic data for krypton spectra [85] using $\lambda = 212.6$ nm two-photon excitation in N_2, Racah nl[K]$_J$ notation. Line numbers correspond to Fig. 2.2.

Line	Transition	λ_{air} (nm)	Upper Level	Lower Level
1	M	758.74	$5p[1/2]_0$	$5s[3/2]^o_1$
2	N	760.15	$5p[3/2]_2$	$5s[3/2]^o_2$
3	L	768.52	$5p'[1/2]_0$	$5s'[1/2]^o_1$
4	F	769.45	$5p[3/2]_1$	$5s[3/2]^o_2$
5	L	785.48	$5p'[1/2]_1$	$5s'[1/2]^o_0$
6	L	805.95	$5p'[3/2]_1$	$5s'[1/2]^o_0$
7	D	810.44	$5p[5/2]_2$	$5s[3/2]^o_2$
8	J	811.29	$5p[5/2]_3$	$5s[3/2]^o_2$
9	O	819.01	$5p[3/2]_2$	$5s[3/2]^o_1$
10	L	826.32	$5p'[3/2]_2$	$5s'[1/2]^o_1$
11	L	828.11	$5p'[1/2]_1$	$5s'[1/2]^o_1$
12	G	829.81	$5p[3/2]_1$	$5s[3/2]^o_1$

The current state of KTV consists of (2+1) resonant enhanced multiphoton ionization (REMPI). REMPI is a compound process consisting of two-photon excitation

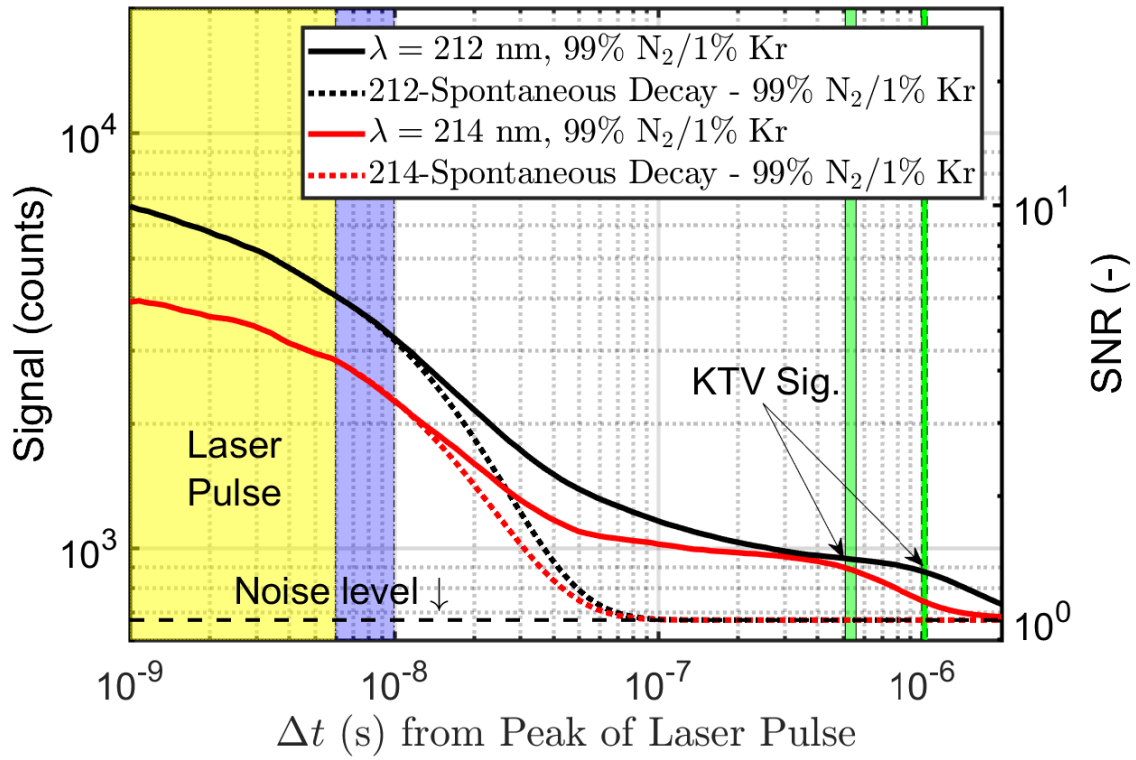

Figure 2.3: Fluorescence Decay Curves for 212 and 214 nm Excitation Lines. Dotted Lines Represent Theoretical 2-Photon Decay. Yellow Box Represents Laser Pulse Width. Blue Box Represent Camera Write Gate Width. Green Boxes Represent Possible Camera Read Gate Widths at either 500 ns and 1000 ns.

followed by a one-photon ionization. It is magnitudes more efficient than direct three-photon ionization and is governed by two ordinary differential equations [87], incorporating the two-photon excitation rate and the one-photon ionization rate. REMPI ionizes Kr gas, producing a cold plasma ($T_{ion} \ll T_e$), from which a long-lasting afterglow is observed. The fluorescence signal is primarily the result of electron-ion recombination and its resulting radiative cascade [88]. This afterglow is critical to single-laser KTV, as shown in Fig. 2.3,[1] forming the entirety of the read image signal.

In Fig. 2.3, typical fluorescence decay curves are shown for the 212.556 nm and

[1]Experiments were performed with the same setup used for the spectroscopy study.

214.769 nm excitation lines. During laser excitation of Kr (yellow region), the tagged Kr tracer is formed as a result of REMPI, consisting of both the two-photon excited state and the ionized state. The write image (blue region) in obtained in an interval (3-5 ns) following the write step. This image serves as a reference line to determine tagged tracer displacements. At a time Δt from the opening of the write camera gate, the read image is obtained using a camera gate of 50 ns (green region). In Fig. 2.3, the two-photon excited state plays little role in the KTV read image. Rather, it is the electron-ion recombination process and the resulting radiative cascade which is imaged by the camera. These time-dependent phenomenon dominate during the read step of single-laser velocimetry techniques.

Table 2.3: Excitation Spectrum data and theoretical cross-sections in 200-220 nm range, including excitation wavelengths, two-photon excited states, observed emission wavelengths of the two-photon state, calculated cross-sections, and experimental Kr excitation signal normalized against 212.556 nm excitation signal. Racah $nl\,[K]_J$ notation is used (LS_1 coupling).

Laser Wavelength λ_L (nm)		202.316	204.196	212.556	214.769	216.667
Two-Photon Excited State		$5p\prime[1/2]_0$	$5p\prime[3/2]_2$	$5p[1/2]_0$	$5p[3/2]_2$	$5p[5/2]_2$
Primary Emission (nm)		768.74	826.55	758.95	760.36	810.66
Calc. Cross-Section (10^{-35} cm^4)		4.17	3.25	23.6	4.18	6.33
N. Signal	Richardson et al. fs-excitation	0.20	0.13	1.00	0.14	0.21
	Grib et al. fs-excitation	(-)	(-)	1.00	0.153	(-)
	Grib et al. ns-excitation	(-)	(-)	1.00	0.132	(-)
	Present Work ns-excitation	(-)	(-)	1.00	0.319	0.290

2.1 The Optimal Excitation Line for Krypton using First Order Perturbation Theory

A theoretical excitation line optimization study was performed in [33, 86] using multi-path, first-order accurate perturbation theory, and its results are shown in Fig. 2.4 and tabulated in Table 2.3. The matrix mechanics formulation of Lambropoulos [91], who provides a thorough review of multiphoton processes and calculations, is used because

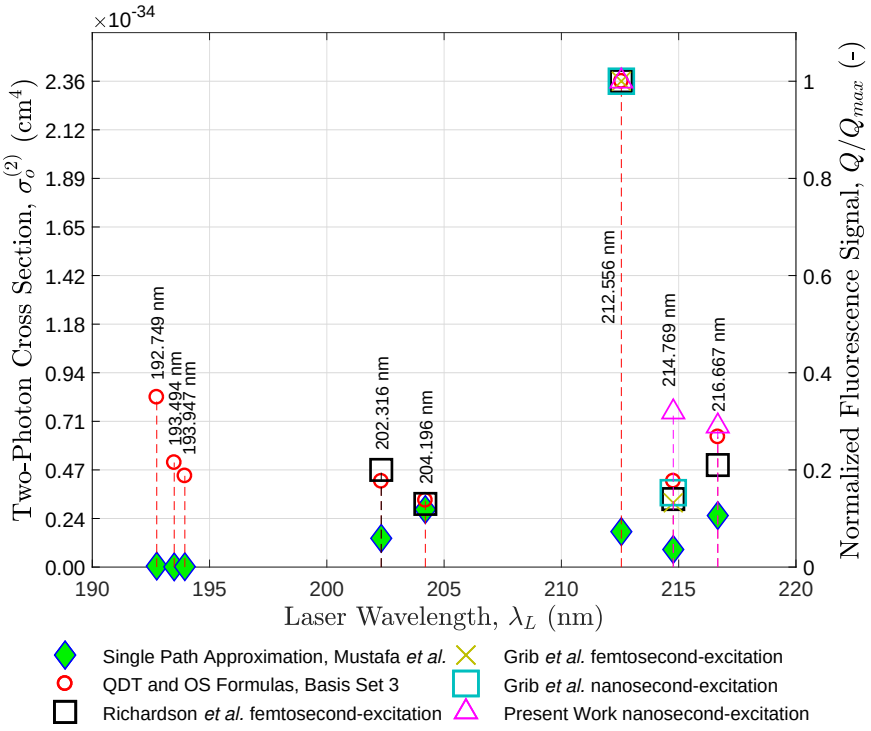

Figure 2.4: Two-photon Excitation Cross-sections using Basis Set 3 using basis set 3 from [33] as the Basis of Intermediate States, which included $5s$, $6s$, $7s$, $4d$, $5d$, and $6d$ states. Via quantum-defect theory (QDT) and oscillator strength formulas, cross-sections were calculated and compared to the excitation data of Richardson *et al.*, Grib *et al.*, and this work. Richardson data were obtained by fs-laser excitation in a 1 bar, 95% Ar/5% gas mixture. Grib data were obtained by both fs-laser and ns-laser excitations in a 1 atm, 77% N_2/33% Kr gas mixture. My lab data was obtained via ns-laser excitation in 1 torr, 99% N_2/1% Kr gas mixture to minimize collisional effects. Values are listed in Table 2.3.

it obtains all excitation pathways for a finite basis of states. With the intention of contributing to the hypersonic diagnostics community, this work obtained a simplified formula for the dipole matrix element for linearly polarized excitation and justified the use of analytical, quantum-defect, hydrogenic radial wave functions to describe excited Kr states, as shown in Fig. 2.5.[2] This work makes an existing mathemat-

[2]An in-house Hartree-Fock MATLAB code was written to compare first-order accurate radial wave functions to quantum-defect radial wave functions. This code accounts for first-order electron repulsion potentials and solves the nonrelativistic Schödinger Equation, using finite differences, fixed point iteration, and eigenvalue inverse-power iteration. See Appendix A.

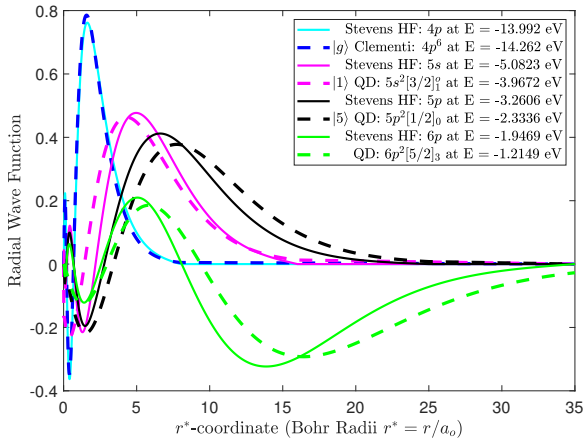

Figure 2.5: Comparison between Hartree-Fock (HF) Radial Orbitals and Quantum-Defect (QD) Radial Orbitals. The Clementi $4p$ radial wave is described in [89]. This plot demonstrates the hydrogen-like behavior of Kr radial wave functions. This plot justifies the use of quantum-defect orbitals and validates Rydberg's original observation of the hydrogenic behavior of excited atoms [90].

ical framework more understandable in order to support multiphoton cross-section calculations and excitation line optimization studies for other tagging techniques. A Hartree-Fock radial wave function of the krypton ground state $(4p^6\ {}^1S_0)$ [3] was assumed [89], and oscillator-strength (OS) formulas were used upon the availability of NIST transition probabilities and data [85]. It is noted that a Kr gas mixture with naturally-occurring isotope mole fractions was considered because the NIST line spectra database presents spectroscopic data for a naturally-occurring mixture of Kr [85]. Additionally, quantum-defect theory (QDT) was used to calculate electric dipole matrix elements $\langle i|\,\hat{\epsilon}\cdot\vec{r}\,|j\rangle$ when NIST transition probabilities were unlisted. This use of QDT is key to the success of the approach, as it enabled the inclusion of additional excitation pathways not included in previous works; and it determined the sign of all pathway contributions to the two-photon matrix element. When QDT is used to evaluate the purely radial matrix elements $\langle r\rangle$, scaled hydrogen radial wave functions are constructed to represent excited Kr states. With the aid of QDT, a

[3] Russell-Saunders Notation ${}^{2S+1}L_J$ with $S = 0$, $L = 0$, and $J = 0$.

truncated spectral expansion of a Green's function was constructed from a basis of intermediate Kr states ($5s$, $6s$, $7s$, $4d$, $5d$, and $6d$ states) that approximately satisfy the nonrelativistic Schrödinger equation. Within the framework of matrix mechanics, this expansion ultimately allowed the evaluation of the two-photon-transition matrix element.

2.1.1 Two-Photon Cross-Section Calculation for Kr

The two-photon cross-section $\sigma_o^{(2)}$ is independent of laser intensity, time, and Kr concentration. It is a solution to the time-independent, non-relativistic Schrödinger equation [4]. At the rising edge of the laser pulse, $\sigma_o^{(2)} \propto \sigma^{(2)} \propto Q \propto \text{SNR}$ [93]. The two-photon cross-section $\sigma_o^{(2)}$ is related to the two-photon excitation rate-coefficient $\sigma^{(2)}$ via the lineshape function $g(2\omega_L)$ as

$$\sigma^{(2)} = \sigma_o^{(2)} g(2\omega_L). \tag{2.1.1}$$

The two-photon excitation cross-section is calculated as

$$\sigma_o^{(2)} = (2\pi)^3(\alpha)^2\omega_L^2 \left|M_{fg}^{(2)}\right|^2 a_o^4, \tag{2.1.2}$$

where α is the fine structure constant, a_o is the Bohr radius, and $M_{fg}^{(2)}$ is the two-photon-transition matrix element [94, 95]. The line shape function $g(2\omega_L)$[5] is assumed

[4] Relativistic effects were neglected in the Schrödinger equation because the energy of the laser was much less than the rest energy of an electron $3\hbar\omega_L \ll m_e c^2$ [92].

[5] The multiphoton lineshape function is $g(n_{ph}\omega_L, \omega_T) = \frac{2\sqrt{\ln(2)/\pi}}{\sqrt{n_{ph}(\Delta\omega_L)^2 + (\Delta\omega_T)^2}} \exp\left(\frac{4\ln(2)(n_{ph}\omega_L - \omega_T)^2}{n_{ph}(\Delta\omega_L)^2 + (\Delta\omega_T)^2}\right)$, formed by the convolution of the Gaussian lineshapes for Doppler Broadening and Laser Linewidth [96], written in terms of full width at half maximum (FWHM).

to be of Gaussian form with a peak:

$$g(2\omega_L = \omega_T) = \frac{2\sqrt{\ln(2)/\pi}}{\sqrt{2(\Delta\omega_L)^2 + (\Delta\omega_T)^2}}. \tag{2.1.3}$$

The linewidth of the laser is $\Delta\omega_L$ (1350 MHz in this work), and the Doppler linewidth, $\Delta\omega_T$, is calculated by

$$\Delta\omega_T = (2\omega_L)\sqrt{\frac{8\ln(2)k_bT}{m_{kr}c^2}}, \tag{2.1.4}$$

where k_b is the Boltzmann constant, c is the speed of light, m_{kr} is the mass of one krypton atom, and T is the temperature of the Kr gas mixture.

The two-photon-transition matrix element is expressed as

$$M_{fg}^{(2)} = \sum_{k=g}^{\infty} \frac{\langle f | \hat{\epsilon} \cdot \vec{r} | k \rangle \langle k | \hat{\epsilon} \cdot \vec{r} | g \rangle}{\omega_k - \omega_g - \omega_L}, \tag{2.1.5}$$

where $|g\rangle$ is the ground state, $|f\rangle$ is the two-photon excited state, $|k\rangle$ is the intermediate state, and $\hat{\epsilon} \cdot \vec{r}$ is the electric dipole operator. Angular frequencies ω_g, ω_f, and ω_k respectively represent the energies of the ground, final, and intermediate states.[6] For practical calculation on a computer, the summation over the intermediate state index k is truncated at the N^{th} state. Therefore, the transition matrix element,

$$M_{fg}^{(2)} = \sum_{k=g}^{N} \frac{\langle f | \hat{\epsilon} \cdot \vec{r} | k \rangle \langle k | \hat{\epsilon} \cdot \vec{r} | g \rangle}{\omega_k - \omega_g - \omega_L}, \tag{2.1.6}$$

is summed over a finite basis of states, such as those listed in Table 2.6. Bra-ket notation from Liboff [97] is used to represent each atomic state and its associated set of good quantum numbers. The truncation criterion for two-photon excitation is determined by a constraint on the maximum principal quantum number n of a

[6]For a state with energy E, the angular frequency of the state is $\omega = E/\hbar$.

bound state: n_{max}. As n becomes large, the expected radius of a one-electron atom of effective nuclear charge Z_e is $\langle r \rangle = n^2/Z_e$ in Bohr radii [97]. Per Park [98], the $\langle r \rangle$ is proportional to the Debeye length d_D:

$$n_{\max} = \sqrt{\frac{Z_e d_D}{10 a_o}} \approx \left(\frac{Z_e^2 \epsilon_o k_b}{e^2 \left(\frac{N_e}{T_e V} + \frac{N_e}{TV} \right) (10 a_o)^2} \right)^{\frac{1}{4}}, \tag{2.1.7}$$

where N_e/V is the electron number density and N_i/V is the ion number density, T_e is the electron temperature, and T_i is the Kr ion temperature. The factor of $10a_o$ describes approximately the krypton van der Waals diameter and represents a 90% reduction in the Debeye potential, Φ_D, which is non-dimensionally described by $\Phi_D = 1/r \exp(-r a_o/d_D)$ [97]. For the (2+1) resonance-enhanced multiphoton excitation of Kr at laser wavelength $\lambda_L = 212.556$ nm, room temperature $T = 298$ K, and pressure $P = 1$ torr, the electron temperature is $T_e = 27626$ K and number densities are calculated as $N_e/V = N_i/V = 1.62 \times 10^{21}$ electrons/m^3. The electron temperature was obtained from $2(3\hbar\omega_L - |E_{ion}|)/3k_b$ [99], and number densities were obtained via the analytical population model of Saito et al. [87]. Assuming $Z_e = 1$ for the Kr ion, the result is $n_{\max} = 7.42$. Therefore, N accommodates all states with a principal quantum number equal to or less than 7: $n \leq 7$. This is convenient because NIST transition probability data is limited for states with $n \leq 8$ [85].

An approximate Green's function, expressed as a truncated spectral expansion, is nested in the center of the expression for $M_{fg}^{(2)}$:

$$G(\vec{r}, \vec{r}\,') = \sum_{k=g}^{N} \frac{|k(\vec{r})\rangle \langle k(\vec{r}\,')|}{\omega_k - \omega_g - \omega_L}, \tag{2.1.8}$$

which is a function of the set of all position vectors $\vec{r}$ and $\vec{r}\,'$ for each electron in

the Kr atom.[7] Following matrix mechanics notation (and for brevity), the position vectors $\vec{r}$ and $\vec{r}\,'$ are henceforth omitted.

Since Green's functions are symmetric about variable exchange ($\vec{r} \leftrightarrow \vec{r}\,'$), $G(\vec{r}, \vec{r}\,') = G(\vec{r}\,', \vec{r})$, so $M^{(2)}_{fg} = M^{(2)}_{gf}$. This mathematical property is a fundamental deviation from the oscillator-strength approach in Khambatta et al. [94], which is one-sided and asymmetric. Therefore, the use of oscillator formulas, while valid, causes the loss of symmetry in the transition-matrix element. This symmetry loss is problematic in describing higher-order multiphoton excitation (three-photon and higher).

$M^{(2)}_{fg}$ is a double tensor contraction of an infinite matrix space $M = DGD$, where D and G are the matrix representations of the dipole matrix operator and Green's function operator, respectively. More importantly, due to the invariance of multiphoton-excitation with respect to reference frame and basis $|k\rangle$, $M = DGD$ is a symmetric, rank-2 tensor. The evaluation of $M^{(2)}_{fg}$ requires the evaluation of two reduced matrix elements of the form

$$\langle i \,|\hat{\epsilon} \cdot \vec{r}| \, j\rangle = D_{ij}, \tag{2.1.9}$$

[7] A one-electron model is not yet assumed.

where D_{ij} is an element of the matrix representation of the dipole operator D:

$$D = \begin{bmatrix} \langle g|\hat{\epsilon}\cdot\vec{r}|g\rangle & \langle g|\hat{\epsilon}\cdot\vec{r}|1\rangle & \langle g|\hat{\epsilon}\cdot\vec{r}|2\rangle & \cdots & \cdots & \langle g|\hat{\epsilon}\cdot\vec{r}|N\rangle \\ \langle 1|\hat{\epsilon}\cdot\vec{r}|g\rangle & \langle 1|\hat{\epsilon}\cdot\vec{r}|1\rangle & \langle 1|\hat{\epsilon}\cdot\vec{r}|2\rangle & \cdots & \cdots & \langle 1|\hat{\epsilon}\cdot\vec{r}|N\rangle \\ \langle 2|\hat{\epsilon}\cdot\vec{r}|g\rangle & \langle 2|\hat{\epsilon}\cdot\vec{r}|1\rangle & \langle 2|\hat{\epsilon}\cdot\vec{r}|2\rangle & \cdots & \cdots & \langle 2|\hat{\epsilon}\cdot\vec{r}|N\rangle \\ \vdots & \vdots & \vdots & \ddots & & \vdots \\ \vdots & \vdots & \vdots & & \ddots & \vdots \\ \langle N|\hat{\epsilon}\cdot\vec{r}|g\rangle & \langle N|\hat{\epsilon}\cdot\vec{r}|1\rangle & \langle N|\hat{\epsilon}\cdot\vec{r}|2\rangle & \cdots & \cdots & \langle N|\hat{\epsilon}\cdot\vec{r}|N\rangle \end{bmatrix}. \tag{2.1.10}$$

The two indices i, j of the matrix D represent the final state $|i\rangle$ and initial state $|j\rangle$, respectively. Here, the ground state is denote as $|g\rangle$, and all other states (1 - N) are denoted as $|1\rangle$ to $|N\rangle$. The dipole operator, $\hat{\epsilon}\cdot\vec{r}$, describes the rotation of two electric charges of opposite sign by an external electric field. The denominator of Eq. 2.1.6,

$$G_{ii} = \frac{1}{\omega_i - \omega_g - \omega_L}, \tag{2.1.11}$$

can also be rewritten in matrix form as a diagonal matrix G:

$$G = \begin{bmatrix} \frac{1}{\omega_g-\omega_g-\omega_L} & 0 & \cdots & 0 & 0 \\ 0 & \frac{1}{\omega_1-\omega_g-\omega_L} & \ddots & \vdots & \vdots \\ \vdots & \ddots & \ddots & \ddots & \vdots \\ \vdots & & \ddots & \frac{1}{\omega_{(N-1)}-\omega_g-\omega_L} & 0 \\ 0 & 0 & \cdots & 0 & \frac{1}{\omega_N-\omega_g-\omega_L} \end{bmatrix}. \tag{2.1.12}$$

G is the matrix representation of the Green's function, Eq. 2.1.8. Rewriting

Eq. 2.1.6, the transition matrix element can be represented in matrix form:

$$M_{fg}^{(2)} = \sum_{k=g}^{N} D_{fk} G_{kk} D_{kg} = \hat{e}_f^T D G D \hat{e}_g, \tag{2.1.13}$$

where $\hat{e}_i$ is a unit vector that identifies the state of the system. For example, the vector representations of states $|g\rangle$, $|1\rangle$, $|2\rangle$, and $|N\rangle$ are

$$\hat{e}_g = \begin{Bmatrix} 1 \\ 0 \\ 0 \\ \vdots \\ 0 \end{Bmatrix}, \ \hat{e}_1 = \begin{Bmatrix} 0 \\ 1 \\ 0 \\ \vdots \\ 0 \end{Bmatrix}, \ \hat{e}_2 = \begin{Bmatrix} 0 \\ 0 \\ 1 \\ \vdots \\ 0 \end{Bmatrix}, \text{ and } \hat{e}_N = \begin{Bmatrix} 0 \\ 0 \\ 0 \\ \vdots \\ 1 \end{Bmatrix}. \tag{2.1.14}$$

Eq. 2.1.13 substantiates to a rank 2 tensor contraction of the Green's function matrix G. The f^{th} row of matrix D is post-multiplied by the matrix G, which is then post-multiplied by the g^{th} column of matrix D, resulting in the scalar $M_{fg}^{(2)}$.

2.1.2 The Calculation of Dipole Matrix Elements D_{ij} Using QDT

In this section, the dipole matrix elements D_{ij} are calculated via the central-field approximation [97, 100], which allows one to separate the effects of angular and radial components in the Schrödinger equation, expressed in spherical coordinates. This allows a state $|k\rangle$ to be expressed as a product of one-electron, radial wave functions $R_{nl}(r) \cdot \prod_p R_p(r_p)$ multiplied by a tensor spherical harmonic $\mathbf{Y}_{JM}^{LS}(\theta, \phi)$. Here, subscript p denotes an unexcited krypton electron, and nl denotes the quantum numbers of the valence electron to be excited by the laser. This state is represented as $|\mathbf{n}LSJM\rangle$, assuming LS spin-orbit coupling. The radius of the excited valence electron from the Kr nucleus is r. The orientation of its angular momentum is described

by azimuth angle θ and polar angle ϕ. The set of all principal quantum numbers for the Kr atom is $\mathbf{n}$, and the principal quantum number of the excited electron is n. L is the total orbital angular momentum quantum number of the atom, and l is the single-electron angular momentum number of the excited electron. S is the total electron spin quantum number of the atom. For a true dipole moment transition, S remains constant because the dipole moment operator $\hat{\epsilon} \cdot \vec{r}$ does not act on electron spin coordinates. The dipole moment operator is solely written in terms of scalar spherical harmonics [100]:

$$\hat{\epsilon} \cdot \vec{r} = \sqrt{\frac{4\pi}{3}} r \sum_{q=(0,\pm 1)} \epsilon_q Y_1^q, \tag{2.1.15}$$

where the polarization component is ϵ_q; $q = 0$ for linear polarization; $q = 1$ for right-handed circular polarization; and $q = -1$ for left-handed polarization of the laser's electric field [101]. The orientation of the laser electric field defines the orientation of the z-axis in the spherical coordinate system imposed on the nucleus of a Kr atom.

To evaluate the reduced matrix elements D_{ij}, a simplified expression must first be obtained. By applying the Wigner-Eckart Theorem [101], D_{ij} may be rewritten as

$$\begin{aligned} D_{ij} &= \langle i \,|\hat{\epsilon} \cdot \vec{r}|\, j \rangle \\ &= \langle \mathbf{n}_i L_i S_i J_i M_i \,|\hat{\epsilon} \cdot \vec{r}|\, \mathbf{n}_j L_j S_j J_j M_j \rangle \\ &= \langle \mathbf{n}_i L_i S_i J_i \,|\vec{r}|\, \mathbf{n}_j L_j S_j J_j \rangle \\ &\quad \times \sum_{q=(0,\pm 1)} \epsilon_q \begin{pmatrix} J_i & 1 & J_j \\ -M_i & q & M_j \end{pmatrix} (-1)^{1-J_j-M_i}. \end{aligned} \tag{2.1.16}$$

By using the definition of a location vector $\vec{r} = r\hat{e}_r$, radial coordinates are separated

from angular coordinates:

$$D_{ij} = \langle i \,|r|\, j\rangle \, \langle L_i S_i J_i \,|\hat{e}_r|\, L_j S_j J_j\rangle \\ \times \sum_{q=(0,\pm 1)} \epsilon_q \begin{pmatrix} J_i & 1 & J_j \\ -M_i & q & M_j \end{pmatrix} (-1)^{1-J_j-M_i}. \tag{2.1.17}$$

Using the following expression from Messiah [101] (Eq. C.89) for reduced matrix elements and irreducible tensor operators of tensor rank k,

$$\left\langle \tau_1 \tau_2 J_1 J_2 J \left| T^{(k)} \right| \tau_1' \tau_2' J_1' J_2' J' \right\rangle = \\ \delta_{\tau_2 \tau_2'} \delta_{J_2 J_2'} \left\langle \tau_1 J_1 \left| T^{(k)} \right| \tau_1' J_1' \right\rangle (-1)^{J'+J_1+J_2+k} \\ \times \sqrt{(2J+1)(2J'+1)} \begin{Bmatrix} J_1 & k & J_1' \\ J' & J_2 & J \end{Bmatrix}, \tag{2.1.18}$$

the angular term $\langle L_i S_i J_i \,|\hat{e}_r|\, L_j S_j J_j\rangle$ can be further simplified, noting $\tau_1 = \tau_1' = \tau_2 = \tau_2' = 1$. The reduced matrix element D_{ij} becomes

$$D_{ij} = \delta_{S_i S_j} \langle r\rangle \, \langle L_i \,|\hat{e}_r|\, L_j\rangle \, (-1)^{L_i+J_j+S_i+1} \\ \times \sqrt{(2J_i+1)(2J_j+1)} \begin{Bmatrix} L_i & 1 & L_j \\ J_j & S_j & J_i \end{Bmatrix} \\ \times \sum_{q=(0,\pm 1)} \epsilon_q \begin{pmatrix} J_i & 1 & J_j \\ -M_i & q & M_j \end{pmatrix} (-1)^{1-J_j-M_i}, \tag{2.1.19}$$

where $\langle r\rangle = \langle i \,|r|\, j\rangle$ is the purely radial matrix element. The term $\delta_{S_i S_j}$ implies that the dipole moment operator (Eq. 2.1.15) does not act on electron spin coordinates [100, 102]. Next, using the Wigner-Eckart Theorem [101] for the expected value of a

spherical tensor Y_k of rank k,

$$\begin{aligned}\langle l_1 \left| Y_k \right| l_2 \rangle &= \\ &= (-1)^{l_1} \sqrt{\frac{(2l_1+1)(2k+1)(2l_2+1)}{4\pi}} \begin{pmatrix} l_1 & k & l_2 \\ 0 & 0 & 0 \end{pmatrix},\end{aligned} \tag{2.1.20}$$

the expected value of the rank-1 unit vector $\hat{e}_r$, $\langle L_i \left| \hat{e}_r \right| L_j \rangle$, can be evaluated. D_{ij} becomes

$$\begin{aligned} D_{ij} = \delta_{S_i S_j} \langle r \rangle & \sqrt{(2L_i+1)(2L_j+1)} \\ & \times \begin{pmatrix} L_i & 1 & L_g \\ 0 & 0 & 0 \end{pmatrix} \sqrt{(2J_i+1)(2J_j+1)} \\ & \times (-1)^{2L_i+J_j+S_i+1} \begin{Bmatrix} L_i & 1 & L_j \\ J_j & S_j & J_i \end{Bmatrix} \\ & \times \sum_{q=(0,\pm 1)} \epsilon_q \begin{pmatrix} J_i & 1 & J_j \\ -M_i & q & M_j \end{pmatrix} (-1)^{1-J_j-M_i}, \end{aligned} \tag{2.1.21}$$

which rearranges into

$$\begin{aligned} D_{ij} = \delta_{S_i S_j} \langle r \rangle & \sqrt{(2J_i+1)(2J_j+1)(2L_i+1)(2L_j+1)} \\ & \times \begin{pmatrix} L_i & 1 & L_g \\ 0 & 0 & 0 \end{pmatrix} \begin{Bmatrix} L_i & 1 & L_j \\ J_j & S_j & J_i \end{Bmatrix} (-1)^{2L_i+J_j+S_i+1} \\ & \times \sum_{q=(0,\pm 1)} \epsilon_q \begin{pmatrix} J_i & 1 & J_j \\ -M_i & q & M_j \end{pmatrix} (-1)^{1-J_j-M_i}. \end{aligned} \tag{2.1.22}$$

For allowable dipole transitions, the effect of the factor of $-1^{-J_j-M_i+1}$, which arises from the definition of the Wigner-Eckart Theorem, has no effect on the transition

Table 2.4: Parity Table for term $-1^{-J_j-M_i+1}$. $J_j = 0, 1$ correspond to 2-photon transitions, and $J_j = 0, 1, 2$ correspond to 3-photon transitions. The term $-1^{-J_j-M_i+1}$ does not contribute to the transition matrix element summation because it is consistently the same value for each stage of a multiphoton transition for all possible pathways.

J_j	0		1		2	
M_i	0	1	0	-2	0	3
$-1^{-J_j-M_i+1}$	-1	1	1	1	-1	1

matrix element summation due to the consistent parity of J, as shown in Table 2.4.

The 2×3 matrix terms in parentheses are $3j$-Wigner Symbols, and the 2×3 matrix term in brackets is the $6j$-Wigner Symbol. $3j$-Wigner Symbols enforce dipole moment selection rules, and the $6j$-Wigner Symbol quantifies the degeneracy of a transition occurring (it amounts to a normalization factor). This research only considers linear polarization of the laser electric field, $q = 0$, forcing $M_i = M_j = 0$ for all transitions $j \rightarrow i$. $S_i = S_j = 0$ for all transitions because the Kr ground state has a total electron spin of zero, and the dipole moment operator $\hat{\epsilon} \cdot \vec{r}$ does not act on electron spin coordinates. L_i is the norm of the addition of two angular momenta, $L_i = |\vec{l_i} + \vec{l_g}|$, which describes the angular momentum coupling between the excited electron and a $4p$ valence electron of opposite electron spin. Since the dipole moment operator does not operate on electron coordinates, $L_i = J_i$ for the dipole transitions analyzed in this work. A cartoon summarizing how angular momentum changes during $(2+1)$-photoionization is shown in Fig. 2.6, and an angular momentum table is provided in Table 2.5 to show how to calculate the coupled quantum L from the angular momenta of two electrons, each with an azimuth orbital quantum number $m = 0$.

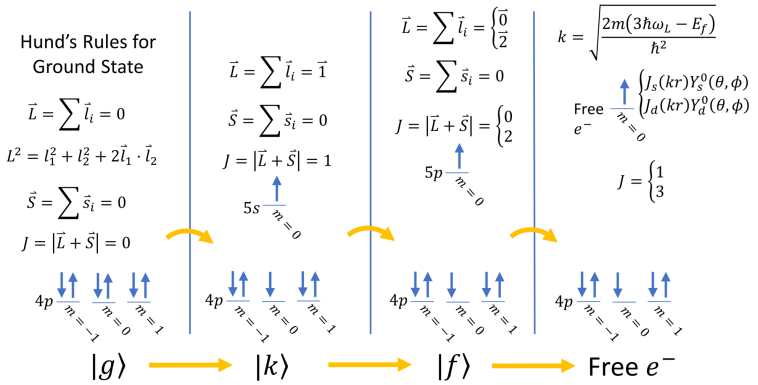

Figure 2.6: Angular momenta of a Kr atom during linearly polarized (2+1) multiphoton photoionization. This cartoon demonstrates LS spin-orbit coupling for each Kr state at each stage of excitation: ground state $|g\rangle$, intermediate state $|k\rangle$, two-photon state $|f\rangle$, and ionized state e^-. For dipole transitions, $\Delta S = 0$ and consequently, $J = L$.

Table 2.5: Addition of the angular momentum of two electrons l_1 and l_2: $\vec{L} = \vec{l_1} + \vec{l_2}$. $m = 0$ for both electrons.

State	$L^2 = l_1^2 + l_2^2 + 2\vec{l_1} \cdot \vec{l_2}$	L	J
$\|g\rangle$	$1^2 + 1^2 + 2(1)(-1) = 0$	0	0
$\|k\rangle$	$1^2 + 0^2 + 2(1)(0) = 1$	1	1
$\|f\rangle$	$1^2 + 1^2 + 2(1)(\pm 1) = \left\{ \begin{array}{c} 4 \\ 0 \end{array} \right\}$	$\left\{ \begin{array}{c} 2 \\ 0 \end{array} \right\}$	$\left\{ \begin{array}{c} 2 \\ 0 \end{array} \right\}$

Therefore, the simplified dipole matrix element is

$$D_{ij} = \delta_{l_i, l_j \pm 1} \langle r \rangle (2J_i + 1)(2J_j + 1) \times \begin{pmatrix} J_i & 1 & J_j \\ 0 & 0 & 0 \end{pmatrix}^2 \begin{Bmatrix} J_i & 1 & J_j \\ J_j & 0 & J_i \end{Bmatrix}, \tag{2.1.23}$$

noting that for a dipole transition $\Delta l = \pm 1$. The factor of $(-1)^{2L_i + J_j + S_i + 1}$ is omitted because it does not contribute any meaningful sign change in the summation. For dipole moments, parity is conserved, resulting in consistent state parity. $S_i + 1$ is

always 1; $2L_i$ is always even; and -1^{J_j} is consistent for all considered transitions. More interestingly, due to the consistent parity of J for transition states, Eq. 2.1.23 is symmetric about variable exchange $i \leftrightarrow j$, which conforms to the symmetry property of a Green's function Eq. 2.1.8. Using identity (C.37) from [101], Eq. 2.1.23 can be further simplified to

$$D_{ij} = \delta_{l_i,l_j\pm1} \langle r \rangle \sqrt{(2J_i+1)(2J_j+1)} \times \begin{pmatrix} J_i & 1 & J_j \\ 0 & 0 & 0 \end{pmatrix}^2 . \tag{2.1.24}$$

The mathematical structure is similar to that of the integral of the product of three spherical harmonics. Eq. 2.1.24 is a major highlight of this research.

Radial Wave Functions for the Evaluation of the Purely Radial Matrix Element $\langle r \rangle$

The main difficulty with calculating D_{ij} is the evaluation of the radial wave function integral $\langle r \rangle$:

$$\begin{aligned} \langle r \rangle &= \langle R_i(r) \, |r| \, R_j(r) \rangle \prod_p \langle R_{i,p}(r_p) | R_{j,p}(r_p) \rangle \\ &= \int_0^\infty r^3 R_i(r) R_j(r) dr \end{aligned} \tag{2.1.25}$$

because the form of the wave functions $R_i(r)$ must be assumed from prior knowledge. The one-electron model of Kr also assumes that only the radial wave function of the excited electron changes (not the unexcited Kr electron denoted by p), an assumption justified by a Hartree-Fock calculation [89]. Therefore, $\prod_p \langle R_{i,p}(r_p) | R_{j,p}(r_p) \rangle = 1$, due to the normalization of the radial wave functions.

Excited states of noble gas atoms approximate one-electron atoms, and to first

order, electric dipoles. Quantum-defect theory correctly assumes that the excited states of atoms exhibit scaled, hydrogen-like behavior, as verified by the Hartree-Fock calculation shown in Fig. 2.5. This observation was first made by Rydberg [90] and was later exploited by Bethe et al. [92], Bebb et al. [103], and McGuire [104, 105] to do cross-section calculations for noble gases. While Hartree-Fock iterates for an explicit electron repulsion potential [89, 100], quantum-defect theory directly incorporates the effect of electron repulsion through the use of excited state energy as an input to scale the wave function. With the verified assumption of hydrogenic behavior for excited Kr states, quantum-defect radial wave functions can be used with confidence to describe the excited states of Kr.

Properly normalized hydrogen radial wave functions [106] are expressed as

$$R_{nl}(r) = \sqrt{\left[\frac{(n-l-1)!}{2n((n+l)!)}\left(\frac{2Z_e}{n}\right)^3\right]}\left(\frac{2Z_e r}{n}\right)^l \times \exp\left(\frac{-Z_e r}{n}\right) L_{n-l-1}^{2l+1}\left(\frac{2Z_e r}{n}\right), \tag{2.1.26}$$

with effective nuclear charge $Z_e = 1$ and energy $E_n = -Ry/n^2$. Meanwhile, quantum-defect radial wave functions [90] are scaled hydrogen radial wave functions and are written similarly as

$$R_{nl}(E, I_m, r) = \frac{2}{(n^*)^2}\sqrt{\frac{\Gamma(n-l-I_m(l))}{\Gamma(n^*+l^*+1)}}\left(\frac{2r}{n^*}\right)^l \times \exp\left(\frac{-r}{n^*}\right) L_{n-l-I_m(l)-1}^{2l^*+1}\left(\frac{2r}{n^*}\right), \tag{2.1.27}$$

where the effective principal quantum number is

$$n^* = n - \delta_d, \tag{2.1.28}$$

the quantum defect is

$$\delta_d = n - \sqrt{\frac{-Ry}{E}}, \tag{2.1.29}$$

and the effective angular momentum quantum number is

$$l^* = l - \delta_d + I_m(l). \tag{2.1.30}$$

Γ is the gamma function; ( )! is the factorial function; and $L_n^y(x)$ is the associated Laguerre polynomial function of degree n and input y evaluated at x. Eq. 2.1.27 is a scaled version of Eq. 2.1.26.

Quantum-defect radial wave functions are generated by four input parameters n, l, E, and I_m, which are determined by NIST data [85] and are listed in Table 2.6 for a basis of Kr states. Quantum numbers n and l are reported in the Racah notation of a state. Absolute energy E is obtained by subtracting the first ionization energy of Kr (13.9996053 eV) from the reported NIST energy because NIST reports energy relative to the ground state. For the selection of the integer I_m, Einstein coefficients are used to ensure that the radial wave functions reflect experimental observations. Also, $(\delta_d - l - 1/2) \leq I_m < (n - l - 1)$ [90]. By minimizing the discrepancy between calculated Einstein coefficients [107],

$$A_{ij} = \frac{2e^2\omega_{ij}^3 a_o^2}{3c^3 h\epsilon_o} \sum_{m_j} \left| \langle n_i l_i m_i | \, \vec{r} \, | n_j l_j m_j \rangle \right|^2, \tag{2.1.31}$$

and tabulated NIST Einstein coefficients through integer variation of I_m, acceptable radial wave functions are constructed for excited Kr states.

The initial state $|i\rangle$ has a degenerate azimuth quantum number m_i. In a pure dipole moment transition, the only active quantum number is the angular momentum quantum number l. A weighted summation must take place over both m_i and m_j

Table 2.6: Input Parameters for Quantum-Defect Radial Wave Functions. This table also provides the basis of states used to calculate the two-photon transition matrix element. Data was obtained from NIST [85]. States $|5\rangle$, $|6\rangle$, $|9\rangle$, $|11\rangle$, $|12\rangle$, $|15\rangle$, $|16\rangle$, and $|17\rangle$ are of critical interest for the laser excitation lines considered in this work The two-photon excitation wavelengths, λ_L, are measured in vacuum.

Index	State (Term Symbol)*	n	l	E (eV)	I_m	λ_L (nm)
g	$4p^6\ ^1S_0$	4	1	-13.9996053	-	-
1	$(^2P^o_{3/2})5s\ ^2[3/2]^o_1$	5	0	-3.96720476	3	-
2	$(^2P^o_{3/2})5s\ ^2[3/2]^o_2$	5	0	-4.08437309	2	-
3	$(^2P^o_{1/2})5s\ ^2[1/2]^o_1$	5	0	-3.35597053	3	-
4	$(^2P^o_{1/2})5s\ ^2[1/2]^o_0$	5	0	-3.43719109	2	-
5	$(^2P^o_{3/2})5p\ ^2[1/2]_0$	5	1	-2.33357724	3	212.556
6	$(^2P^o_{3/2})5p\ ^2[3/2]_2$	5	1	-2.45378261	1	214.769
7	$(^2P^o_{3/2})5p\ ^2[1/2]_1$	5	1	-2.69615013	2	219.374
8	$(^2P^o_{3/2})5p\ ^2[5/2]_3$	5	1	-2.55655804	3	216.698
9	$(^2P^o_{3/2})5p\ ^2[5/2]_2$	5	1	-2.55494904	1	216.667
10	$(^2P^o_{3/2})5p\ ^2[3/2]_1$	5	1	-2.47348948	1	215.136
11	$(^2P^o_{1/2})5p\ ^2[3/2]_2$	5	1	-1.85595245	2	204.196
12	$(^2P^o_{1/2})5p\ ^2[1/2]_0$	5	1	-1.74313881	2	202.316
13	$(^2P^o_{1/2})5p\ ^2[1/2]_1$	5	1	-1.85917847	1	204.250
14	$(^2P^o_{1/2})5p\ ^2[3/2]_1$	5	1	-1.89925407	1	204.927
15	$(^2P^o_{3/2})6p\ ^2[1/2]_0$	6	1	-1.13480243	3	192.749
16	$(^2P^o_{3/2})6p\ ^2[3/2]_2$	6	1	-1.18427475	3	193.494
17	$(^2P^o_{3/2})6p\ ^2[5/2]_2$	6	1	-1.21421328	2	193.947
18	$(^2P^o_{1/2})6s\ ^2[1/2]_1$	6	0	-0.963121959	2	-
19	$(^2P^o_{3/2})6s\ ^2[3/2]_1$	6	0	-1.614321866	1	-
20	$(^2P^o_{1/2})7s\ ^2[1/2]_1$	7	0	-0.885709772	1	-
21	$(^2P^o_{3/2})4d\ ^2[3/2]_1$	4	2	-1.645049675	1	-
22	$(^2P^o_{3/2})5d\ ^2[1/2]_1$	5	2	-1.129823313	2	-
23	$(^2P^o_{3/2})6d\ ^2[3/2]_1$	6	2	-0.577230406	1	-
24	$(^2P^o_{3/2})6d\ ^2[1/2]_1$	6	2	-0.649464393	3	-

* Two Notations:[85] (1) Russell-Saunders $^{2S+1}L_J$ notation for Kr ground state $|g\rangle$. (2) Racah $(^{2S_1+1}P^o_{J_1})\ nl^{(2S_1+1)}[K]_J{}^o$ notation for excited Kr states. Note $\vec{K}=\vec{J}_1+\vec{l}$; $\vec{J}=\vec{K}+\vec{s}$; and $\vec{K}=\vec{L}+\vec{S}_1$ [85]. S_1 is the total electron spin of the ion, s is the spin of the excited electron, and L is the total orbital angular momentum. $\vec{S}=\vec{S}_1+\vec{s}$.

to account for the degeneracy of both quantum numbers in an isotropic electric field

$q = 0, \pm 1$. Therefore,

$$\begin{aligned} A_{ij} &= \frac{2e^2\omega_{ij}^3 a_o^2}{3c^3 h\epsilon_o} \sum_{m_i} \frac{1}{\sqrt{w_t}} \sum_{m_j} \sum_{q=0,\pm 1} |\langle n_i l_i m_i | \, \vec{r} \, | n_j l_j m_j \rangle|^2 \\ &= \frac{2e^2\omega_{ij}^3 a_o^2}{3c^3 h\epsilon_o} \left[\langle r \rangle \sqrt{\frac{(2l_i+1)(2l_j+1)}{w_t}} \begin{pmatrix} l_i & 1 & l_j \\ 0 & 0 & 0 \end{pmatrix} \right]^2 \\ &= \frac{2e^2\omega_{ij}^3 a_o^2}{3c^3 h\epsilon_o} \left[\langle r \rangle \frac{1}{\sqrt{3}} \right]^2 \text{ for s} \Leftrightarrow \text{p transitions} \\ &= \frac{2e^2\omega_{ij}^3 a_o^2}{3c^3 h\epsilon_o} \left[\langle r \rangle \sqrt{\frac{2}{9}} \right]^2 \text{ for p} \Leftrightarrow \text{d transitions,} \end{aligned} \tag{2.1.32}$$

where w_t is the number of nonzero transitions produced by the degeneracy of m_i and m_j in an isotropic radiation field. $1/w_t$ is the probability of a transition occurring. See Appendix B for the determination of w_t. For fixed l_i and l_j, the value of w_t can be determined from the number of nonzero Clebsch-Gordon coefficients for varying m_i, m_j, and polarization component q. For $s \leftrightarrow p$ transitions, $w_t = 3$; and for $p \leftrightarrow d$ transitions, $w_t = 9$. Eq. 2.1.32 amounts to practical means to calculate Einstein coefficients from a set of radial wave functions. Results are shown in Table 2.7. For the ground state $|g\rangle$, a Hartree-Fock radial orbital, composed of a linear combination

of Slater-type orbitals, from Clementi et al. [89] is used:

$$\begin{aligned} R_{4p}(r) = \quad & 0.08488 \times \mathrm{STO}(2, 17.03660, r) + \\ & 0.00571 \times \mathrm{STO}(2, 26.04380, r) + \\ & 0.04169 \times \mathrm{STO}(3, 15.51000, r) + \\ & - 0.07425 \times \mathrm{STO}(3, 9.49403, r) + \\ & - 0.26866 \times \mathrm{STO}(3, 6.57275, r) + \\ & 0.01341 \times \mathrm{STO}(4, 5.38507, r) + \\ & 0.51241 \times \mathrm{STO}(4, 3.15603, r) + \\ & 0.42557 \times \mathrm{STO}(4, 2.02966, r) + \\ & 0.18141 \times \mathrm{STO}(4, 1.42733, r), \end{aligned} \tag{2.1.33}$$

where the normalized Slater Type Orbital (STO) function is defined as

$$\mathrm{STO}(n, \zeta, r) = \frac{1}{\sqrt{(2n)!}} (2\zeta)^{(n+1/2)} r^{n-1} e^{-\zeta r}. \tag{2.1.34}$$

This ground-state Hartree-Fock radial wave function assumes a spherically symmetric electric charge distribution and accounts to first order the electron-repulsion exerted on a $4p$ electron. Electron repulsion shields a valence $4p$ electron from the attractive potential of the Kr nucleus, increasing its ground state energy beyond that of a pure one-electron atom of atomic number $Z = 36$. In eq. (2.1.34), ζ is interpreted as a shielding parameter obtained by curve fitting the numerical results of a Hartree-Fock calculation.

In Table 2.7, Einstein coefficients are calculated via Eq. 2.1.32 with varying accuracy but to the correct order of magnitude. The QDT parameter, I_m, is tuned

Table 2.7: Calculation of Einstein Coefficients Using Quantum-defect Functions and Comparison with NIST Experimental Data [85].

NIST				Quantum Defect Theory	
Transition	Wavelength (nm)	$A_{ij}(1/s)$	Acc.**	A_{ij} (1/s)	% Error
$\|23\rangle \rightarrow \|g\rangle$	92.3713	1.14×10^8	C	4.16×10^7	63.5%
$\|24\rangle \rightarrow \|g\rangle$	92.8711	3.87×10^6	C	2.64×10^5	93.2%
$\|22\rangle \rightarrow \|g\rangle$	96.3374	3.35×10^7	C	2.13×10^7	36.3%
$\|20\rangle \rightarrow \|g\rangle$	94.5441	2.81×10^8	C	1.0450×10^8	62.8%
$\|18\rangle \rightarrow \|g\rangle$	95.1056	2.58×10^7	C	6.8928×10^7	167.2%
$\|19\rangle \rightarrow \|g\rangle$	100.1061	3.42×10^8	C	2.68×10^8	21.5%
$\|21\rangle \rightarrow \|g\rangle$	100.3550	1.82×10^8	C	1.37×10^8	24.8%
$\|3\rangle \rightarrow \|g\rangle$	116.4867	3.09×10^8	$A+$	2.33×10^8	24.5%
$\|1\rangle \rightarrow \|g\rangle$	123.5838	2.98×10^8	$A+$	4.97×10^8	66.7%
$\|15\rangle \rightarrow \|2\rangle$	427.5172	1.99×10^6	$C+$	1.74×10^6	12.7%
$\|16\rangle \rightarrow \|1\rangle$	437.7351	3.74×10^6	B	2.45×10^6	34.4%
$\|15\rangle \rightarrow \|1\rangle$	445.5168	3.97×10^5	B	4.92×10^5	23.9%
$\|17\rangle \rightarrow \|1\rangle$	450.3617	7.8×10^5	C	4.59×10^6	488.7%
$\|5\rangle \rightarrow \|1\rangle$	758.7414	4.310×10^7	$A+$	4.77×10^7	10.8%
$\|6\rangle \rightarrow \|2\rangle$	760.1546	2.732×10^7	AA	2.78×10^7	1.8%
$\|12\rangle \rightarrow \|3\rangle$	768.7361	4.064×10^7	AA	2.98×10^7	26.8%
$\|10\rangle \rightarrow \|2\rangle$	769.6658	4.27×10^6	A	2.74×10^7	540.9%
$\|13\rangle \rightarrow \|4\rangle$	785.6984	2.041×10^7	A	2.14×10^7	5.0%
$\|14\rangle \rightarrow \|4\rangle$	806.1721	1.583×10^7	$B+$	2.19×10^7	38.6%
$\|8\rangle \rightarrow \|2\rangle$	811.5132	3.610×10^7	AAA	3.50×10^7	3.10%
$\|6\rangle \rightarrow \|1\rangle$	819.2308	8.94×10^6	A	2.75×10^7	207.3%
$\|11\rangle \rightarrow \|3\rangle$	826.5514	3.416×10^7	AA	2.93×10^7	14.2%
$\|9\rangle \rightarrow \|1\rangle$	877.9161	2.217×10^7	AA	2.43×10^7	9.66%
$\|7\rangle \rightarrow \|3\rangle$	893.1145	2.289×10^7	A	2.24×10^7	2.02%

** NIST estimated accuracy of Einstein Coefficient. $AAA \leq 0.3\%$, $AA \leq 1\%$, $A \leq 3\%$, $B+ \leq 7\%$, $B \leq 10\%$, $C+ \leq 18\%$, $C \leq 25\%$.

to maximize the accuracy of A_{ij}. By obtaining the correct order of magnitude and in some cases the correct Einstein coefficient, Table 2.7 further validates the use of quantum-defect radial wave functions Eq. 2.1.27, reinforcing the justification provided by Fig. 2.5 and Appendix A.

2.2 Calculation of Two-Photon Excitation Cross-sections

With a basis of wave functions calibrated on NIST atomic spectra data, Eqs. 2.1.13 and 2.1.2 are directly evaluated, producing the two-photon cross-section data shown in Fig. 2.4. The values of cross-sections are shown in Tables 2.8, 2.9, and 2.10. When

quantum-defect radial wave functions are used in conjunction with oscillator strength formulas for linear polarization [95], such as

$$\langle i|\,\hat{\epsilon}\cdot\vec{r}\,|j\rangle = \sqrt{\frac{3A_{ij}hc^3\epsilon_o}{2e^2\omega_{ij}}}\sqrt{2J_i+1}\begin{pmatrix} J_i & 1 & J_j \\ 0 & 0 & 0 \end{pmatrix}, \tag{2.2.1}$$

good agreement is obtained with the Richardson et al. [108] excitation spectrum, especially using basis sets 2 and 3, which include d orbitals. In Table 2.11, single-path cross-section results are also calculated and tabulated for comparison to results listed in Table 2.10.

Table 2.8: Two-photon Cross-sections using Basis Set 1: $5s$, $6s$, and $7s$ States.

Basis	Basis Set 1: $\|g\rangle, \|1\rangle, \|2\rangle, \ldots \|17\rangle$					
Theory	Quantum-Defect			Quantum-Defect with Oscillator Strengths		
λ_L (nm)	$\sigma_o^{(2)}$ (cm^4)	$\sigma^{(2)}=\sigma_o^{(2)}g(2\omega_L)$ $(cm^4\cdot s)$	$\frac{\sigma^{(2)}}{\|\|\sigma^{(2)}\|\|_\infty}$	$\sigma_o^{(2)}$ (cm^4)	$\sigma^{(2)}=\sigma_o^{(2)}g(2\omega_L)$ $(cm^4\cdot s)$	$\frac{\sigma^{(2)}}{\|\|\sigma^{(2)}\|\|_\infty}$
192.749	7.02×10^{-37}	2.29×10^{-47}	0.005	1.73×10^{-36}	5.65×10^{-47}	0.016
193.494	5.01×10^{-37}	1.64×10^{-47}	0.003	3.70×10^{-38}	1.21×10^{-48}	0.0003
193.947	7.28×10^{-37}	2.39×10^{-47}	0.005	1.25×10^{-37}	4.10×10^{-48}	0.001
202.316	2.17×10^{-35}	7.39×10^{-46}	0.151	6.67×10^{-37}	2.27×10^{-47}	0.006
204.196	2.55×10^{-35}	8.74×10^{-46}	0.178	3.84×10^{-37}	1.32×10^{-47}	0.004
212.556	1.39×10^{-34}	4.91×10^{-45}	1.000	1.03×10^{-34}	3.63×10^{-45}	1.000
214.769	5.56×10^{-35}	1.98×10^{-46}	0.404	3.30×10^{-35}	1.18×10^{-45}	0.324
216.667	6.23×10^{-35}	2.24×10^{-46}	0.455	3.92×10^{-35}	1.41×10^{-45}	0.388

The resulting approach is a hybrid method for the evaluation of dipole matrix elements, consisting of quantum defect theory and where possible, oscillator strengths. Another contribution of quantum defect theory is the prediction of the sign of the radial matrix element from the evaluation of Eq. 2.1.25. The oscillator strength, Eq. 2.2.1, must retain the same sign as Eq. 2.1.25 and Eq. 2.1.23. This sign determines which excitation pathways make constructive and destructive contributions to the two-photon transition matrix element. Also, wherever Eq. 2.2.1 is used for

Table 2.9: Two-photon Cross-sections using only Basis Set 2: $5s$, $6s$, $7s$, and $4d$ States.

Basis	Basis Set 2: $\|g\rangle, \|1\rangle, \|2\rangle, ... \|18\rangle$					
Theory	Quantum-Defect			Quantum-Defect with Oscillator Strengths		
λ_L (nm)	$\sigma_o^{(2)}$ (cm^4)	$\sigma^{(2)} = \sigma_o^{(2)} g(2\omega_L)$ $(cm^4 \cdot s)$	$\frac{\sigma^{(2)}}{\|\|\sigma^{(2)}\|\|_\infty}$	$\sigma_o^{(2)}$ (cm^4)	$\sigma^{(2)} = \sigma_o^{(2)} g(2\omega_L)$ $(cm^4 \cdot s)$	$\frac{\sigma^{(2)}}{\|\|\sigma^{(2)}\|\|_\infty}$
192.749	2.56×10^{-35}	8.37×10^{-46}	0.094	2.80×10^{-35}	9.15×10^{-46}	0.133
193.494	9.85×10^{-35}	7.42×10^{-46}	0.084	1.60×10^{-35}	5.26×10^{-46}	0.077
193.947	1.73×10^{-35}	5.67×10^{-46}	0.064	1.20×10^{-35}	3.93×10^{-46}	0.057
202.316	1.04×10^{-34}	3.55×10^{-45}	0.400	1.95×10^{-35}	6.61×10^{-46}	0.0963
204.196	9.85×10^{-35}	3.37×10^{-45}	0.381	1.57×10^{-35}	5.39×10^{-46}	0.0784
212.556	2.51×10^{-34}	8.86×10^{-45}	1.000	1.94×10^{-34}	6.87×10^{-45}	1.000
214.769	1.32×10^{-34}	4.71×10^{-45}	0.531	3.95×10^{-35}	1.41×10^{-45}	0.205
216.667	1.38×10^{-34}	4.95×10^{-45}	0.559	6.34×10^{-35}	2.28×10^{-45}	0.331

Table 2.10: Two-photon Cross-sections using only Basis Set 3: $5s$, $6s$, $7s$, $4d$, $5d$, and $6d$ States.

Basis	Basis Set 3: $\|g\rangle, \|1\rangle, \|2\rangle, ... \|21\rangle$					
Theory	Quantum-Defect			Quantum-Defect with Oscillator Strengths		
λ_L (nm)	$\sigma_o^{(2)}$ (cm^4)	$\sigma^{(2)} = \sigma_o^{(2)} g(2\omega_L)$ $(cm^4 \cdot s)$	$\frac{\sigma^{(2)}}{\|\|\sigma^{(2)}\|\|_\infty}$	$\sigma_o^{(2)}$ (cm^4)	$\sigma^{(2)} = \sigma_o^{(2)} g(2\omega_L)$ $(cm^4 \cdot s)$	$\frac{\sigma^{(2)}}{\|\|\sigma^{(2)}\|\|_\infty}$
192.749	6.53×10^{-35}	2.13×10^{-45}	0.206	8.25×10^{-35}	2.70×10^{-45}	0.323
193.494	5.31×10^{-35}	1.74×10^{-45}	0.198	5.08×10^{-35}	1.66×10^{-45}	0.199
193.947	4.46×10^{-35}	1.47×10^{-45}	0.142	4.43×10^{-35}	1.45×10^{-45}	0.174
202.316	1.46×10^{-34}	4.96×10^{-45}	0.479	4.17×10^{-35}	1.42×10^{-45}	0.170
204.196	1.32×10^{-34}	4.53×10^{-45}	0.438	3.25×10^{-35}	1.11×10^{-45}	0.133
212.556	2.92×10^{-34}	1.03×10^{-44}	1.000	2.36×10^{-34}	8.34×10^{-45}	1.000
214.769	1.62×10^{-34}	5.79×10^{-45}	0.559	4.18×10^{-35}	1.49×10^{-45}	0.179
216.667	1.67×10^{-34}	6.01×10^{-45}	0.581	6.33×10^{-35}	2.27×10^{-45}	0.272

the evaluation of a matrix element, the equality, $D_{ij} = D_{ji}$, must be used to ensure symmetry. This properly interfaces quantum-defect theory with oscillator strength formulas, creating the hybrid dipole matrix element evaluation method and thus allowing for the eventual extension of Eq. 2.1.13 to general multiphoton excitation. For

example, for three photon excitation, the entire dipole matrix D is used:

$$M_{fg}^{(3)} = \sum_{k=g}^{N} \sum_{p=g}^{N} D_{fk} G_{kk} D_{kp} G_{pp} D_{pg} = \hat{e}_f^T DGDGD\hat{e}_g. \tag{2.2.2}$$

When using a hybrid dipole matrix element calculation scheme, selection of states with adequate experimental data is crucial for reasonable results. Insufficient transition probability data rendered some state omissions in the finite basis of states listed in Table 2.6. For example, only one $4d$ orbital, state $|21\rangle$, was used in basis sets 2 and 3 (Tables 2.9 and 2.10) because it had the highest observed transition probability of all $4d$ states between itself and ground, and it had the highest experimentally measured, transition probability between itself and a $5p$ state: $|21\rangle \rightarrow |10\rangle$. It was the only state with high transition probabilities between $4d$ and $5p$ levels. More importantly, state $|21\rangle$ exhibited dipole-moment behavior, which could be described by quantum-defect theory. The effect of other $4d$ orbitals on the excitation process is small but can be better determined once more transition probabilities become available for transitions between $4d$ and $5p$ states. However, the inclusion of other $4d$ states will not significantly change the excitation spectrum shown in Fig. 2.4. The same reasoning was made for the inclusion of $5d$ and $6d$ states in basis set 3.

2.3 Comparison of Two-Photon Cross-section Calculations with Experiment

Cross-section calculations are reported for eight excitation lines (192.749 nm, 193.494 nm, 193.947 nm, 202.316 nm, 204.196 nm, 212.556 nm, 214.769 nm, 216.667 nm) in Tables 2.8, 2.9, and 2.10 for basis sets 1, 2, and 3 respectively. Assuming the signal mostly consists of signal arising from (2+1) REMPI, these cross-section calculations are then directly compared to three sets of excitation spectrum data in

Table 2.11: Single-Path Approximation Calculations.

λ_L (nm)	State $\|k\rangle$	State $\|f\rangle$	$\sigma_o^{(2)}$ (cm^4)	$\sigma^{(2)}$ $(cm^4 \cdot s)$	$\frac{\sigma^{(2)}}{\|\|\sigma^{(2)}\|\|_\infty}$
192.749	$\|1\rangle$	$\|15\rangle$	4.73×10^{-37}	1.55×10^{-47}	0.016
193.494	$\|1\rangle$	$\|16\rangle$	1.04×10^{-37}	3.40×10^{-48}	0.004
193.947	$\|1\rangle$	$\|17\rangle$	2.01×10^{-37}	6.60×10^{-48}	0.007
202.316	$\|3\rangle$	$\|12\rangle$	1.40×10^{-35}	4.75×10^{-46}	0.496
204.196	$\|3\rangle$	$\|11\rangle$	2.80×10^{-35}	9.57×10^{-46}	1.000
212.556	$\|1\rangle$	$\|5\rangle$	1.72×10^{-35}	6.08×10^{-46}	0.635
214.769	$\|1\rangle$	$\|6\rangle$	8.54×10^{-35}	3.05×10^{-46}	0.318
216.667	$\|1\rangle$	$\|9\rangle$	2.50×10^{-35}	8.98×10^{-46}	0.939

Table 2.12: Experimental Kr Excitation Signal normalized against 212.556 nm Excitation Signal.

λ_L (nm)	202.316	204.196	212.556	214.769	216.667
Richardson et al. fs-excitation	0.20	0.13	1.00	0.14	0.21
Grib et al. fs-excitation	(-)	(-)	1.00	0.153	(-)
Grib et al. ns-excitation	(-)	(-)	1.00	0.132	(-)
Present Work ns-excitation	(-)	(-)	1.00	0.319	0.290

Fig. 2.7 with good agreement (For convenience, Fig. 2.4 is repeated here to accompany results listed in Tables 2.10, 2.11, and 2.12.). The first experimental data set is from this work's nanosecond excitation at 212.556 nm, 214.769 nm, and 216.667 nm. Excitation lines at lower wavelengths with the setup are not currently accessible. Additionally, we present the Richardson et al. [108] excitation spectrum from a femtosecond laser excitation of Kr at 202.316 nm, 204.196 nm, 212.556 nm, 214.769 nm, and 216.667 nm. This spectrum approximates the impulse/natural response of the Kr atom. Due to the short timescales of excitation of Richardson et al. [108], and due to the closely clustered energies of eight, two-photon excited krypton states, the two-photon cross-section can be compared directly to the fluorescence results. The

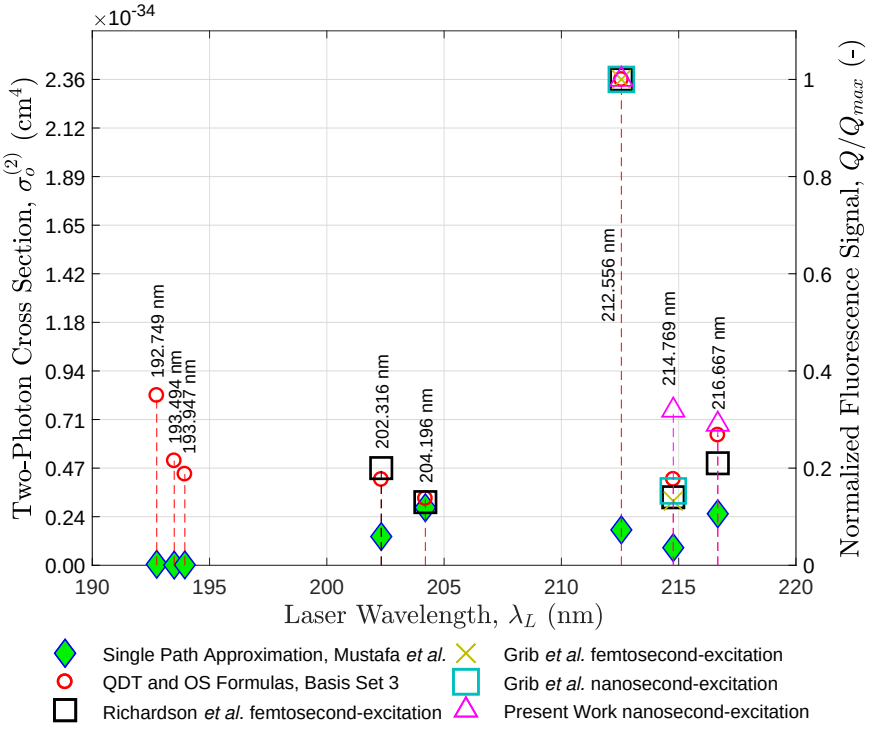

Figure 2.7: Two-photon excitation cross-sections using basis set 3 as the basis of intermediate states, which included $5s$, $6s$, $7s$, $4d$, $5d$, and $6d$ states. Via quantum-defect theory (QDT) and oscillator strength formulas, cross-sections were calculated and compared to the excitation data of Richardson *et al.*, Grib *et al.*, and this work. Richardson data were obtained by fs-laser excitation in a 1 bar, 95% Ar/5% gas mixture. Grib data were obtained by both fs-laser and ns-laser excitations in a 1 atm, 77% N_2/33% Kr gas mixture. This work's data was obtained via ns-laser excitation in 1 torr, 99% N_2/1% Kr gas mixture to minimize collisional effects. Calculated cross-sections and normalized experimental excitation data are listed in Tables 2.10 through 2.12, respectively.

plotted, relative fluorescence signal magnitudes for 212.556 nm and 214.769 nm excitation of Grib et al. [109] also agree with both Richardson et al. [108] excitation spectrum and this work's excitation spectrum, regardless of fs- or ns- laser excitation. Normalized experimental excitation data are listed in Table 2.12 for all considered data sets. In Fig. 2.4, comparison is also made to the single-path approximation, whose cross-section values are listed in Table 2.11. Single-path approximation is unable to reconstruct the experimentally observed excitation spectrum, but it can obtain

rough estimates of cross-sections.

The convergence of the summation over the intermediate basis set $|k\rangle$ is shown in Tables 2.8, 2.9, and 2.10, which agrees with the convergence criterion of Eq. 2.1.7: $n_{max} \leq 7$. The rate of convergence cannot be inferred, but for basis sets 1-3, the Richardson trend is present for the 212.556 nm, 214.769 nm, and 216.667 nm excitation lines.

In Table 2.10, the calculated cross-section for 214.769 nm excitation is 4.18×10^{-35} cm^4. This cross-section agrees well with the experimentally measured 214.769 nm two-photon cross-section of Dakka et al. [110]: $5.2 \pm 2.2 \times 10^{-35}$ cm^4. This validates the order of magnitude and accuracy of calculated cross-sections for basis set 3.

Overall, the comparison of the calculated two-photon cross-sections with the experimental data of multiple research groups is good for lines between 200-220 nm. Cross-sections for lines between 190-200 nm are predictions calculated by the method described within this work. The multi-path, finite basis approximation of the two-photon transition matrix element, $M_{fg}^{(2)}$, generated context for each calculated excitation cross-section. From a first order perturbation calculation, an entire excitation spectrum was constructed with sufficient accuracy. This work improved the effectiveness of first order perturbation theory for multiphoton processes beyond a mere order of magnitude calculation.

2.4 Experimental Setup

Laser-induced fluorescence experiments were performed in a hermetic test cell that had optical ports for a laser and camera. The cell was maintained at room temperature. Two quiescent gas mixtures were used, 99% N_2/1% Kr and 75% N_2/5% Kr/20%

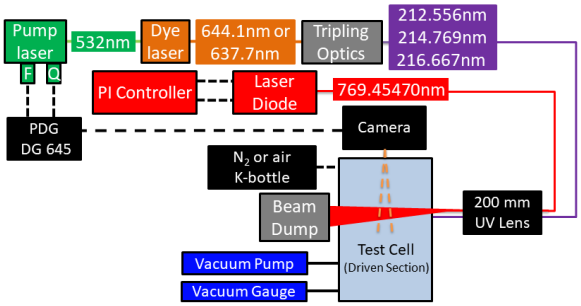

Figure 2.8: Schematic of Experimental Setup. PDG refers to pulse delay generator.

O_2. The pressure was varied from 1-100 torr in the 99% N_2/1% Kr mixture and from 1-50 torr in the 75% N_2/5% Kr/20% O_2 mixture.

A frequency-doubled Quanta Ray Pro-350 Nd:YAG laser pumping a frequency tripled Sirah PrecisionScan Dye Laser (DCM dye, DMSO solvent) is the laser system used for nanosecond REMPI excitation in this work. A schematic of the optical setup is shown in Fig. 2.8. The Nd:YAG laser pumps the dye laser with 1000 mJ/pulse at a wavelength of 532 nm. The dye laser is tuned to output a 637.67/644.31/650.01 nm beam and frequency tripling (Sirah THU 205) of the dye-laser output results in a 212.56/214.77/216.67 nm beam, with 3 mJ energy, 1350 MHz linewidth and 7 ns pulsewidth at a repetition rate of 10 Hz. The write beam was focused into the test section with a 200 mm focal-length, fused-silica lens. The beam fluence and spectral intensity at the waist were 1.28×10^4 J/cm^2 and 1.35×10^3 W/(cm^2 Hz), respectively.

Excitation of the Kr metastable state, $5s[3/2]_2$, was accomplished by a continuous wave 2.65 W Toptica TA Pro Laser diode, which outputted a $\lambda_L = 769.45470$ nm beam in air with a waist of 3.28 mm. The excitation spectrum of the diode is plotted in Fig. 2.9. The diode wavelength was regulated by feedback control on the piezoelectric voltage input of the DCL Pro, which powered the diode. The feedback and control signals were provided by a WS7-4150 Wavelength Meter, which measured the wavelength of the diode to 0.00001 nm precision and implemented the PI-control law.

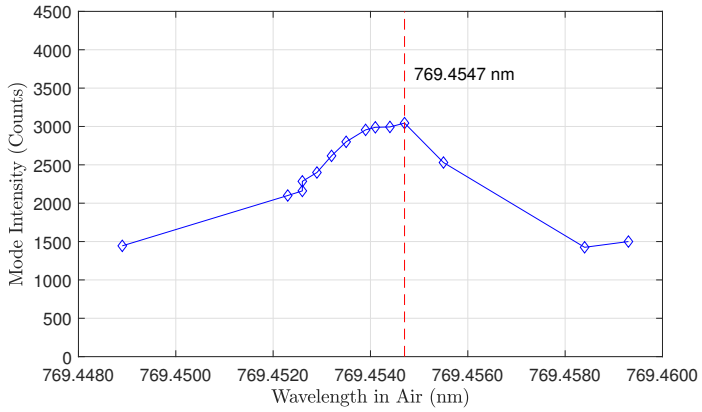

Figure 2.9: Excitation Spectrum for 769.45 nm CW Laser Diode, showing a peak near 769.4547 nm in air. The mode signal represents a camera count measurement with the greatest number of occurrences at a wavelength, measured in air.

Online tuning obtained PI-control gains. The sampling rate of the wavelength meter was set between 90 - 100 ms. In order to prevent saturation of the piezoelectric voltage, manual tuning of the diode diffraction grating via a 2.5 mm Allen key was done to bring the diode within ± 0.02 nm from the desired operating wavelength, prior to the implementation of the control law.

The intensified CCD camera used for all experiments is a Princeton Instruments PIMAX-4 (PM4-1024i-HR-FG-18-P46-CM) with a Nikon NIKKOR 24-85mm f/2.8-4D lens in "macro" mode and positioned approximately 200 mm from the write/read location. The camera gate opens once immediately after the write laser pulse, for 50 ns to capture the fluorescence from transitions C, D, M, N, O in Fig. 2.1. The raw image from the camera was processed using a Gaussian peak finding algorithm from O'Haver [111] to quantify the value of the peak in each row of the fluorescence image. The final value of the signal that is reported is the average value of the peaks in the rows closest to the focus of the tagged line.

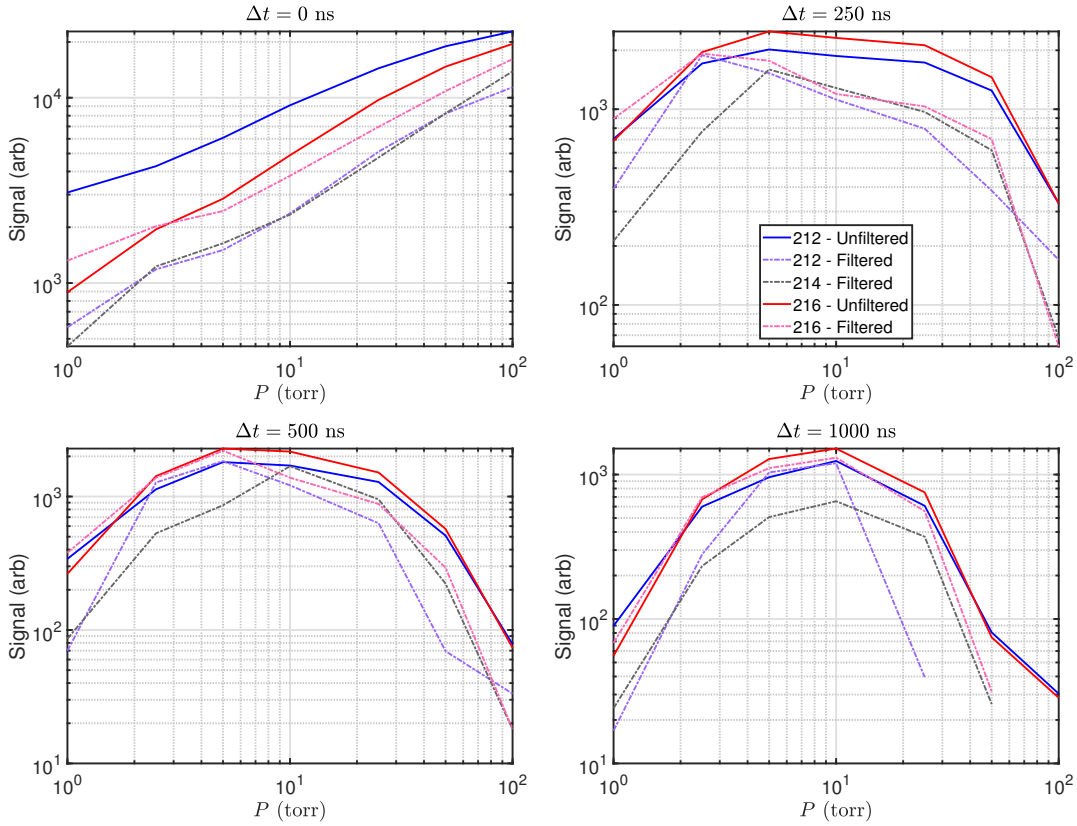

Figure 2.10: Kr Fluorescence signal in 99% N_2/1% Kr at Time Δt after dye laser pulse: (*Top Left*) 0 ns, (*Top Right*) 250 ns, (*Bottom Left*) 500 ns, and (*Bottom Right*) 1000 ns. This is two-laser excitation. A 769.4547 nm continuous diode was used to excite metastable Kr. The filter used was an 800 highpass filter. Seven discrete pressure measurements were made for each time frame.

2.5 Experimental Results

For the excitation spectrum in Fig. 2.4, the data in this work were obtained via ns-laser excitation in 1 torr, 99% N_2/1% Kr gas mixture to minimize collisional effects. However, the excitation spectrum alone does not prove the optimality of the 212.556 nm excitation line with respect to time-dependent phenomena. In Figs. 2.10 and 2.11, a sweep of the pressure-time parameter space was performed at room temperature in two gas mixtures ((1) 99% N_2/1% Kr and (2) 5%-Kr 20%-O_2 75%-N_2) for each of the three excitation lines of interest for use in high-speed, reacting flow. This

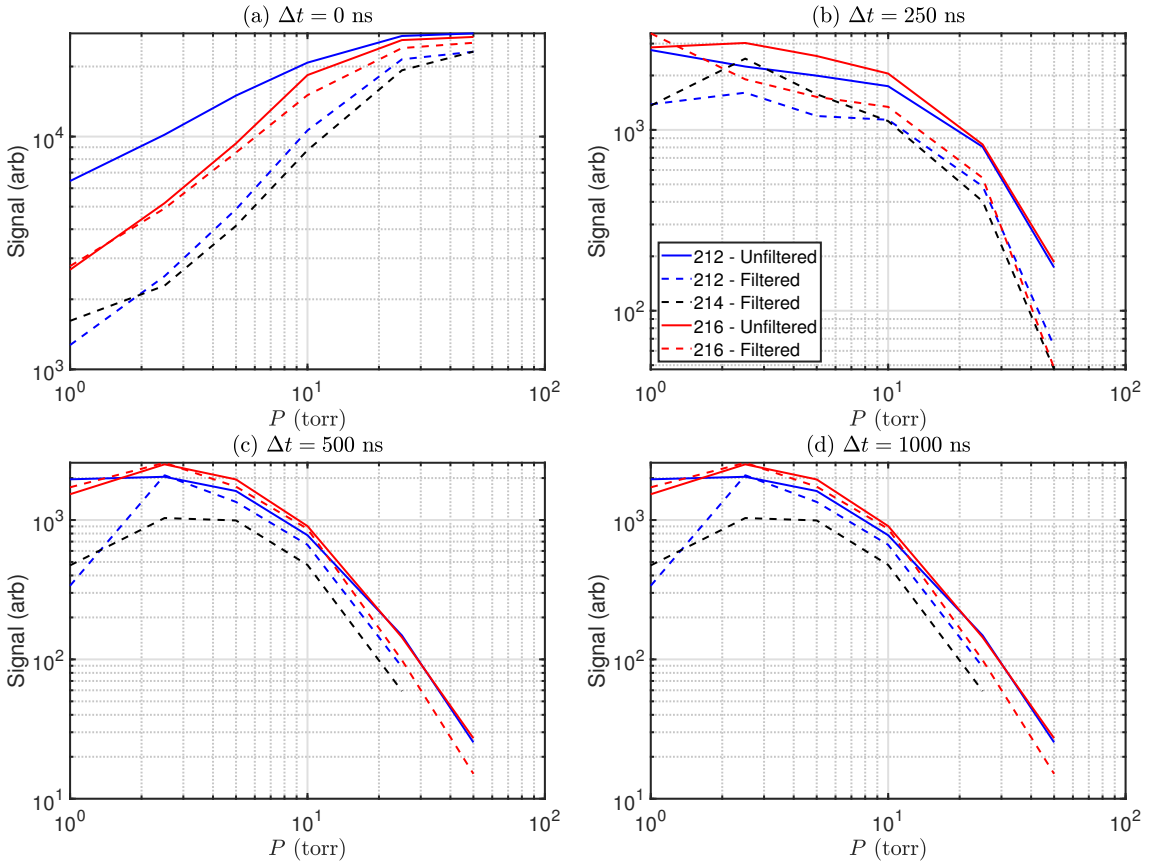

Figure 2.11: Kr Fluorescence Signal in 5%-Kr, 20%-O_2, and 75%-N_2 at Time Δt after laser pulse. (a) 0 ns, (b) 250 ns, (c) 500 ns, and (d) 1000 ns. Seven discrete pressure measurements were made for each time frame.

highlights physical features which would otherwise be difficult to calculate, such as the signal contribution of radiative cascade in a cold, partially ionized Kr plasma and the optimality of laser excitation schemes at different times Δt after the rising edge of the laser pulse, both with and without an 800 highpass filter. The plots assign timescales and weigh the significance of different phenomena, such as two-photon excitation, $(2+1)$ photoionization, metastable excitation, and radiative cascade against the overall Kr fluorescence signal.

2.6 Discussion of Experimental and Theoretical Results

For any single-laser KTV scheme using an excitation line in the 190 - 220 nm range, the 212.556 nm line is optimal, achieving maximum fluorescence from (2+1) REMPI and its resulting afterglow. The excitation spectrum in Fig. 2.4 shows that the single-path approximation is unable to predict two-photon cross-sections, and does not recreate the experimentally observed excitation spectrum. Meanwhile, multi-path, first-order perturbation theory via matrix mechanics successfully does, even agreeing with the experimentally obtained cross-section of [110] of $5.2 \pm 2.2 \times 10^{-35}$ cm^4 for the 214.667 nm excitation line. The excitation spectrum also shows that the two-photon excitation cross-section is the dominant factor in optimizing the single-laser excitation line for Kr, especially considering all lines share approximately the same one-photon ionization cross-section at the two-photon state.

For the 769.4547 nm CW diode-assisted scheme, time-dependent factors beyond the two-photon excitation cross-section were considered, including the collisional de-excitation of the electrons in a partially ionized Kr gas (a cold plasma) by energy exchange with oxygen and nitrogen (and other possible contaminants) [112, 113]. The complicated mechanisms of the recombination processes for a cold Kr plasma precluded kinetic modeling, and therefore, an experimental sweep in pressure-time space was used. For a given read image time Δt, pressure optimality is shown. For $\Delta t \geq 50$ ns, the unfiltered 216.667 nm line outperformed the unfiltered 212.556 nm line. The 800 nm highpass filtered 214.769 nm line was best at 10 torr. However, the filtered 216.667 nm line could be argued to be robustly optimal for $\Delta t \geq 50$ ns for all pressures, which cannot be said for the more sensitive 214.769 nm line. Therefore, for high-speed, high-enthalpy experiments, 216.667 nm was chosen as the excitation line. For a 99% N_2/1% Kr gas mixture, the KTV signal peaks at 10 torr (1.3 kPa). For a

5%-Kr 20%-O_2 75%-N_2 gas mixture, the KTV signal peaks at 2.5 torr (0.33 kPa).

In this chapter, state-of-the-art KTV excitation techniques were introduced discussed. A simplified dipole-moment matrix element formula was derived, and a framework for calculating two-photon cross-sections for all noble gases via multi-path first-order perturbation theory is presented, based on that presented by Lambropoulos [91]. Single-laser KTV line optimization was done, and the optimality of different excitation lines was discussed for a 769.45 nm CW diode-assisted scheme. These results may aid the development of other noble gas tagging techniques which utilize multiphoton processes. This work provides an illustrative calculation for multiphoton excitation cross-sections that may aid members of the hypersonic diagnostics community. This work also shows that excitation of the metastable state, produced from recombination processes or the decay of the two-photon excited state, can alter the optimality of excitation lines in the 210-220 nm regime during the KTV read step.

Chapter 3

Geometrical Transformation to Mitigate Effect of Laser Ablation Plume for Krypton Tagging Velocimetry over a Hollow Cylinder in the Stevens Shock Tube

One option to minimize the significance of laser ablation on test articles is to use a special geometry setup and transformation, as done in [32]. By assuming axisymmetric flow, boundary layer measurements were made tangentially to a sectioned hollow cylinder, instead of normal to a flat plate, in the Stevens Shock Tube (Fig. 3.1). This effectively stretched the boundary layer, increasing near-wall resolution. The write laser excited Kr atoms on a line approximately tangent to the cylinder, and the camera captured the projected image of the line and its displacement (Fig. 3.2a). The locations of tagged Kr atoms on this cylinder were mapped to corresponding wall-normal points over a flat plate to transform the curved surface problem into a flat plate problem. This minimized and sometimes avoided the laser ablation plumes on the test article surface, which obscured the desired fluorescence signal. As a result, the full laser pulse energy of the laser ($\approx$ 10 mJ) could be used while retaining near-wall resolution, as shown in Stevens Shock Tube Shot 94 in Fig. C.1b. Appendix C describes a direct approach to mitigate the size of laser ablation plumes via the application of Teflon®on a test article surface, but unlike the simple geometrical transformation in this chapter, it is unsuitable for the deposition of large laser pulse energies (10 mJ) on a test article surface.

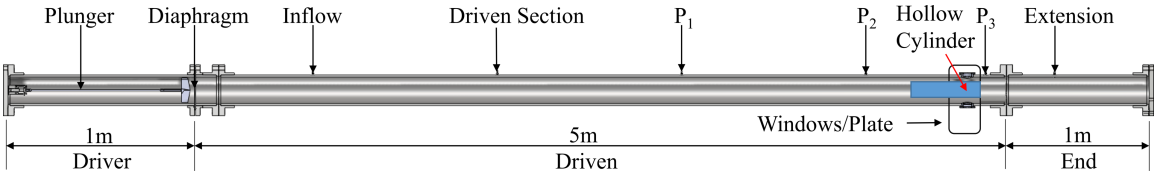

Figure 3.1: Schematic of Stevens Shock Tube with Sectioned Hollow Cylinder Test Article.

3.1 Geometry Setup and Coordinate Transformation

This chapter will expand on the coordinate transformation presented in Mustafa et al. [32] to emphasize an important ablation-mitigation result that will eventually be used in the study of flow over the hollow cylinder flare test article featured in Ch. 5. A schematic of the measurement location in the Stevens Shock Tube is shown in Fig. 3.1. Optical access was provided by three fused-silica windows near the end of the tube. The operation of the shock tube is initiated by a diaphragm-piercing mechanism, consisting of a solenoid-actuated plunger, as depicted in Fig. 3.1. Three pressure transducers are installed along the length of the tube, the most downstream of which is at the measurement location (marked as "P_3" in Fig. 3.1). There is also an additional port used to fill the driven section with gas mixtures. Experiments were performed over a sectioned hollow cylinder with a sharp leading edge positioned $x = 43 \pm 3$ mm ahead of the measurement location in the shock tube test section. The measurement location was in a region of laminar flow.

From Mustafa et al. [32], Fig. 3.2 depicts a sketch of a laser beam striking the cylinder (a pipe with a sharp leading edge). Flow is out of the page and is assumed to be axisymmetric with respect to the cylinder axis. The diagram aids in the derivation of the mapped wall-normal location, y, as a function of the measurement distance y_m (the quantity measured from camera images) from the wall location to an observed point of fluorescence, the radius R of the pipe, the angular offset θ from the true

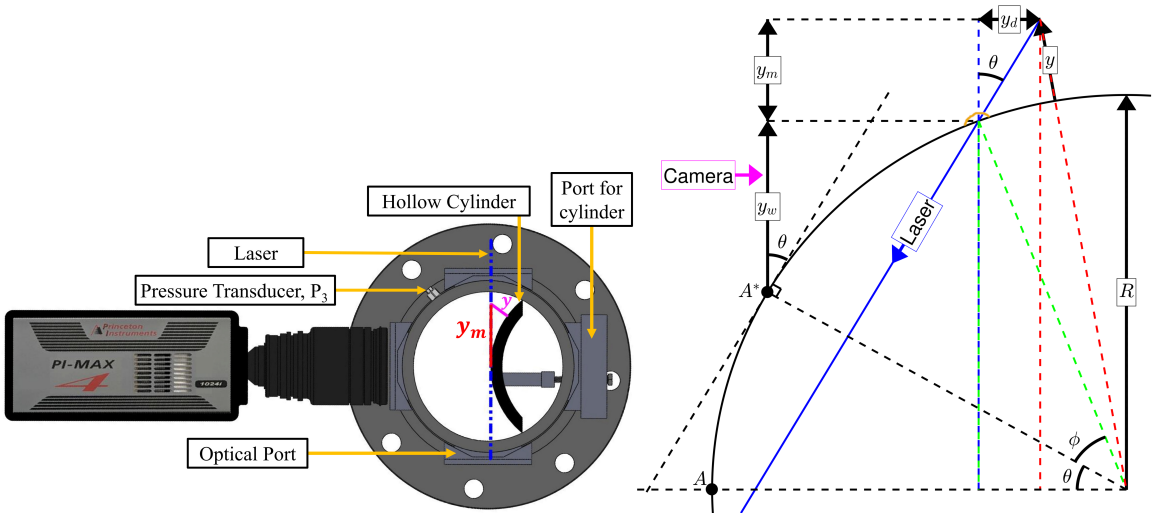

(a) Camera and Laser Setup (b) Sketch of Geometry

Figure 3.2: Geometry of Laser Setup with Respect to the Hollow Cylinder Surface. (a) Camera and Laser Setup over Hollow Cylinder (flow direction is out of the paper). (b) Sketch of Geometry showing relationship between boundary layer coordinate y and measured camera image coordinate y_m. An orange arc segment denotes the location of laser wall ablation on the hollow cylinder test article.

apogee A and the wall location y_w from the observed apogee A^*. The derivation of the mapping expression for y from y_m uses this geometry, beginning with the green and red triangles drawn in the sketch. From the green triangle, a relationship between θ and ϕ is obtained as

$$\sin(\theta + \phi) = \frac{R\sin(\theta) + y_w}{R}. \tag{3.1.1}$$

Solving (3.1.1) for ϕ,

$$\phi = \arcsin\left(\frac{R\sin(\theta) + y_w}{R}\right) - \theta. \tag{3.1.2}$$

In order to find the height of the red triangle, the distance y_d is found via,

$$y_d = y_m \tan(\theta). \tag{3.1.3}$$

Applying the Pythagorean Theorem to the red triangle yields the final expression for the wall-normal distance,

$$y = \sqrt{(R\cos(\theta+\phi) - y_d)^2 + (R\sin(\theta) + y_m + y_w)^2} - R. \tag{3.1.4}$$

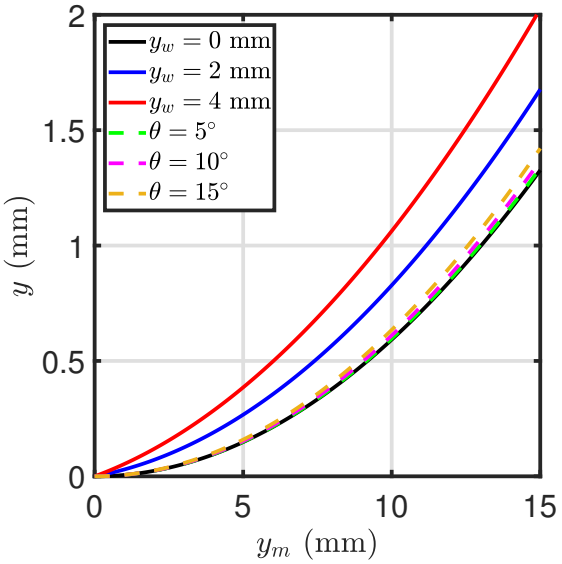

Figure 3.3: Effect of θ and y_w on Mapping. The the transformation $y_m \rightarrow y$ allows approximately quadratic magnification of the boundary layer. Meanwhile, laser ablation plumes are effectively demagnified by the transformation.

Fig. 3.3 displays a parameter sweep of θ and y_w to measure their impact on y. A more effective way to judge the geometry transformation, Eq. 3.1.4, is to simplify the expression for y, using small angle approximation ($\phi \leq 10°$and $\theta \leq 10°$). By approximating $\sin(\theta) \approx \theta$, $\cos(\theta) \approx 1$, $\tan(\theta) \approx \theta$, and $\arcsin(\theta) \approx \theta$, Eq. 3.1.1 becomes

$$\begin{aligned} \phi &= \arcsin\left(\frac{R\sin(\theta) + y_w}{R}\right) - \theta \\ &\approx \left(\frac{R\theta + y_w}{R}\right) - \theta \\ &\approx \frac{y_w}{R}. \end{aligned} \tag{3.1.5}$$

The simplification of Eq. 3.1.4 is a bit more involved. Using Eq. 3.1.1,

$$\begin{aligned}\cos(\phi+\theta) &= \sqrt{1-\sin^2(\phi+\theta)} \\ &= \frac{\sqrt{R^2\cos^2\theta - y_w^2 - 2Ry_w\sin\theta}}{R}.\end{aligned} \tag{3.1.6}$$

Then Eq. 3.1.4 can be rewritten exactly as

$$\begin{aligned}y &= \sqrt{(R\cos(\theta+\phi)-y_d)^2+(R\sin(\theta)+y_m+y_w)^2} - R \\ &= \big\{R^2\cos^2(\theta) - y_w^2 - 2Ry_w\sin(\theta) - 2Ry_d\cos(\theta+\phi) + y_d^2 \\ &\quad + R^2\sin^2(\theta) + 2R(y_m+y_w)\sin(\theta) + (y_m+y_w)^2\big\}^{\frac{1}{2}} - R \\ &= \big\{R^2 - 2Ry_m\tan(\theta)(\cos(\theta)\cos(\phi)-\sin(\theta)\sin(\phi)) \\ &\quad + y_m^2(1+\tan^2(\theta)) + 2Ry_m\sin(\theta) + 2y_wy_m\big\}^{\frac{1}{2}} - R \\ &= \sqrt{R^2 + 2y_my_w + y_m^2\sec^2(\theta) + 2Ry_m\sin(\theta)\left(1-\cos(\phi)+\tan(\theta)\sin(\phi)\right)} - R,\end{aligned} \tag{3.1.7}$$

remembering $y_d = y_m\tan(\theta)$. Applying small angle approximation and using Eq. 3.1.5, Eq. 3.1.7 becomes

$$\begin{aligned}y &\approx \sqrt{R^2 + 2y_my_w + y_m^2\sec^2(\theta) + 2Ry_m\theta^2\phi} - R \\ &\approx \sqrt{R^2 + 2y_my_w + y_m^2\sec^2(\theta) + 2y_wy_m\theta^2} - R \\ &\approx R\left(1 + \frac{2y_my_w + y_m^2\sec^2(\theta) + 2y_wy_m\theta^2}{R^2}\right)^{\frac{1}{2}} - R \\ &\approx R\left(1 + \frac{2y_my_w + y_m^2\sec^2(\theta) + 2y_wy_m\theta^2}{2R^2} + \dots\right) - R \\ &\approx \frac{2y_my_w + y_m^2\sec^2(\theta) + 2y_wy_m\theta^2}{2R} \\ &\approx \frac{2y_my_w + y_m^2\sec^2(\theta)}{2R} + \frac{y_wy_m\theta^2}{R} \\ &\approx \frac{2y_my_w + y_m^2\sec^2(\theta)}{2R},\end{aligned} \tag{3.1.8}$$

where $\theta^2 \approx 0$ and $\sqrt{1+x} \approx 1 + \frac{x}{2}$. If one does not approximate $\sec^2(\theta)$ as 1, one can obtain the trends shown in the Fig. 3.3 as follows:

$$y \approx \frac{y_m y_w}{R} + \frac{y_m^2 \sec^2(\theta)}{2R}. \tag{3.1.9}$$

Now, it is safe to assume $\sec^2(\theta) \approx 1$.

Taking the derivative with respect to the image coordinate y_m yields

$$\frac{\partial y}{\partial y_m} \approx \frac{y_w + y_m}{R}. \tag{3.1.10}$$

The same result would be reached from the full derivative

$$\frac{\partial y}{\partial y_m} = \frac{R\sin(\theta)(1 - \cos(\phi) + \tan(\theta)\sin(\phi)) + y_m \sec^2(\theta) + y_w}{\sqrt{(R\cos(\theta+\phi) - y_d)^2 + (R\sin(\theta) + y_m + y_w)^2}} \tag{3.1.11}$$

$$\approx \frac{y_w + y_m}{R}. \tag{3.1.12}$$

3.2 Conclusions

The derivative $\frac{\partial y}{\partial y_m}$ describes the attenuation by a factor of a least (y_m/R) of the ablation plume at the surface of the hollow cylinder by the coordinate transformation. The derivative is significantly less than one, clearly showing that y_m effectively stretches the boundary layer coordinate, y, by a factor of $R/(y_w + y_m)$. Therefore, it is advantageous to maximize the radius of the hollow cylinder test article. Of critical importance is that the slope at y_m = 0-5 mm, $\frac{\partial y}{\partial y_m} \approx \frac{y_m + y_w}{R}$, is small. Laser ablation plumes are demagnified by a factor of $\frac{\partial y}{\partial y_m}$ = 2-7 mm/84 mm = 0.02-0.08, which is advantageous. Meanwhile, the boundary layer is stretched out in coordinate y_m by a factor of $\partial y_m/\partial y = R/y_m$, and the plume size remains unchanged in coordinate y_m. Additionally, it is important to minimize $|\theta|$ to minimize $\frac{\partial y}{\partial y_m}$.

The effectiveness of the transformation is demonstrated by KTV over a hollow cylinder in the Stevens Shock Tube, as described in Mustafa et al. [32], in which the transformation ensured near-wall resolution of the boundary during each consecutive shock tube experiment.

Chapter 4

Krypton Tagging Velocimetry in High Speed, High Enthalpy Flow

A major outcome of Mustafa et al. [32] was the implementation of KTV in a large-scale, high-enthalpy impulse hypersonic facility, like the Caltech T5 Piston-Driven Reflected-Shock Tunnel. There is little or no experimental velocimetry data in the literature at high-enthalpy conditions due to the difficulties of performing experiments in impulse facilities [9, 114]. As such, there is no experimental data with which computational researchers can use to validate their modeling efforts in capturing the relevant physics of non-equilibrium thermochemistry and the Navier-Stokes equations. A review of these modeling efforts may be found in [115, 116]. This lack of experimental techniques to make measurements in these high-enthalpy flows slows the progress of fundamental hypersonic flow-physics research and hypersonic vehicle development [117].

In this chapter, KTV is used to measure velocity profiles in the freestream of the T5 Reflected-Shock Tunnel [118] at the California Institute of Technology. The results from an experimental campaign are discussed, where the flow conditions were varied through much of the T5 parameter space (reservoir enthalpy range: $h_R \approx 5$ - 16 MJ/kg). The experimentally-obtained freestream velocity-profile measurements are compared to reacting, Navier-Stokes nozzle calculations with good agreement. Finally, some of the limitations of the present measurement technique are discussed, including quenching effects and flow luminosity. An uncertainty estimate is made for freestream velocity computations, which accounts for the experimentally-derived inputs to the nozzle code. A new approach to KTV image processing is presented.

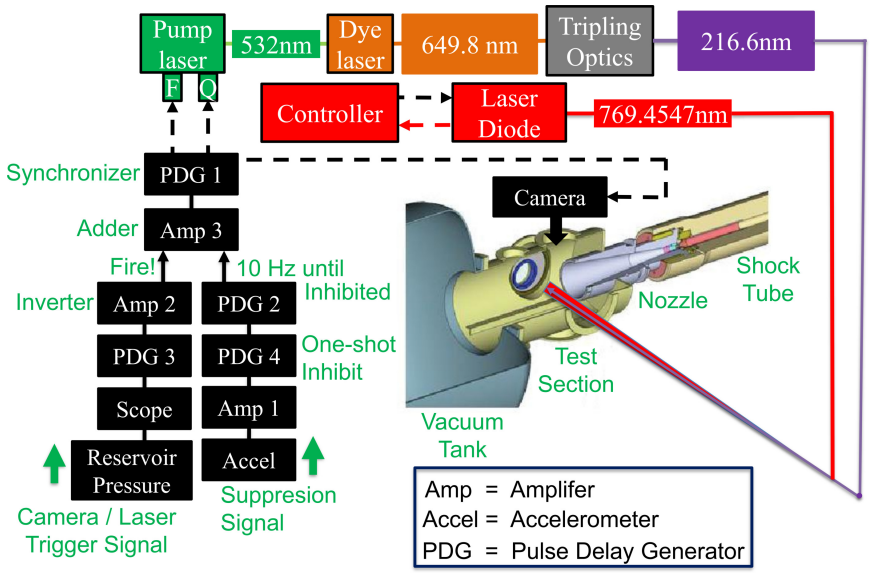

Figure 4.1: Experimental Setup. The timing of the experiment is shown in Figs. 4.2 and 4.3.

4.1 Experimental Setup

4.1.1 Laser and Camera Setup

Based on the results from the pressure-time parameter sweep described in Ch. 2 (Figs. 2.10 and 2.11) for a write laser with a 769.4547 nm CW laser diode, the 216.667 nm line was selected as the excitation line for KTV in the T5 shock tunnel. The 216.667 nm excitation line fulfilled two criteria. For unfiltered imaging, it is optimal over the examined pressure-time space for both 75% N_2/20% O_2/5% Kr and 99% N_2/1% Kr gas mixtures, offering flexibility in tunnel run conditions; and its fluorescence lies primarily within the 800 - 850 nm wavelength range (see Fig. 2.1c and Table 2.1), which is crucial for avoiding the effects of freestream luminosity in the T5 tunnel that would otherwise saturate the camera and prevent imaging the KTV signal.

The write-laser system for this KTV investigation is a frequency-doubled

Quanta Ray Pro-290 Nd:YAG laser and a frequency tripled Sirah PrecisionScan Dye-Laser (DCM dye, DMSO solvent). A schematic of the optical setup is shown in Fig. 4.1. The Nd:YAG laser pumps the dye-laser with 500 mJ/pulse at a wavelength of 532 nm. The dye-laser is tuned to output a 650.01 nm beam, and frequency tripling (Sirah THU 205) of the dye-laser output results in a 216.67 nm beam, with 4 mJ of energy entering the test section, a 1350 MHz linewidth, and a 7 ns pulsewidth at a repetition rate of 10 Hz. The write beam was focused into the test section, near the centerline of the nozzle, just downstream of the exit plane of the nozzle with a 1000 mm focal-length, fused-silica lens. The beam fluence and spectral intensity at the waist were 1.5×10^3 J/cm^2 and 1.6×10^2 W/(cm^2 Hz), respectively. Additionally, data is presented with sufficient SNR at least 20-35 mm away from the focal point where the beam fluence and spectral intensity are lower, 87 J/cm^2 and 9.2 W/(cm^2 Hz), respectively.

The read laser was a Topica TA Pro 2 Watt, CW Laser Diode that generated the 769.4547 nm laser radiation to excite the metastable Kr state. As shown in Fig. 4.1, the diode's beam is directed into the test section to overlap with the write beam. The beam output is approximately 15 mm x 15 mm in size at the location of the write beam focus (where the KTV measurement is made), resulting in an intensity of $\approx$ 900 mW/cm^2. This intensity is several orders of magnitude larger than the saturation intensity estimated from Chapter 7 of [93]. A laser diode is much easier to manage than a second pulsed dye-laser, as was used previously for KTV involving 214.7 nm excitation scheme. With little increase in the complexity of the laser setup, the laser diode increases the SNR of the KTV read image. A feedback loop for wavelength reference tracking was implemented to lock the diode on the desired wavelength with the WS7-4150 Wavelength Meter.

The intensified CCD camera used for all experiments was a Princeton Instru-

ments PIMAX-4 (PM4-1024i-HR-FG-18-P46-CM) with two one-inch lens tubes and an AF-S NIKKOR 200 mm f/2G ED-VR-II prime lens positioned approximately 500 mm from the write/read location. To maintain a frame rate greater than 20 Hz, a region of interest 1020 × 512 was selected from a 1024 × 1024 frame, and the image was binned by 6 in the radial/vertical coordinate. The camera gate opened twice: once for 5 ns immediately following the write-laser pulse and again at a prescribed delay time of 500 ns for 50 ns to capture the transitions from the read step. The flow luminosity in the T5 tunnel obscured the fluorescence signal, either by influencing the shape of the imaged signal or saturating the CCD sensor of the camera. To mitigate this, three 800 nm high pass and two 850 nm low pass filters were placed in front of the camera. The filters also decreased the KTV signal; however, this did not outweigh the benefit of reducing the effect of the flow luminosity. A typical image scale of ≈32 pixels/mm was recorded before each shot, using Gaussians fitted to the white space between the 1 mm markings on a Pocket USAF Optical Test Pattern card.

4.1.2 T5 Reflected-Shock Tunnel

All measurements were made in T5, the free-piston-driven reflected-shock tunnel at the California Institute of Technology. It is the fifth in a series of shock tunnels designed to simulate high-enthalpy, real gas effects on the aerodynamics of vehicles flying at hypervelocity speeds through the atmosphere. More information regarding the capabilities of T5 can be found in [118]. In Fig. 4.1, the schematic shows the driven section of the shock tube, the nozzle, and the test section along with the equipment required for KTV in T5.

To calculate the freestream run conditions, the conditions of the nozzle reservoir are first determined for each experiment. Using the initial driven section pressure, P_1, and the measured incident shock speed U_s, the thermodynamic state is evaluated

Table 4.1: T5 Experimental Conditions Grouped Approximately by Reservoir Enthalpy. Shot refers to the experimental shot number. Gas composition is given in percent by mole. P_R, T_R, and h_R are the reservoir pressure, temperature, and mass-specific enthalpy, respectively. P_∞, T_∞, ρ_∞, M_∞, U_∞, and Re_∞^{unit} are the freestream pressure, temperature, density, Mach number, and unit Reynolds number, respectively.

Set	Shot	Test Gas			P_R	T_R	h_R	P_∞	T_∞	ρ_∞	M_∞	U_∞	Re_∞^{unit}
		% Kr	% N_2	% O_2	(MPa)	(K)	(MJ/kg)	(kPa)	(K)	(kg/m^3)		(m/s)	(1/m)
1	2909	3	97	0	19.9	4483	4.94	4.07	444	0.032	7.16	2983	4.61×10^6
	2910	1	99	0	20.4	4489	5.18	4.44	461	0.033	7.02	3039	4.03×10^6
	2926	1	99	0	14.8	3948	4.57	3.97	421	0.032	6.80	2850	3.81×10^6
	2927	5	75	20	18.1	3700	4.65	5.63	552	0.035	6.09	2836	3.56×10^6
2	2928	1	99	0	16.6	6097	7.87	3.97	723	0.019	6.71	3675	2.00×10^6
	2929	5	75	20	17.3	5024	7.55	6.50	1037	0.021	5.50	3502	1.81×10^6
3	2930	1	99	0	20.7	8335	15.7	7.24	1665	0.014	5.80	4894	1.25×10^6
	2931	1	99	0	21.0	8376	15.9	7.45	1695	0.014	5.14	4940	1.26×10^6
4	2933	1	99	0	22.4	5379	6.60	5.52	611	0.030	6.75	3400	3.39×10^6

for the portion of test gas that has been processed by both the incident and reflected shocks. We assume the pressure of this state isentropically expands to the reservoir pressure, P_R, which accounts for weak expansion or compression waves that are reflected between the contact surface and the shock tube end wall. These calculations were performed using Cantera [119] with the Shock and Detonation Toolbox [120]. The thermodynamic data are found in the literature [121, 122]. Following the evaluation of the reservoir condition, the steady expansion through the contoured nozzle from the reservoir to the freestream is computed by the University of Minnesota Nozzle Code which modeled the flow with the axisymmetric, reacting Navier-Stokes equations and the Spalart-Allmaras turbulence model [123–126]. Finally, the three test-gas mixtures were: (1) 97% N_2/3% Kr, (2) 99% N_2/1% Kr, and (3) 75% N_2/20%O_2/5% Kr.

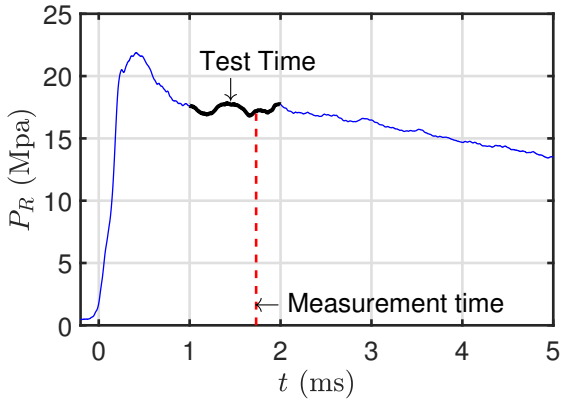

Figure 4.2: Representative Pressure Reservoir Trace. The trace is shown for Shot 2929. The considered test time is 1 - 2 ms, denoted by a thick black lineweight on the pressure trace.

4.1.3 Timing Scheme for Data Acquisition

A timing scheme was implemented to synchronize the time of laser pulsing and camera image acquisition with the firing of the T5 reflected-shock tunnel. The fundamental design requirements of the scheme were to 1) pulse the dye-laser at 10 Hz to maintain its operating temperature, 2) during a tunnel run, suppress the 10 Hz signal, and 3) pulse the dye-laser and trigger the camera once, at the time of measurement. The time of the KTV measurement was set to be 0.6 - 1.8 ms after the reservoir pressure P_R has been established. A representative P_R trace is shown in Fig. 4.2. This choice of delay time is made such that the measurement occurs after the nozzle start-up (1 ms in Fig. 4.2), but before driver-gas contamination or arrival of the expansion fan (2 ms in Fig. 4.2). The choice of delay time is determined by referencing past T5 experiments; see, for example, more details on driver-gas contamination in [127] and [128].

Fig. 4.1 illustrates how the timing scheme controls the dye-laser and camera, noting that the CW laser is left on throughout the experiment. Pulse delay generator (PDG) 2 provides a 10 Hz pulse to the dye-laser and camera. Amplifier (AMP) 3

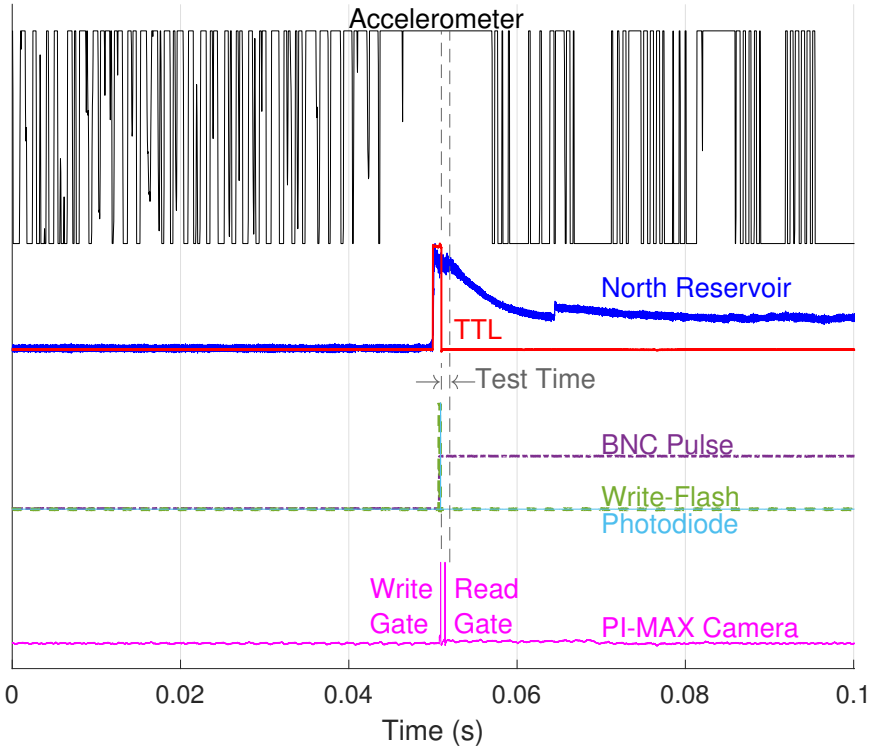

Figure 4.3: Representative Timeline of Timing Scheme. Traces are from Shot 2931.

adds the contributions of PDG 2 and PDG 3. The output of AMP 3 triggers PDG 1, which synchronizes the triggering of the dye-laser and camera 1.5 ms after the rising edge of each trigger pulse. At the start of the tunnel run, an accelerometer senses the tunnel recoil and triggers PDG 4, which sends a single, one-shot inhibit signal to PDG 2, thus suppressing the 10 Hz signal for 10 seconds. Once the incident shock is reflected at the end of the shock tube, the reservoir pressure rises sufficiently for the reservoir pressure transducer to trigger in sequence an oscilloscope and PDG3, which sends a TTL pulse to AMP 2. The TTL pulse is inverted by AMP 2 and is subtracted by AMP 3. Signals produced by PDG 2 and PDG 3 are essentially added. Through AMP 3, this TTL pulse both fires the dye-laser and triggers the camera 0.6-1.8 ms after the rising edge of the reservoir transducer. The timeline of the scheme is shown in Fig. 4.3.

The length of the pause that the laser system experiences is less than 200 ms. This is the time between the accelerometer inhibiting the laser and the reservoir pressure triggering it to make the measurement. This is the time between the T5 piston starting to move and the establishment of reservoir pressure. 200 ms is longer than the 10 Hz operating frequency, but it was observed that there was an acceptable loss of power in the dye-laser during the "write pulse."

4.2 Results

In this section, results are presented for the experiments in N_2 and air. Corresponding flow conditions and gas mixtures are listed in Table 4.1. To process the KTV exposures, the line centers were found in the following manner:

1) An image was cropped to an appropriate field of view and normalized. For each row in the image, the mean was subtracted off, and row elements were normalized by the row maximum. This resulted in some horizontal streakiness in the processed images.

2) A two-dimensional Wiener adaptive-noise removal filter was applied [129, 130]. The Wiener-filter stencil was 1 pixel in the streamwise direction and 8 pixels in the spanwise direction.

3) Fourier filtering is performed by transforming into wavenumber space and applying a low-pass filter that removed structures with wavenumbers above 800 1/m in the spanwise-direction [131, 132]. Without the Fourier filtering in the spanwise direction, obtaining consistent results for the higher-enthalpy cases would not have been possible.

4) The Gaussian peak finding algorithm from [111] was applied to find the line centers for the top row using the lines in the top row of each image as a first guess.

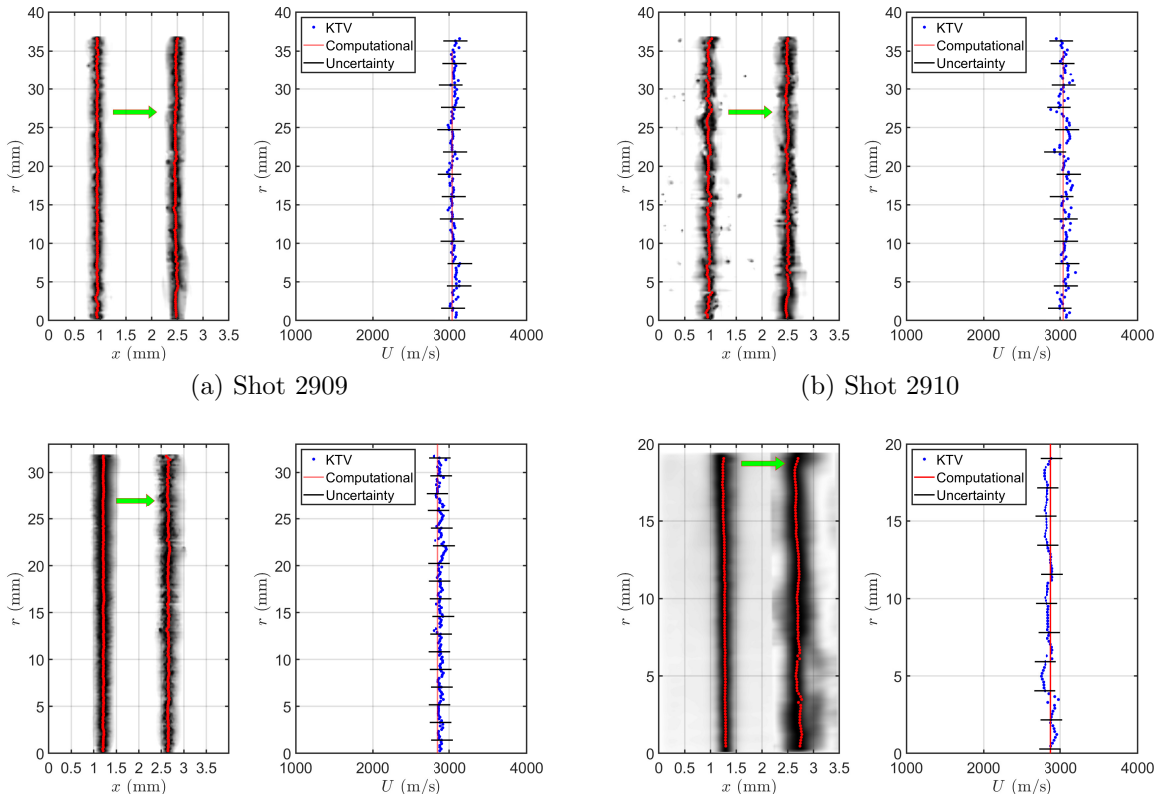

(a) Shot 2909 (b) Shot 2910

(c) Shot 2926 (d) Shot 2927

Figure 4.4: T5 Shots with Reservoir Enthalpy of Approximately 4.5-5 MJ/kg and Freestream Pressure of 4.07-5.63 kPa. In each subfigure, *left* is the concatenation of processed write and read KTV images (inverted Scale); and *right* is the KTV-obtained velocity profile in blue, error bars in black, and computational results in red. The time of displacement is Δt =500 ns. Gas mixtures were 97% N_2/3% Kr (a), 99% N_2/1% Kr (b and c), and 75% N_2/20% O_2/5% Kr (d).

5) Proceeding from the top-down, the Gaussian peak finding algorithm from [111] was applied to find the line centers for each row using the line center location immediately above as the guess.

Error bars for the KTV measurements are calculated in the same fashion as

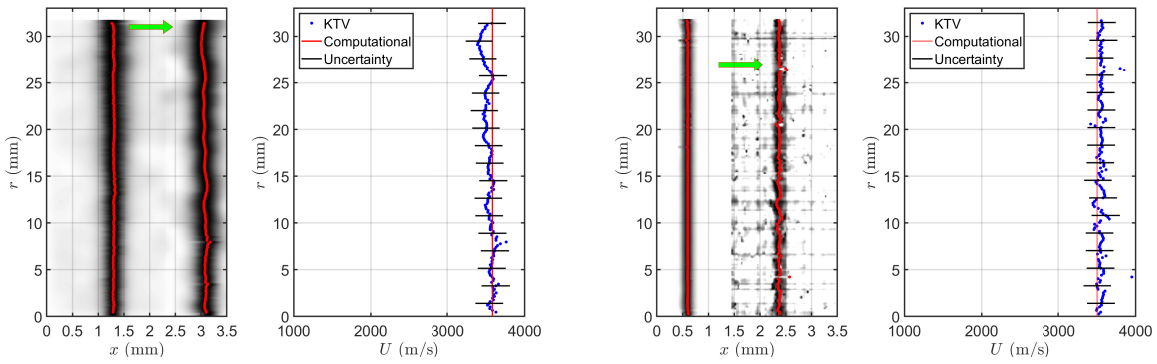

(a) Shot 2928 (b) Shot 2929

Figure 4.5: T5 Shots with Reservoir Enthalpy of Approximately 7-8 MJ/kg and Freestream Pressure of ≈6.5 kPa. Same layout as Fig. 4.4. Gas mixtures were 99% N_2/1% Kr (a), and 75% N_2/20% O_2/5% Kr (b).

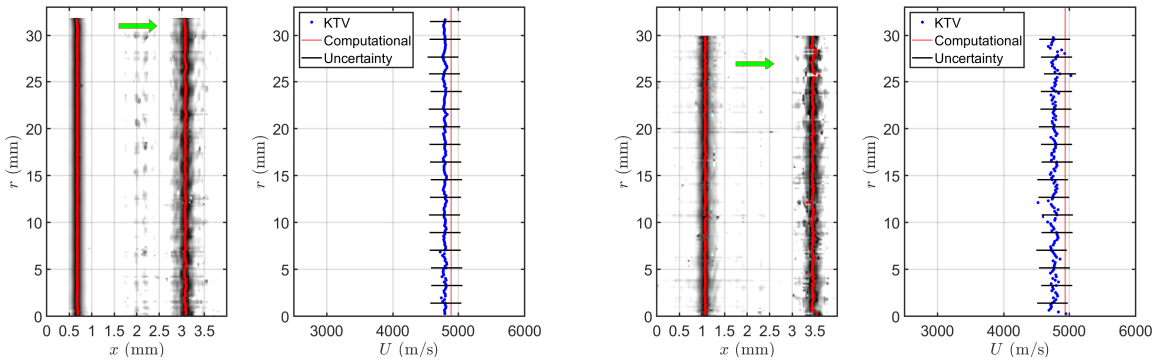

(a) Shot 2930 (b) Shot 2931

Figure 4.6: T5 Shots with Reservoir Enthalpy of 16.7-16.9 MJ/kg and Freestream Pressure of 9.44-9.59 kPa. Same layout as Fig. 4.4. Gas mixtures are 99% N_2/1% Kr (a and b).

Zahradka et al. [25]:

$$\widetilde{U}_{\mathrm{KTV}} = \left[\left(\widetilde{\Delta x} \frac{\partial U}{\partial \Delta x} \right)^2 + \left(\widetilde{\Delta t} \frac{\partial U}{\partial \Delta t} \right)^2 + \left(v'_{RMS} \frac{\partial U}{\partial y} \Delta t \right)^2 \right]^{\frac{1}{2}}, \tag{4.2.1}$$

where uncertainty estimates of a variable are indicated with a tilde and $U = \Delta x / \Delta t$. The uncertainty in the measured displacement distance, $\widetilde{\Delta x}$, of the excited Kr tracer

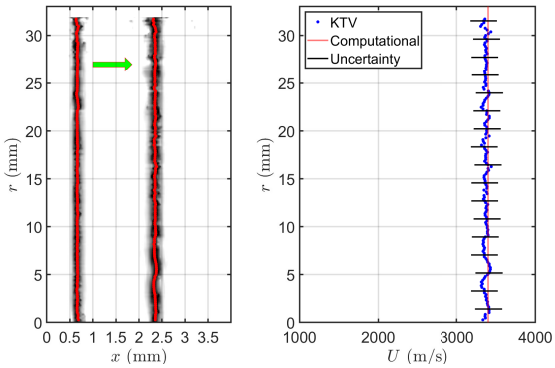

Figure 4.7: Shot 2933 with Reservoir Enthalpy of 6.7 MJ/kg and Freestream Pressure of 8.07 kPa. Same layout as Fig. 4.4. Gas mixture was 99% N_2/1% Kr.

is estimated as the 95% confidence bound on the write and read locations from the Gaussian fits, ≈10 microns. The uncertainty in time, $\widetilde{\Delta t}$, is estimated to be half the camera gate width, 50 ns, causing fluorescence blurring [133]. The third term in Eq. 4.2.1 is uncertainty in streamwise velocity due to wall-normal fluctuations in the xy-plane [133, 134], where v'_{RMS} is estimated as the mean of the wall-normal velocity at the nozzle exit, approximately 40 m/s. The third term in Eq. 4.2.1 is relatively small in these experiments because there is little slope in the measured profiles. Meanwhile, the first term is dominant because it scales with freestream velocity U.

The results for shots 2909, 2910, 2926-2931, and 2933 are shown in Figs. 4.4-4.7. For each experiment, the plot on the left is the concatenation of normalized write and read KTV images. Peaks of Gaussian fits (in red) are plotted on these images. The plot on the right shows the derived KTV velocity profile in blue, the uncertainty estimate as black bars, and the computational results in red. The field of view of the KTV measurements is 20 - 35 × 3.5 mm and the uncertainty is typically 5% of the freestream value. The zero in Figs. 4.4-4.7 marks the centerline of the nozzle, and the measurement was made immediately downstream of the exit plane of the nozzle.

4.3 Evaluation of Lowpass 2D-Fourier Filtering

Lowpass Fourier-Filtering was in the image processing of Figs. 4.4-4.7. According to [135], the 2D Fourier Transform of an arbitrary two-dimensional matrix and the corresponding inverse transform are unitary, meaning they do not distort the original signal. The circular window/mask function is a lowpass filter in wavenumber space [136, 137]. A test was prepared to evaluate the effectiveness of 2D Fourier Filtering in image processing. As shown in Fig. 4.8, a test signal function, simulating the shape of a boundary layer, is superimposed with a noise function:

$$F = a \exp\left(-c\left(b + g\left(1 - \exp\left(-\frac{y-11}{d}\right)\right) - x\right)^2\right) + n z_{\text{rand}}(x,y), \qquad (4.3.1)$$

with $a = 1$, $b = 75$, $c = 0.005$, $d = 20$, and $g = 50$ where $z_{\text{rand}}(x,y)$ is a random white noise process with range 0 to 1. The noise amplitude is related to the SNR via the relationship, $\text{SNR} = \frac{a}{n}$. The signal-to-noise ratio, SNR, is varied from 0.05 to 1.00 to show the effectiveness of 2D Fourier Filtering. The original KTV signal 4.8 is distorted by random noise of amplitude $n = \frac{a}{\text{SNR}}$. The left-hand figures of Figs. 4.9

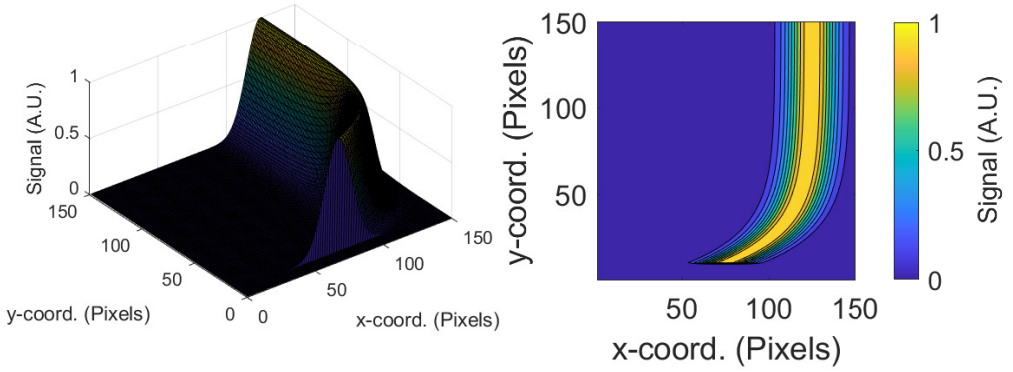

Figure 4.8: Test KTV Fluorescence Signal to Simulate Read KTV image.

and 4.10 show noisy images with SNR decreasing as one goes down the page. In the right-hand-side figures of Figs. 4.9 and 4.10, Fourier Filtered images are presented with varying degree of success.

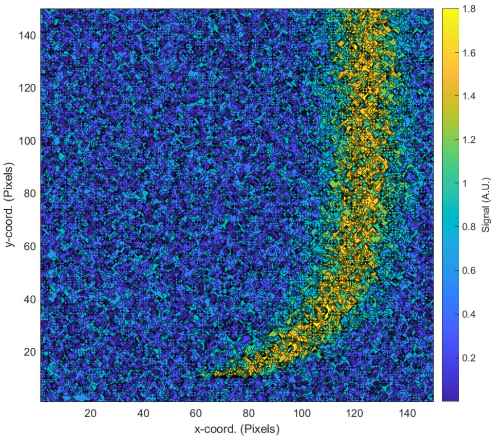

(a) Noisy Image, $\frac{a}{n} = 1.00$, SNR $= 2.17$

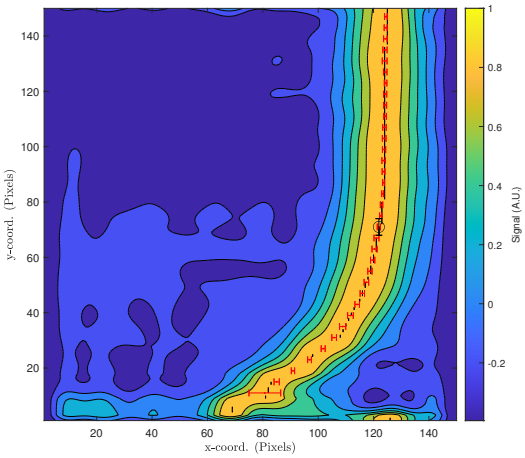

(b) Filtered Image, $\frac{a}{n} = 1.00$, SNR $= 2.17$

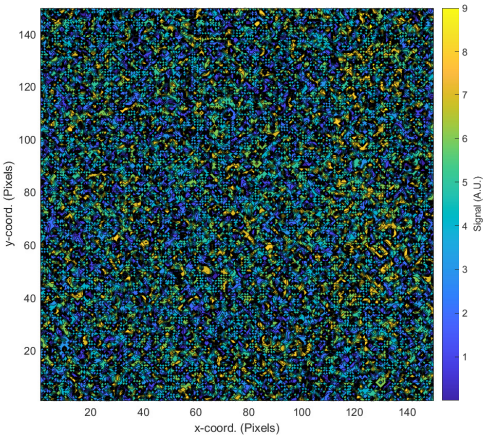

(c) Noisy Image, $\frac{a}{n} = 0.11$, SNR $= 0.16$

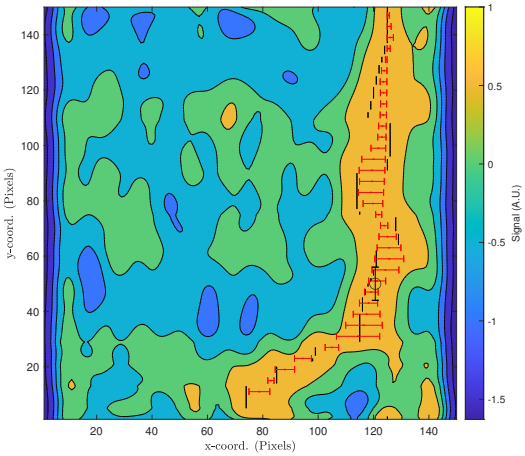

(d) Filtered Image, $\frac{a}{n} = 0.11$, SNR $= 0.16$

Figure 4.9: 2D-Fourier Filtering of Noisy Images with SNR of (a) 2.17 and (c) 0.16.

Fig. 4.11a shows the performance of two-dimensional, lowpass Fourier filtering in recovering features of a simulated, boundary layer read line as a function of signal amplitude to noise amplitude ratio a/n. These features include freestream velocity,

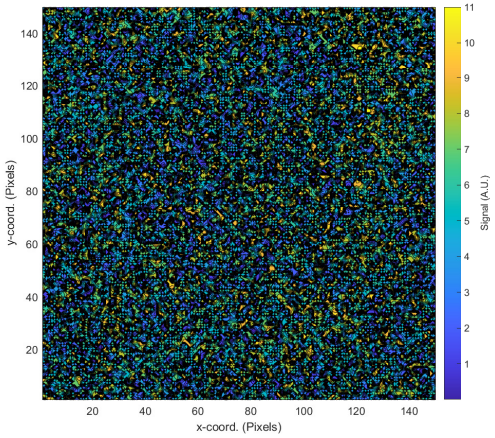

(a) Noisy Image, $\frac{a}{n} = 0.091$, SNR ≈ 0

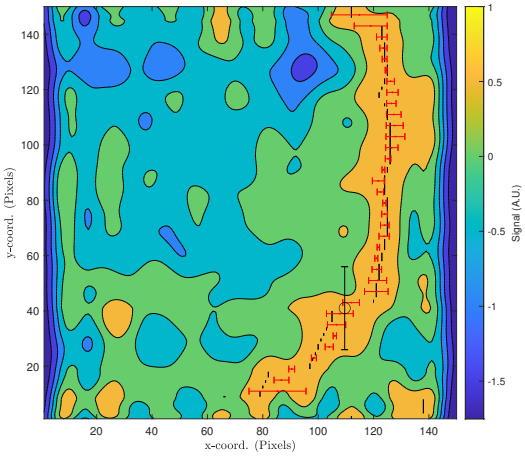

(b) Filtered Image, $\frac{a}{n} = 0.091$, SNR ≈ 0

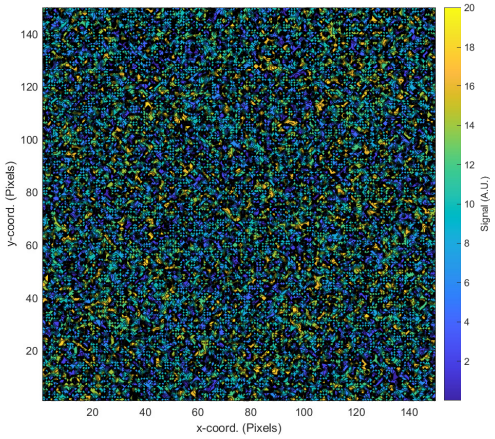

(c) Noisy Image, $\frac{a}{n} = 0.05$, SNR ≈ 0

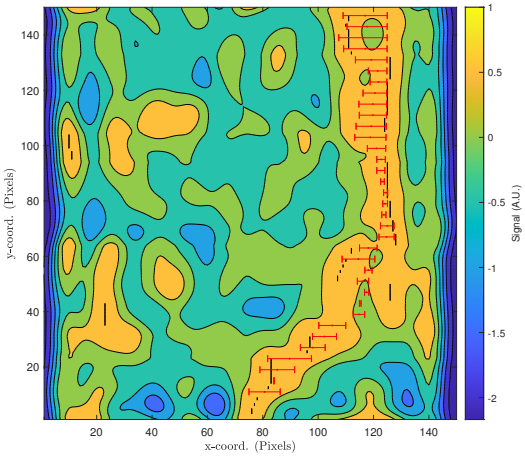

(d) Filtered Image, $\frac{a}{n} = 0.05$, SNR ≈ 0

Figure 4.10: 2D-Fourier Filtering of Noisy Images with low SNR of approximately zero.

wall location, and boundary layer thickness. Deviation of the processed signal from the original signal (Fig. 4.11) increases with respect to decreasing ratio a/n and SNR. Fig. 4.11b shows how SNR varies as a function of amplitude ratio a/n. The minimum a/n required to reliably recover the original signal (Eq. 4.3.1 and Fig. 4.8) is 0.1. Below a/n = 0.1, Fourier-filtering cannot guarantee complete signal recovery, but

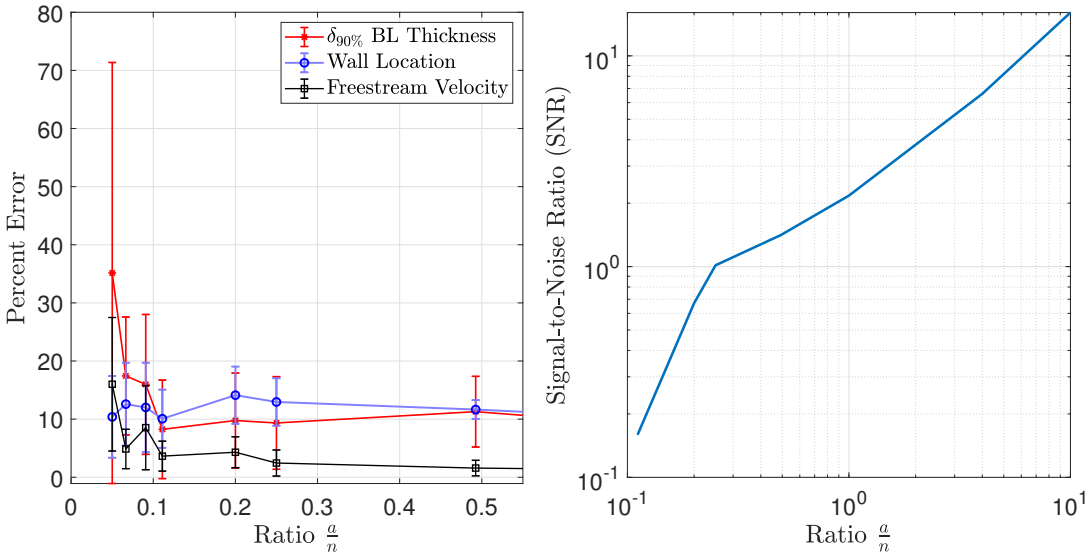

(a) Error in Identifying Features

(b) SNR vs. Ratio a/n

Figure 4.11: Performance of 2DFFT for varying ratio a/n. (a) Flow Features as a function of a/n. (b) SNR as a function of a/n.

it reliably recovers the freestream velocity and wall location. Fig. 4.10 presents the best results for a/n $\leq$ 0.1 out of 10 trials using Eq. 4.3.1. The 90% boundary layer thickness is not accurately processed for a/n $<$ 0.1. Two-dimensional Fourier lowpass filtering is robust against the random noise term for a/n $\geq$ 0.1.

To give further context on the power of 2D-FFT lowpass filtering in the field, the processing of low SNR KTV read images for supersonic flow over a hollow cylinder (using the Ch. 3 KTV experimental setup) is shown in Fig. 4.12. In Fig. 4.12, a discarded shock tube KTV read image is shown in the leftmost image. When processed by the peak finding algorithm of O'Haver [111], peaks are found only 1/3 of the way down the image because the algorithm is thrown off by low SNR in the succeeding rows. To overcome this challenge of low SNR, lowpass Fourier-filtering (with a circular mask) is used to produce the rightmost image. Filtering eliminate features with high wavenumbers (ex. white noise) and smooths the image. When the peak-finding algorithm is applied to the rightmost image, krypton fluorescence signal peaks are

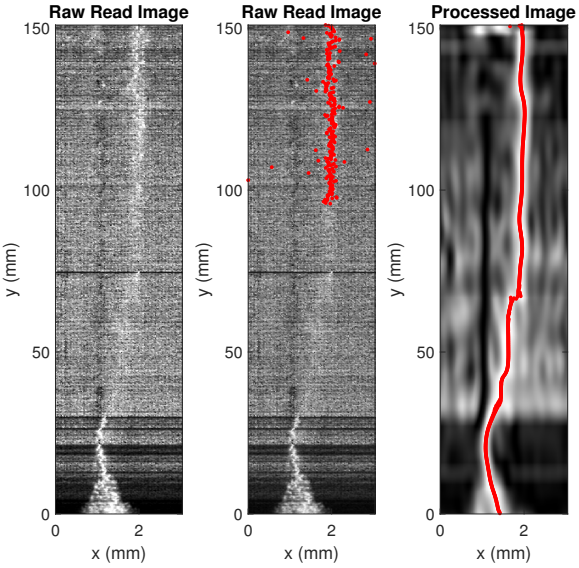

Figure 4.12: KTV over Hollow Cylinder for Shot 43 Stevens Shock Tube in 1% Kr/99% N_2 flow with driven section pressure of $P_1 = 1$ torr and a 3 mJ laser pulse at $\lambda = 212.556$ nm. *Left:* Original Read Image. *Middle:* Image Processed with KTV peak-finding algorithm. *Right:* Lowpass Filtered Image processed by KTV peak-finding algorithm.

located all the way to the wall. Here, lowpass Fourier-filtering was done globally on the entire image, without the need for piecewise application.

4.4 Discussion

The experimental conditions in Mustafa et al. [32] showed that KTV could be performed at static conditions similar to the T5 freestream with 99% N_2/1% Kr, and 75% N_2/20% O_2/5% Kr gas mixtures. Relative to [32] described in Ch. 3, the experiments described in the present work are significantly more complex due to a) the longer standoff distance from the KTV LIF to the camera; b) lower write-laser power, 10 mJ/pulse in [32] versus 3 - 4 mJ/pulse in this work; c) timing complexity; d) laser-power attenuation resulting from not triggering the laser setup at the designed repetition rate of 10 Hz; e) freestream luminosity; and, f) scheduling complications

of single-shot-per-day experiments.

4.4.1 Choice of gas mixtures and quenching effects

In light of the complexity associated with performing experiments in T5, the first experiment was performed with the 97% N_2/3% Kr mixture to serve as a conservative baseline of what could be done with KTV in a large-scale, high-enthalpy reflected-shock tunnel. This successful experiment led to the use of the 99% N_2/1% Kr and 75% N_2/20% O_2/5% Kr gas mixtures in subsequent experiments. The air mixture is doped with 5% Kr, as opposed to the 1% used in the N_2 experiments, because of the additional quenching from O_2. These levels of Kr doping were sufficient in previous experiments [32]. Referring to the energy level diagram in Fig. 2.1c, the increased quenching effects occur in at least two ways: (1) fluorescence quenching of transitions C, D, and F through L, and (2) collisional quenching of the metastable state via $5s[3/2]_2^o \rightarrow 4p^6$. Fluorescence quenching (1) reduces the fluorescence, thus reducing the SNR. Meanwhile, quenching of the metastable state (2) reduces the population of the $5s[3/2]_2^o$ level, which in turn reduces the number Kr atoms to be re-excited with the CW laser diode (transition E in Fig. 2.1c), thus decreasing the SNR by reducing the number of G and F transitions imaged by the camera.

Experiments 2910 and 2926 were conducted approximately one year apart due to the Covid-19 pandemic (Fig. 4.4). All research participants were present for shots 2909 and 2910, but the rest of the experiments were performed by the Caltech researchers with virtual support by the Stevens researchers and myself. Shot 2926 served as a check on the experimental setup and assessed if this experiment could be performed quasi-remotely. The results from Shots 2910 and 2926 are within experimental error of each other, giving some confidence in the repeatability of the measurement and robustness of the technique for other large-scale high enthalpy facilities. One

discrepancy in the results from these two shots is the location of the write-line focus, manifesting itself as a wider write line at 30 mm from the nozzle centerline in shot 2926 than at the same location in shot 2910. In shot 2926, the focus appears to be at the nozzle centerline (approximately 0 mm), and this was corrected to be located at approximately 10 mm in the experiments that followed; the write lines appear more uniform as a result.

At two nominal reservoir enthalpies, ≈5 MJ/kg and ≈8 MJ/kg, two experiments were performed with the 99% N_2/1% Kr mixture and repeated with the 75% N_2/20% O_2/5% Kr mixture.

4.4.2 Effects of flow luminosity

Some non-uniformity was observed in the write line for shot 2910 (Fig. 4.4a), which is unusual for KTV or any tagging experiments; that is, the line should be straight because the flow has not yet had a chance to advect the tagged atoms or molecules. This is speculated to be due to sensor noise exacerbated by high levels of flow luminosity. The flow luminosity in T5 is non-uniform within each experiment in time and space, and is not repeatable from shot to shot at matching conditions. The luminosity could be a function of the tunnel operation during the previous experiment; that is, there could have been material that ablated and was deposited on the shock-tube wall following the run, and then on the following shot, this contaminant would be reintroduced to the test gas and present itself as non-uniform flow luminosity at the instant the write or read image is taken. Parziale et al. [138] noted increased levels of noise during a shot that followed an experiment where a large amount of debris was introduced to the facility via ill-advised tunnel operation. During this campaign, there were no ill-advised experiments where a major amount of contamination would have been introduced to the flow on the following run; however, there is still some

run-to-run variation in flow luminosity likely due to these effects. Finally, shock-tube cleanliness in T5 was the main focus of [139], where boundary-layer transition was noted to be inconsistent if proper shock-tube cleaning procedures were not followed. They were therefore followed in this work.

To assess whether flow luminosity would be an issue at high-enthalpy conditions, two experiments were performed at ≈16 MJ/kg. The first experiment in 99% N_2/1% Kr was successful, but the SNR was low relative to the other 99% N_2/1% experiments at lower-enthalpy conditions. Therefore, the experiment with the 99% N_2/1% Kr mixture was repeated. Noting the write pulse was only 4 mJ/pulse, it is likely that higher write-laser power would increase the SNR to sufficient levels to make measurements in the 75% N_2/20% O_2/5% Kr mixture at the higher-enthalpy conditions.

4.4.3 DPLR/KTV comparison and effects of uncertainty in calculation of run conditions on velocity

The computations from the University of Minnesota Nozzle Code were in excellent agreement with the KTV-measured velocities, being between 0.43 - 3.3% in each of the nine experiments. Comparisons are presented in Table 4.2. The broad range of enthalpy (≈ 5 - 16 MJ/kg) spanned nearly the entire usable envelope of T5 which served as a test of the non-equilibrium thermochemical modeling incorporated into DPLR. That is, if a large modeling error or omission in DPLR was present, a significant error in the calculated velocity would be expected. In the two high enthalpy cases (≈ 16 MJ/kg), KTV measurements of velocity were lower than the DPLR computations. It is speculated that this could be the result of radiation losses in the reservoir, as $T_R > 8000$ K. Quantifying the radiation losses in a reflected-shock tunnel is difficult, as was done in [140]. However, following [141] to a first approximation,

Table 4.2: Comparison of DPLR/KTV Velocimetry Results

Shot	DPLR U_∞ (m/s)	KTV $\overline{U}$ (m/s)	KTV σ (m/s)	% Difference
2909	2983	3056	33.0	0.57
2910	3039	3059	52.3	0.66
2926	2850	2884	27.6	1.2
2927	2836	2848	44.6	0.43
2928	3675	3567	56.0	2.9
2929	3502	3553	55.8	1.5
2930	4894	4797	15.5	2.0
2931	4940	4775	51.3	3.3
2933	3400	3372	26.6	0.82

if a 5% reduction is assumed in reservoir enthalpy, h_R, due to radiation losses, this could explain the 2-3% velocity deficit at the higher enthalpy conditions. This could be an avenue for interesting further work.

As detailed in sec. 4.1.2, the reservoir conditions are calculated using the initial driven section pressure, P_1, the measured incident shock speed U_s, and the measured reservoir pressure, P_R. The reservoir conditions, calculated from these measured parameters, are then input into the UM Nozzle code, giving the freestream conditions. To assess the bounds of error on the inputs to the nozzle code, the error is estimated for P_1, U_s, and P_R as 1.5%, 1.5% and 8% per [142] and [143]. One input was varied at a time. In Table 4.3, only small uncertainties were observed in the freestream velocity due to these measured input uncertainties; for example, the change in freestream velocity due to the uncertainty in the shock speed being is $\widetilde{\Delta U_{\infty U_s}} \approx 1\%$.

Table 4.3: Run-Condition Effect on Calculated Velocity from DPLR.

Shot	$\widetilde{\Delta U_{\infty P_1}}$	$\widetilde{\Delta U_{\infty P_R}}$	$\widetilde{\Delta U_{\infty U_s}}$
2929	0.05%	0.76%	0.98%
2931	0.10%	0.67%	0.85%

4.5 Conclusions

KTV was performed successfully in the T5 Reflected-Shock Tunnel at Caltech. At reservoir enthalpies of 5 MJ/kg and 8 MJ/kg, experiments were performed in 99% N_2/1% Kr and 75% N_2/20% O_2/5% Kr gas mixtures, thus allowing the possibility of performing experiments that investigate non-equilibrium effects. A 16 MJ/kg KTV experiment was performed twice in a 99% N_2/1% Kr gas mixture; with higher laser power, this experiment could likely be repeated in the air/Kr mixture. The experiments at ≈16 MJ/kg had a freestream velocity of ≈4.94 km/s which represent some of the highest experimentally-obtained velocities in the literature.

KTV-measured velocity profiles agree well with computationally obtained velocity profiles, to within the experimental error of the KTV technique. This agreement of experiment and computation in N_2 and air flows over the range of ≈ 5 - 6 MJ/kg brings confidence to the T5 test condition calculation method, which inputs three experimentally-measured quantities: (1) driven section initial pressure, (2) the incident shock-speed, and (3) the reservoir pressure. If there were large systemic errors in this method or omissions in the underlying models in Cantera or the UM Nozzle code, one would expect a larger discrepancy in the freestream velocity or a trend in uncertainty for air vs. N_2 flows due to the great complexity of calculating these reacting flows.

Despite this experimental campaign being interrupted by the Covid-19 pan-

demic shortly after shot 2910, the experimental setup was capable of being operated by tunnel technicians and operators receiving remote instructions and help. The completion of the campaign illustrates the utility, ease, and reliability of the KTV schemes with a pulsed-write laser and CW read laser in performing high speed, high-enthalpy research.

Chapter 5

Preliminary Work Towards Krypton Tagging Velocimetry over a Hollow-Cylinder-Flare Test Article

A hollow-cylinder-flare (HCF) test article, shown in Fig. 5.1, is currently under fabrication for the Stevens Institute of Technology for use in future Krypton Tagging Velocimetry experiments. The HCF is a canonical geometry studied in hypersonic research. Of particular interest is capturing the time-resolved evolution of the separation bubble size at the flare tip and the surface heat-flux profile along the HCF axis, both of which are difficult for CFD codes to predict [5]. Fig. 5.2 shows the geometry and sensor layout of the model. The 34° flare is proposed to create a separation bubble at the flare tip. Schlieren data was obtained for a plastic 36° blockage flare and is presented in this work for Shots 102 and 103. The HCF is instrumented with arrays of PCB 132B38 piezoelectric pressure sensors (0 - 50 psia range at 11 kHz - 1 MHz) along one plane intersecting the cylinder centerline. Twelve degrees offset from this plane lie two arrays of Kulite XCQ-SL-093 sensors, capable of measuring absolute pressure between 0-5, 0-15, and 0-25 psia at 0 - 150 kHz. Along the axis of the pipe are two circular arrays of Kulite XCQ-SL-093 sensors, which will provide information on the lifting moment on the test article.

The test article is designed to be used potentially in the NASA Mach 6 20-inch tunnel in the Langley Research Center (LARC) and in the Mach 6, 24-inch Stevens Shock Tunnel. Work on KTV for the test article is forthcoming. Additionally, the experimental setup will be described for this future KTV campaign.

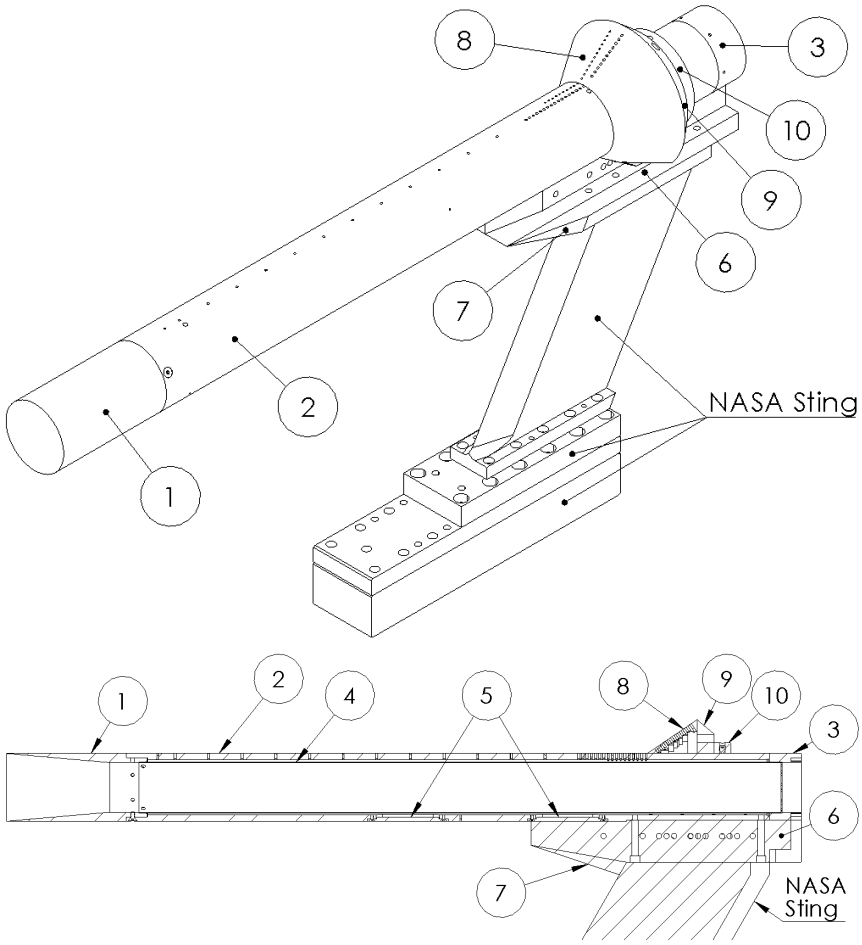

Figure 5.1: Hollow Cylinder Flare. Balloons contain part numbers listed in Table 5.1.

Table 5.1: List of Parts for Hollow Cylinder Flare Assembly shown in Fig. 5.1.

Part	Part Name	Description
1	Removable Hollow Cylinder Tip	Seated Concentrically to Hollow Cylinder Pipe
2	Hollow Cylinder Pipe	Mount onto Adapter Plate
3	Rear Pipe Holder and Wire Router	Mount onto in rear of Hollow Cylinder Pipe
4	Wire Pipe	Inserted btw. Parts 2 and 3 inside Part 1
5	Hatch	Mounted on Bottom of Part 1
6	Adapter Plate	Mounted onto NASA Sting Strut
7	Adapter Wedge Attachment	Mounted onto Adapter Plate
8	34° Flare	Mounted Concentrically on Part 1
9	Flare Rear Plate	Mounted Concentrically to Part 1 behind Part 8
10	Plate Shaft Collar	Mounted Concentrically to Part 1 behind Part 9

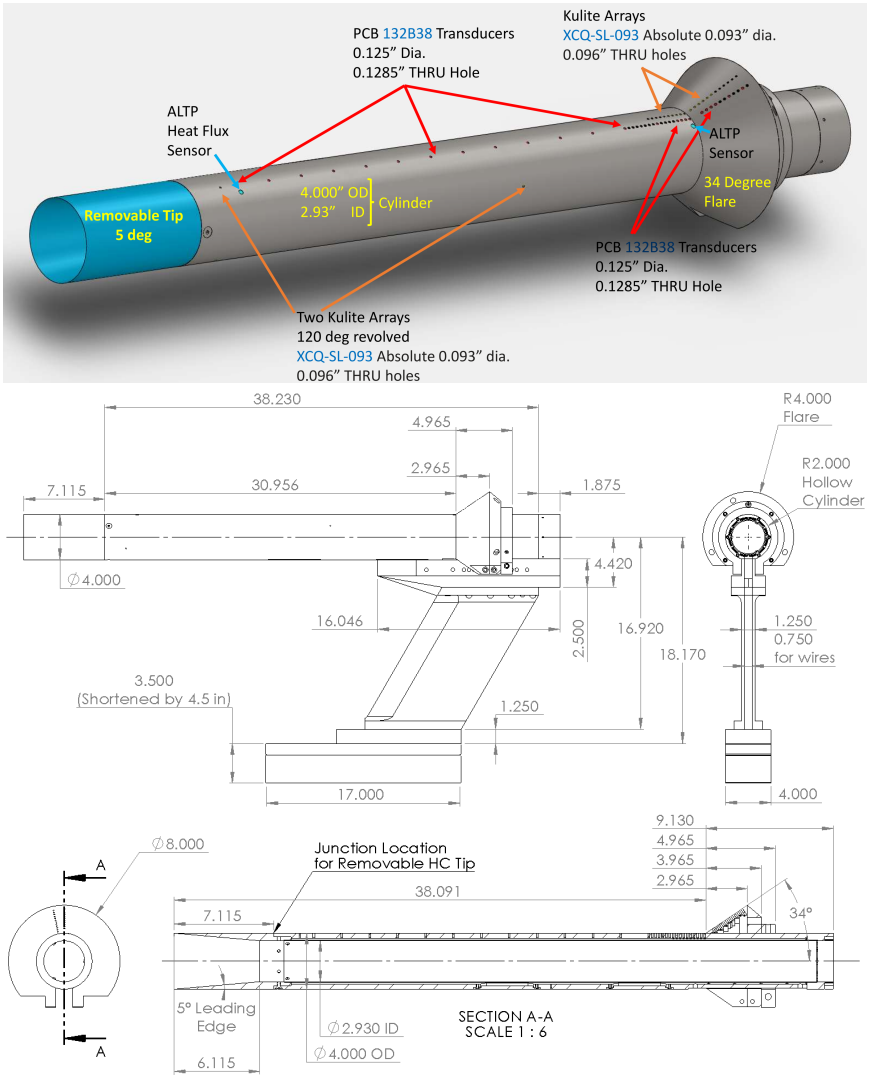

Figure 5.2: Hollow Cylinder Flare Schematics. Balloons correspond to part numbers in Fig. 5.1.

5.1 Schlieren Images of Separation Bubble at Flare Leading Edge in Stevens Shock Tunnel

Schlieren images are presented in Fig. 5.3 for two shots conducted in the Stevens Shock Tunnel with run conditions listed in Table 5.2. These two experiments show a laminar separation bubble at the tip of the flare, indicated by a dark, revolved region at approximately 8.5 degrees with respect to the hollow cylinder axis. Time-resolved

Table 5.2: Run conditions for Selected Shots in Stevens Shock Tunnel. $M_\infty \approx 5.8$ for all shots. Isentropic flow relations are used for determining freestream quantities, denoted by subscript ∞. Shots 102 and 103 were done in shock tunnel configuration.

Shot	P_4 (MPa)	$\frac{P_4}{P_1}$	u_s (m/s)	M_s	P_r (MPa)	T_r (K)	h_r (MJ/kg)	P_∞ (Pa)	T_∞ (K)	Re_∞^{unit} (1/m)
102	3.44	150	1290	3.71	2.55	1875	1.83	1990	243	3.3×10^6
103	1.93	148	1290	3.71	1.44	1872	1.82	1120	242	1.9×10^6

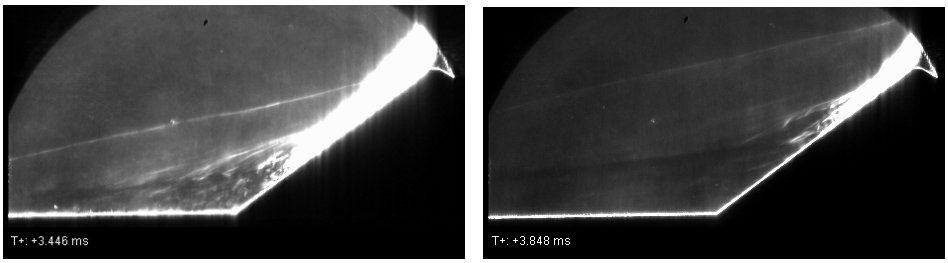

(a) $\theta = 36^\circ$ Shot 102 (b) $\theta = 36^\circ$ Shot 103

Figure 5.3: Schlieren Images of Flow over 36° Hollow Cylinder Flare in the Stevens Shock Tunnel: (a) Shot 102 at $t = 3.448$ ms from rising edge of the nozzle reservoir pressure transducer, (b) Shot 103 at $t = 3.848$ ms from rising edge of nozzle reservoir pressure transducer.

images of a turbulent separation bubble for Stevens Shock Tunnel Shot 106 are found in Fig. 12 of Appendix A in Shekhtman et al. [13]. The dynamics and stability of the flare bubble will be studied in forthcoming experiments.

5.2 Experimental Setup for Hollow Cylinder KTV

The experimental setup for KTV over a HCF is similar to that over a sectioned hollow cylinder, described in Ch. 2 and Mustafa et al. [32] but with two exceptions. The dual-gate Princeton Instruments PIMAX-4 (PM4-1024i-HR-FG-18-P46-CM) camera will be substituted with a high-speed ($f > 100$ kHz) camera with an image intensifier, enabling the capturing of high-speed video, which is necessary for turbulent measurements. The 10 Hz Quanta Ray Pro-350 Nd:YAG laser and a frequency tripled Sirah

PrecisionScan Dye Laser (DCM dye, DMSO solvent) are replaced with a Spectral Energies QuasiModo Pulse-Burst Nd:YAG laser and a Spectral Energies optical parametric oscillator (OPO), as described in Grib et al. [144]. Unlike the work in Ch. 2, the boundary layer near the flare will be considerably thicker, ≈ 7 mm, possibly preventing the laser plume from obscuring the entirety of the boundary layer (especially if Teflon®PTFE is used to protect the test article surface (See Appendix C.)). A 769.45 nm read laser diode is also being considered to excite the resulting metastable Kr state, but a Pockels Cell may be used to pulse the diode output.

The timing of the laser and the camera will be similar to that of the KTV work done in Ch. 4. The rising edge of the reservoir transducer in the Steven Shock Tunnel (Fig. 1.1) will trigger the laser, which will then trigger several multichannel pulse generators that will govern the timing of the camera and the image intensifier.

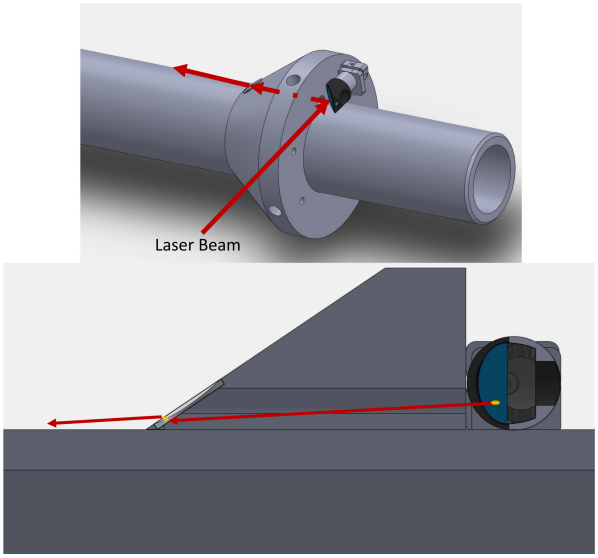

Figure 5.4: Laser Beam Exiting Flare Cavity, Going Across Hollow Cylinder Surface in the Separation Bubble Region.

Additionally, another type of KTV measurement will be made, as shown in Fig. 5.4, in which a laser beam exits out of a cavity in the flare body, going across

the hollow cylinder surface. This laser beam will provide the wall-normal velocity on the Hollow Cylinder and vorticity in the separation bubble region.

5.3 Conclusions

The hollow cylinder flare will help demonstrate new KTV techniques, which will aid in the determination of laminar and turbulent separation bubble physics. The hollow cylinder flare work will make use of a new excitation laser, which in conjunction with a high-speed camera will provide video of turbulent phenomena in the separation bubble region.

Chapter 6
Conclusions

Work was done to further develop Krypton Tagging Velocimetry (KTV) for high-speed, high-enthalpy flow. Theoretical and experimental studies for the optimal krypton excitation line in the 200 - 220 nm range were done. These determined that the 212.556 nm wavelength is optimal for single-laser techniques, and 216.667 nm is optimal for diode-assisted techniques. Additionally, it was determined that in single-laser tagging, the KTV read line signal is dominated by fluorescing $5s$ and $5p$ Kr states, arising from recombination processes and the resulting radiative cascade. When 769.45 nm diode is used in conjunction with single-laser excitation, the Kr metastable state could be excited, regardless of the excitation process. Two benchmark KTV campaigns were conducted in impulse facilities. A KTV study was performed on a hollow cylinder in the Stevens Shock Tube, using a coordinate transformation that magnified the normal boundary layer coordinate and minimized near-wall obstruction. A KTV study was also performed in the freestream of the T5-Reflected Shock Tunnel, demonstrating the capability of KTV in flow with enthalpy 5 - 16 MJ/kg and speed 2840 - 4780 km/s. These extended the pressure and temperature operating ranges of KTV for use in a ground-test facility. This work also used 2D-lowpass Fourier Filtering to process images with low signal-to-noise ratio, demonstrating that low laser energies (3 - 4 MJ/pulse) can be used for KTV at high enthalpy (up to 15.9 MJ/kg) and freestream pressure (4-7.5 kpa).

An upcoming application of KTV will be flow visualization over a hollow cylinder flare (HCF). This entails a study of separation bubble dynamics on the flare's leading edge and the measurement of turbulence quantities (velocity correlations,

pressure fluctuations, and heat-flux profile) along the hollow cylinder. A hollow cylinder flare (HCF) test article was designed to study separation bubble physics and dynamics near the flare. The article design has passed safety design inspection for use in the Mach 6, 20-inch tunnel at NASA LARC and is currently undergoing fabrication. Using the HCF, KTV will be conducted in the Mach 6 Stevens Shock Tunnel.

Appendix A

Hartree-Fock Analysis of Noble Gas Atoms

In this appendix, details are provided on my in-house Hartree-Fock code, which is used to generate the radial wave functions shown in Fig. 2.5 in Ch. 2. Below is an excerpt from my term project for ME-594 numerical methods with the addition of a radial wave function calculation for xenon gas.

The Schrödinger wave equation is the governing equation of atomic physics, a field concerned with atomic processes, such as excitation, emission, and ionization [97]. The Schrödinger equation is a partial differential equation describing the wave nature of a system of particles as a function of system energy, i.e. the Hamiltonian. While the equation is exactly solvable for a hydrogen-like atom with pure Coulombic interaction between a positively charged nucleus and a negatively charged electron, neglecting intrinsic particle spin, the inclusion of electron repulsion in the Hamiltonian of the Schrödinger equation precludes the analytical, mathematical treatment of multielectron atoms. The self-consistent field approach addresses the difficulty of not knowing the relative displacement of two electrons by approximating electron repulsions with a spherically symmetric electric potential [97]. This potential is constructed via the Hartree-Fock method, which calculates the most probable relative displacement of two electrons from guessed electron wave functions that evolve via relaxed fixed-point iteration (a method of sequential substitution). Hence, the Hartree-Fock potential is a first-order approximation of the Coulombic electric potential due to the repulsion between two electrons. The Hartree-Fock method allows for the iterative numerical calculation of orbital energies and radial wave functions for post ab-initio calculations and perturbation theory calculations. The self-consistent field approach

via Hartree-Fock is celebrated for coarse agreement with experiment on the order of 0.1 eV [145] and is fundamental to almost every major quantum mechanical software package that accounts for electron repulsion.

This section develops a numerical code to reliably solve a system of nondimensional radial wave equations describing a multielectron atom. First, the nondimensional form of the radial wave equation is introduced. Then finite difference formulas are used to transform the radial wave equation into a matrix eigenvalue problem. Due to the poor conditioning of eigenvectors in the continuous ionized spectrum of the atom, which prevents direct matrix diagonalization, a spectral shifted inverse power method solver is implemented to solve for the eigenvalue and eigenvector of a specific bound state ($E < 0$). Applying the eigenvalue solver to a system of radial wave functions results in a new set of radial wave functions, which can be resubstituted as a guess back into the system of radial wave ODE's. Repeated re-substitution until convergence of orbital energies is both the essence of both the fixed-point iteration method and the Hartree-Fock method.

A.1 Theory

The general, time independent Schrödinger equation is

$$\hat{H}\Psi = E\Psi, \tag{A.1.1}$$

The Hamiltonian operator $\hat{H}$ acts on the wave function Ψ to obtain the total energy of the system $E = T + V$ in spherical coordinates (r, θ, ϕ), where is θ is the azimuth angle and ϕ is the polar angle [97]. Quantities T and V are kinetic and potential energies, respectively.

A.1.1 The Hydrogen Atom

In this section, a one-electron atom is treated first to provide the necessary background and numerical framework from which the treatment of a multielectron atom can be conveniently formulated. For the hydrogen atom, with the origin placed at the nucleus, the Hamiltonian operator $\hat{H}$ is

$$\hat{H} = -\frac{\hbar^2}{2\mu r}\frac{\partial^2}{\partial r^2}(r(\ )) + \frac{\hat{L}^2}{2\mu r^2} - \frac{Ze^2}{4\pi\epsilon_o r}, \tag{A.1.2}$$

where the first term describes radial kinetic energy; the second term deals with the kinetic energy due to orbital angular momentum; and the third term deals with the Coulombic potential energy of the electron with respect to it distance from the nucleus. Here, $\hbar$ is the reduced Planck Constant; μ is the reduced mass of the electron-nucleus system ($\mu = 1/m_{nucleus} + 1/m_e$), which is approximately the mass of the electron m_e; Z is the atomic number of the atom; $1/(4\pi\epsilon_o)$ is the Coulomb electrostatic constant; e is the charge of one electron; and $\hat{L}^2$ is angular momentum operator, which only acts on angular coordinates. Inserting Eq. A.1.2 in Eq. A.1.1, the Schrödinger equation for a one-electron atom is expressed as

$$-\frac{\hbar^2}{2\mu r}\frac{\partial^2}{\partial r^2}(r\Psi) + \frac{\hat{L}^2\Psi}{2\mu r^2} - \frac{Ze^2}{4\pi\epsilon_o r}\Psi = E\Psi. \tag{A.1.3}$$

Using separation of variables, $\Psi = R(r)Y_l^m(\theta,\phi)$. Therefore,

$$-\frac{\hbar^2}{2\mu r}\frac{\partial^2}{\partial r^2}(rR(r)Y_l^m(\theta,\phi)) + \frac{\hat{L}^2R(r)Y_l^m(\theta,\phi)}{2\mu r^2} - \frac{Ze^2}{4\pi\epsilon_o r}R(r)Y_l^m(\theta,\phi) = ER(r)Y_l^m(\theta,\phi). \tag{A.1.4}$$

Dividing both sides by the spherical harmonic $Y_l^m(\theta,\phi)$ and recognizing that $\hat{L}^2 Y_l^m(\theta,\phi) = \hbar^2 l(l+1) Y_l^m(\theta,\phi)$,

$$-\frac{\hbar^2}{2\mu r}\frac{\partial^2}{\partial r^2}(rR(r)) + \frac{\hbar^2 l(l+1)R(r)}{2\mu r^2} - \frac{Ze^2}{4\pi\epsilon_o r}R(r) = ER(r), \tag{A.1.5}$$

where l is the orbital angular momentum quantum number. Multiplying each side by r gives

$$-\frac{\hbar^2}{2\mu}\frac{\partial^2}{\partial r^2}(rR(r)) + \frac{\hbar^2 l(l+1)rR(r)}{2\mu r^2} - \frac{Ze^2}{4\pi\epsilon_o r}rR(r) = ErR(r). \tag{A.1.6}$$

A substitution, $u(r) = rR(r)$, is made, and the resulting ordinary differential equation is formed:

$$-\frac{\hbar^2}{2\mu}\frac{\partial^2 u}{\partial r^2} + \frac{\hbar^2 l(l+1)u}{2\mu r^2} - \frac{Ze^2}{4\pi\epsilon_o r}u = Eu \tag{A.1.7}$$

with boundary conditions

$$u(r=0) = 0 \tag{A.1.8}$$

$$\lim_{r\to\infty} u(r) = 0. \tag{A.1.9}$$

Eq. A.1.7 is poorly conditioned for a numerical study because the factor $\hbar^2/(2\mu)$ is a small number ($\approx 10^{-33}$ J^{2}s^2/kg). Eq. A.1.7 is nondimensionalized to decrease the roundoff error resulting from the application of finite differences. A dimensionless radial coordinate is introduced $r^* = r/a_o$, where $a_o = \dfrac{4\pi\epsilon\hbar^2}{\mu e^2}$. By multiplying both sides by $\mu a_o^2/\hbar^2$, Eq. A.1.7 is transformed into

$$-\frac{1}{2}\frac{\partial^2 u}{\partial r^{*2}} + \frac{l(l+1)u}{2r^{*2}} - \frac{Ze^2 a_o}{\hbar^2 4\pi\epsilon_o r^*}u = \frac{\mu E a_o^2}{\hbar^2}u. \tag{A.1.10}$$

Dimensionless energy E^* is introduced in units of Hartrees. One Hartree is defined as twice one Rydberg $2Ry = \frac{\hbar^2}{\mu a_o^2}$. Eq. A.1.10 can be simplified into

$$-\frac{1}{2}\frac{\partial^2 u}{\partial r^{*2}} + \left(\frac{l(l+1)}{2r^{*2}} - \frac{Z}{r^*}\right) u = E^* u. \tag{A.1.11}$$

Eq. A.1.11 is in a form suitable for finite differencing. It is the classic nondimensional equation which governs one-electron atoms. The analytical solutions for the radial wave function and energy eigenvalues are

$$\begin{aligned} u = r^* R_n l(r^*) =& r^* \sqrt{\left[\frac{(n-l-1)!}{2n((n+l)!)}\left(\frac{2Z_e}{n}\right)^3\right]}\left(\frac{2Z_e r^*}{n}\right)^l \\ & \times \exp\left(\frac{-Z_e r^*}{n}\right) L_{n-l-1}^{2l+1}\left(\frac{2Z_e r^*}{n}\right), \end{aligned} \tag{A.1.12}$$

and

$$E^* = \frac{-Z^2}{2n^2}, \tag{A.1.13}$$

where n is the principle quantum number and $L_a^b(x)$ is the Laguerre polynomial function.

A.1.2 The Multielectron Atom

When considering a multielectron atom, an additional Coulombic potential energy, the electron repulsion energy, must the considered, namely the Hartree-Fock potential:

$$V_{HF,ij}(r_i) = \left\langle \Psi_i \left| \frac{e^2}{4\pi\epsilon_o r_{ij}} \right| \Psi_j \right\rangle. \tag{A.1.14}$$

The first-order electrostatic potential energy due to any two electrons, i and j, is hence the expected (mean) value, calculated from the wavefunctions of those two electrons. It is nondimensionalized by multiplying it with the factor $\mu a_o^2/\hbar^2$ and

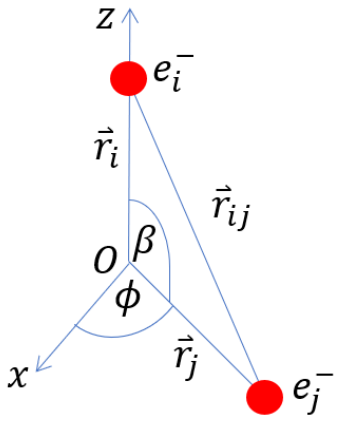

Figure A.1: Electron-Electron Interaction Coordinates.

defining $r = a_o r^*$. This eliminates all constants except the atomic number Z. The nondimensional form of the Hartree-Fock potential is

$$V_{HF,ij}(r_i^*) = \left\langle \Psi_i \left| \frac{1}{r_{ij}^*} \right| \Psi_j \right\rangle . \tag{A.1.15}$$

Using the central-field approximation (self-consistent field approach), the wave function Ψ_i and Ψ_j can be separated into angular and radial parts. Using Fig. A.1 to locate electrons i and j, Eq. A.1.15 can be evaluated as follows:

$$\begin{aligned} V_{HF,ij}(r_i^*) &= \left\langle \Psi_j \left| \frac{1}{r_{ij}^*} \right| \Psi_j \right\rangle \\ &= \int_0^{2\pi} d\phi \int_0^{r_\infty^*} u_j^2 dr_j^* \int_0^{\pi} \frac{\left| Y_{l_j}^{m_j} \right|^2 \sin\beta d\beta}{\sqrt{r_i^{*2} + r_j^{*2} - 2r_i^* r_j^* \cos\beta}}, \end{aligned} \tag{A.1.16}$$

where $u_j = u_j(r_j)$. The assumption of spherical symmetry (s-orbitals; $l_j = 0$; $m_j = 0$) yields

$$\begin{aligned} V_{HF,ij}(r_i^*) &= 2\pi \int_0^{r_\infty^*} u_j^2 dr_j^* \int_0^{\pi} \frac{|Y_0^0|^2 \sin\beta d\beta}{\sqrt{r_i^{*2} + r_j^{*2} - 2r_i^* r_j^* \cos\beta}} \\ &= 2\pi \int_0^{r_\infty^*} u_j^2 dr_j^* \int_0^{\pi} \frac{\left(\frac{1}{4\pi}\right) \sin\beta d\beta}{\sqrt{r_i^{*2} + r_j^{*2} - 2r_i^* r_j^* \cos\beta}} \\ &= \frac{2\pi}{4\pi} \int_0^{r_\infty^*} u_j^2 dr_j^* \int_{-1}^{1} \frac{dx}{\sqrt{r_i^{*2} + r_j^{*2} - 2r_i^* r_j^* x}} \\ &= \frac{1}{2} \int_0^{r_\infty^*} \left[\frac{\sqrt{r_i^{*2} + r_j^{*2} + 2r_i^* r_j^*} - \sqrt{r_i^{*2} + r_j^{*2} - 2r_i^* r_j^*}}{r_i^* r_j^*} \right] u_j^2 dr_j^*, \end{aligned} \tag{A.1.17}$$

which can be evaluated as a single integral. Note that in the third line, the trigonometric substitution $x = \cos(\beta)$ was made.

The Schrödinger equation for a one-electron atom, Eq. A.1.11, is simply appended with the Hartree-Fock potential but is written for each electron i in a multi-electron atom:

$$\begin{aligned} &-\frac{1}{2}\frac{\partial^2 u_i}{\partial r^{*2}} + \left(\frac{l(l+1)}{2r^{*2}} - \frac{Z}{r^*} + \right. \\ &\left. + \frac{1}{2}\Sigma_{j=1}^{Z} \int_0^{r_\infty^*} \left[\frac{\sqrt{r_i^{*2} + r_j^{*2} + 2r_i^* r_j^*} - \sqrt{r_i^{*2} + r_j^{*2} - 2r_i^* r_j^*}}{r_i^* r_j^*} \right] u_j^2 dr_j^* \right) u_i = E_i u_i. \end{aligned} \tag{A.1.18}$$

A multielectron atom consisting of Z electrons will have Z ordinary differential equations, and each electron will have an electron repulsion potential from $Z-1$ electrons.

A.2 Numerical Method

Using second order finite difference formulas to numerical express the second order derivative $\frac{\partial^2 u_i}{\partial r^2}$ in terms of radial spatial index k, Eq. A.1.18 becomes a tridiagonal matrix eigenvalue problem for each electron in an atom:

$$-\frac{u_{i,k-1}}{2(\Delta r^*)^2}-\frac{u_{i,k+1}}{2(\Delta r)^2}+\left(\frac{1}{(\Delta r^*)^2}+\frac{l_i(l_i+1)}{2r_{i,k}^{*2}}-\frac{Z}{r_{i,k}^*}+\right.$$
$$\left.+\frac{\delta}{2}\Sigma_{j=1}^{Z}\int_0^{r_{max}^*}\left[\frac{\sqrt{r_{i,k}^{*2}+r_j^{*2}+2r_{i,k}^*r_j^*}-\sqrt{r_{i,k}^{*2}+r_j^{*2}-2r_{i,k}^*r_j^*}}{r_{i,k}^*r_j^*}\right]u_j^2dr_j^*\right)u_{i,k}=E_iu_{i,k}, \tag{A.2.1}$$

subject to boundary conditions $u_i(r^*=0)=0$ and $\lim_{r^*\to r_{max}^*}u_i(r^*)=0$ with r_{max}^* being a large, finite quantity to approximate infinity. A tweaking parameter, δ, is introduced to match the orbital energy of the valence orbital—ideally, $\delta=1$. The left-hand side of Eq. A.2.1 can interpreted as a tridiagonal matrix A multiplied by an eigenvector $\mathbf{u}_i$:

$$A\mathbf{u}_i=E_i\mathbf{u}_i. \tag{A.2.2}$$

Boundary conditions are applied via the deletions of the first column, first row, last column, and last row of A. This is an extensively used technique in finite element analysis for the implementation boundary conditions in stiffness matrices. This makes the tridiagonal matrix nonsingular with a finite condition number on the order of $\approx 10^5$. Eqs. A.2.1 and A.2.2 are eigenvalue problems easily solved by the spectral-shifted inverse power method, such that the lowest energy value corresponding to a desired bound state ($E<0$) is obtained.

The spectral-shifted inverse power method starts with a guessed eigenvector $\mathbf{u}_i$; spectral shifts matrix A by the reciprocal of a coarse eigenvalue guess $\lambda_c=1/E_{coarse}$:

$$A_{shifted} = A - \frac{1}{\lambda_c} I; \tag{A.2.3}$$

solves for the $(n+1)^{th}$ iteration of $\mathbf{u}_i$ via $A_{shifted}\mathbf{u}_i^{(n+1)} = \mathbf{u}_i^{(n)}$; normalizes $\mathbf{u}_i^{(n+1)}$ by the largest element; and repeats the solution of $\mathbf{u}_i$ via $A_{shifted}\mathbf{u}_i^{(n+1)} = \mathbf{u}_i^{(n)}$ for the next iteration. When the spectral-shifted power method converges on an eigenvector, as dictated by a 2-norm convergence criterion on the difference between the elements $\mathbf{u}_i^{(n+1)}$ and $\mathbf{u}_i^{(n)}$, the normalization factor c_{sol} (the largest element of unnormalized vector $\mathbf{u}_i^{(n+1)}$) is reciprocated and unshifted by spectral shift to obtain the smallest eigenvalue in the vicinity of λ_c:

$$E_i = \lambda_{sol} = \frac{1}{\lambda_c} + \frac{1}{c_{sol}}. \tag{A.2.4}$$

The spectral shift method allows one to target, specific, discrete, bound states ($E < 0$), which have well-conditioned eigenvectors. Unlike matrix diagonalization which results in poorly conditioned eigenvectors due to continuum ionized states ($E \geq 0$), the method readily facilitates high resolution analyses (small $\Delta r \approx 0.005$ Bohr Radii). The eigenvalues are the energies of the orbitals $|nl\rangle$ specified by quantum numbers n and l; and the eigenvector is a discretized eigenfunction. The radial wave function is obtained via the normalization condition

$$\int_0^\infty u_i^2 dr = 1, \tag{A.2.5}$$

which is numerically calculated via trapezoidal integration for each electron ranging between $i = 1, 2, 3, ..., Z$. Meanwhile, Simpson 1/3 composite integration is used to evaluate the Hartree-Fock repulsion energy term in Eq. A.1.18. While the spectral-shifted inverse power method immediately solves Eq. A.1.11 for one-electron atoms,

relaxed fixed-point iteration is necessary to solve the system of Z radial wave function equations contained within Eq. A.1.18. After each iteration, a fraction of the calculated radial wave functions are added to the current set of radial wave functions and are substituted into the Hartree-Fock repulsion integral (Eq. A.1.16). Iteration continues until all system state energies (eigenvalues) converge. The result is an unconditionally stable Hartree-Fock solver. This fixed-point iteration process for Hartree-Fock is outlined in a flow chart in [97].

A.3 Results

The radial wave functions of single hydrogen and noble gas atoms, including He, Ne, Ar, Kr, and Xe were obtained. Results for hydrogen, helium, argon, and krypton are of particular interest.

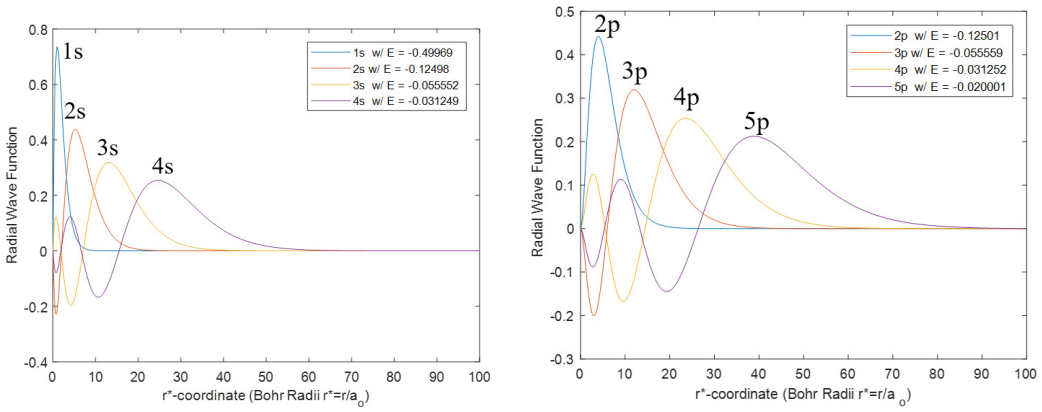

Figure A.2: Hydrogen Radial Wavefunctions. *Left:* Hydrogen s-orbital Radial Wavefunctions. *Right:* Hydrogen p-orbital Radial Wavefunctions.

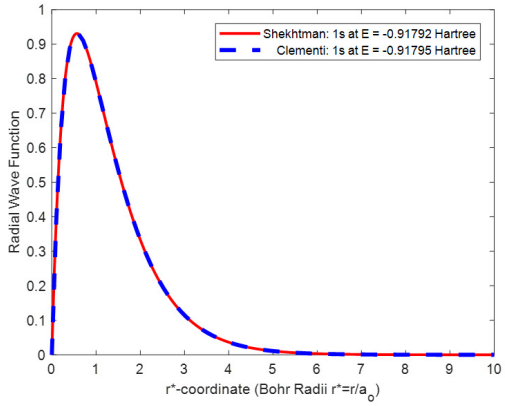

(a) Helium Ground State Radial Wavefunctions.

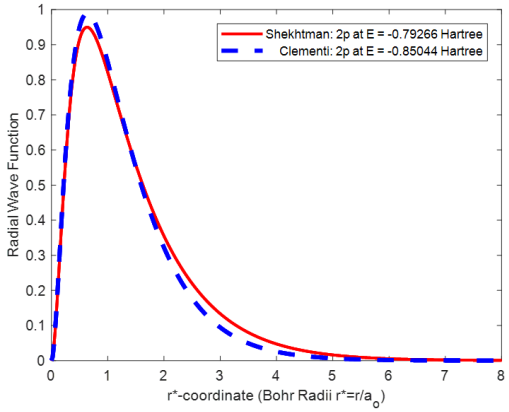

(b) Neon Ground State Radial Wavefunctions.

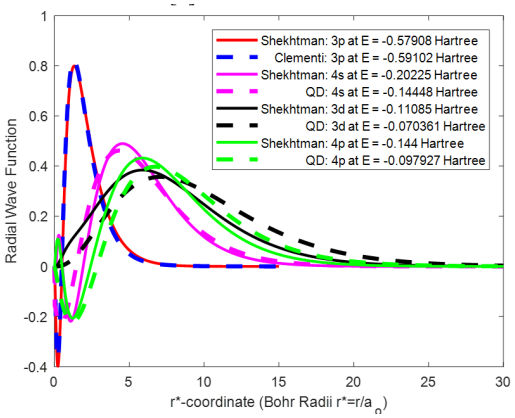

(c) Argon Radial Wavefunctions.

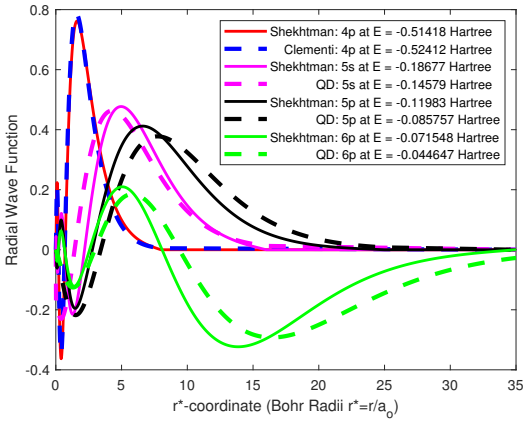

(d) Krypton Radial Wavefunctions.

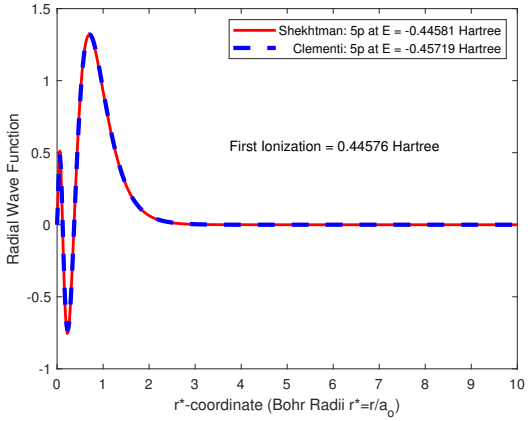

(e) Xenon Ground State Radial Wavefunctions.

Figure A.3: Noble Gas Radial Wavefunctions.

Orbital	Calculated Energy (Hartrees)	Theoretical Energy (Hartrees)	Percent Error
1s	-0.49969	-0.500	0.062%
2s, 2p	-0.12498	-0.125	-0.016%
3s, 3p	-0.055552	-1/18	0.0064%
4s, 4p	-0.031249	-1/32	0.0032%

Table A.1: Orbital Energy Results for Hydrogen Atom

Orbital	Calculated Energy (Hartrees)	Clementi Energy [89] (Hartrees)	Percent Error
1s	-0.91783	-0.91795	0.0131%

Table A.2: Helium Orbital Energy. Note that the experimental orbital energy of the 1s valence electron is -0.9031 Hartree [85].

Orbital	Calculated Energy (Hartrees)	Clementi Energy [89] (Hartrees)	Percent Error
1s	-32.7487	-32.77248	0.00726%
2s	-1.6219	-1.93043	16%
2p	-0.7927	-0.85044	6.79%

Table A.3: Neon Orbital Energies. The experimental orbital energy of the 2p valence electron is -0.7925 Hartree [85].

Orbital	Calculated Energy (Hartrees)	Clementi Energy [89] (Hartrees)	Percent Error
1s	-108.7534	-118.61039	8.31%
2s	-10.8503	-12.32219	11.9%
2p	-9.3455	-9.57150	2.36%
3s	-1.0430	-1.27735	18.3%
3p	-0.5791	-0.59102	2.02%

Table A.4: Argon Orbital Energies. The experimental orbital energy of the 3p valence electron is -0.5792 Hartree [85].

A.4 Discussion

Fig. A.2 validates the use of the spectral shifted inverse power method. Via the method, eigenvalue energies, as shown in table 1, can be accurately calculated with much less restrictive grid sizing ($\Delta r = 0.01 a_o$) than with direct matrix diagonalization

Orbital	Calculated Energy (Hartrees)	Clementi Energy [89] (Hartrees)	Percent Error
1s	-473.5687	-520.16529	8.96%
2s	-64.4556	-69.90320	7.79%
2p	-62.2525	-63.00992	1.20%
3s	-9.1574	-10.84949	15.6%
3p	-7.4806	-8.33152	10.2%
4s	-0.9611	-1.15288	16.6%
3d	-3.4698	-3.82526	9.29%
4p	-0.5142	-0.52412	1.89%

Table A.5: Krypton Orbital Energies. The experimental orbital energy of the 4p valence electron is -0.5145 Hartree [85].

Orbital	Calculated Energy (Hartrees)	Clementi Energy [89] (Hartrees)	Percent Error
1s	-942.5022	-1224.39718	23.0%
2s	-162.1481	-189.34093	14.4%
2p	-179.6035	-177.78252	1.02%
3s	-33.8215	-40.17583	15.8%
3p	-34.5005	-35.22174	2.05%
4s	-6.0260	-7.85620	23.4%
3d	-24.5241	-26.11939	6.11%
4p	-5.5336	-6.00824	7.90%
5s	-0.6734	-0.94433	28.7%
4d	-2.3879	-2.77780	14.0%
5p	-0.4458	-0.45719	2.49%

Table A.6: Xenon Orbital Energies. The experimental orbital energy of the 5p valence electron is -0.4458 Hartree [85].

Tweaking Parameter	He	Ne	Ar	Kr	Xe
δ	1	0.980	0.9774	0.9881	0.989681

Table A.7: Tweaking Parameters for Hartree-Fock Repulsion Potential to compensate for discretization, truncation, and round-off error. The parameter δ should equal 1 for the theoretical realization of the s-orbital Hartree-Fock potential, Eq. A.1.16.

of Eq. A.2.1 and A.2.2. Atoms beyond helium presented the complication of p-orbital electrons. However, under the Hartree-Fock assumption, all orbitals can be

treated as spherically symmetric s-orbitals. This results in energy eigenvalues with a maximum relative error of 16% with Clementi's ground state energies for Neon. Errors in orbital energies are of similar magnitude for argon and krypton. The same is not true for xenon, which is better described by a relativistic quantum formulation: the Dirac equation. Regardless, in order to improve the utility of the wavefunctions, the energies of the valence orbitals were matched with the first ionization energy [85] of each gas (Ne, Ar, Kr, and Xe), using a tweaking parameter δ for the Hartree-Fock potential term in Eq. A.2.1, as detailed in Table A.7. Since δ is close to one, at most within 3.26%, the Hartree-Fock assumption s-orbitals is good for calculating the radial wavefunctions of valence orbitals [145]. The tweaking parameter compensated for discretization, truncation, and round off error. Domain sizes for radius were chosen based on the premise that a wavefunction must decay to zero. With increasing atomic number Z, the maximum radial coordinate can be reduced.

Results for both Ar and Kr showed that (1) a frozen core is a poor assumption for excited electronic states (ex. 6p state of Kr in Fig. A.3d); and (2) the quantum defect approximation (Eq. 2.1.27) is a reasonable and computationally cheap approximation for excited electronic states. One cannot assume that for excited states, core electrons remain at ground state—the frozen core assumption for noble gas excited states is invalid. Figs. A.3c and A.3d are proof that an excited noble gas atom exhibits scaled hydrogenic behavior. Hence, quantum defect wave functions were used in analyses involving excited noble gas states, such as perturbation theory and ab initio calculations.

A.5 Conclusions

The Hartree-Fock Method was successfully implemented via an unconditionally stable, relaxed fixed-point iteration, spectral-shifted inverse power method solver. The solver featured less restrictive grid sizing $\Delta r = 0.01 a_o$ than direct matrix diagonalization via the QR method, for hydrogen and noble gases from helium to krypton. The solver can achieve high resolution for eigenvectors. While this work did not take advantage of the tridiagonal matrix properties to increase computation speed of the spectral shifted inverse power method, this can be done in the future. The solver produced two useful quantum mechanical results. The frozen core model for excited states was invalidated, and quantum defect radial wavefunctions were validated for Kr and Ar, as shown in figs. 5 and 6. This paper is a potential launching point for perturbation calculations, ab initio calculations, and more complex Hartree-Fock analyses, that can involve electron exchange energy and time dependency, such as those described in [101, 145].

Appendix B

Calculation of Weighting Parameter $1.w_t$

The probability of a dipole transition occurring between two degenerate states in an isotropic electric field is $1/w_t$. Thus, the weight on a single dipole moment is $1/\sqrt{w_t}$ because the probability rate of a dipole transition is proportional to the square of the dipole moment. This section also showcases the symmetry of the 3j-Wigner symbol (the Clebsch-Gordan coefficient) due to the even parity of the sum, $J_i + 1 + J_j$, which represents the sum of the first row. This further cements the symmetry of the dipole matrix D. Matrix D is indeed a rank 2 tensor.

Case 1a: Transitions with $l_j = 0$ to $l_i = 1$

$$\begin{pmatrix} 1 & 1 & 0 \\ 0 & 0 & 0 \end{pmatrix} = -\frac{1}{\sqrt{3}} \quad \begin{pmatrix} 1 & 1 & 0 \\ -1 & 1 & 0 \end{pmatrix} = \frac{1}{\sqrt{3}} \quad \begin{pmatrix} 1 & 1 & 0 \\ 1 & -1 & 0 \end{pmatrix} = \frac{1}{\sqrt{3}} \tag{B.0.1}$$

In this case, there are three possible transitions: $w_t = 3$. The 2-norm is 1.

Case 1b: Transitions with $l_j = 1$ to $l_i = 0$

$$\begin{pmatrix} 0 & 1 & 1 \\ 0 & 0 & 0 \end{pmatrix} = -\frac{1}{\sqrt{3}} \quad \begin{pmatrix} 0 & 1 & 1 \\ 0 & 1 & -1 \end{pmatrix} = \frac{1}{\sqrt{3}} \quad \begin{pmatrix} 0 & 1 & 1 \\ 0 & -1 & 1 \end{pmatrix} = \frac{1}{\sqrt{3}} \tag{B.0.2}$$

This case also has three possible transitions: $w_t = 3$. The 2-norm is 1.

Case 2a: Transitions with $l_j = 1$ to $l_i = 2$

$$\begin{pmatrix} 2 & 1 & 1 \\ 0 & 0 & 0 \end{pmatrix} = \sqrt{\frac{2}{15}} \qquad \begin{pmatrix} 2 & 1 & 1 \\ 0 & 1 & -1 \end{pmatrix} = \frac{1}{\sqrt{30}} \qquad \begin{pmatrix} 2 & 1 & 1 \\ 0 & -1 & 1 \end{pmatrix} = \frac{1}{\sqrt{30}}$$

$$\begin{pmatrix} 2 & 1 & 1 \\ -1 & 1 & 0 \end{pmatrix} = -\frac{1}{\sqrt{10}} \quad \begin{pmatrix} 2 & 1 & 1 \\ -1 & 0 & 1 \end{pmatrix} = -\frac{1}{\sqrt{10}} \quad \begin{pmatrix} 2 & 1 & 1 \\ 1 & -1 & 0 \end{pmatrix} = -\frac{1}{\sqrt{10}}$$

$$\begin{pmatrix} 2 & 1 & 1 \\ 1 & 0 & -1 \end{pmatrix} = -\frac{1}{\sqrt{10}} \qquad \begin{pmatrix} 2 & 1 & 1 \\ -2 & 1 & 1 \end{pmatrix} = \frac{1}{\sqrt{5}} \qquad \begin{pmatrix} 2 & 1 & 1 \\ 2 & -1 & -1 \end{pmatrix} = \frac{1}{\sqrt{5}} \tag{B.0.3}$$

This case has nine possible transitions: $w_t = 9$. The 2-norm is 1.

Case 2b: Transitions with $l_j = 2$ to $l_i = 1$

$$\begin{pmatrix} 1 & 1 & 2 \\ 0 & 0 & 0 \end{pmatrix} = \sqrt{\frac{2}{15}} \qquad \begin{pmatrix} 1 & 1 & 2 \\ -1 & 1 & 0 \end{pmatrix} = \frac{1}{\sqrt{30}} \qquad \begin{pmatrix} 1 & 1 & 2 \\ 1 & -1 & 0 \end{pmatrix} = \frac{1}{\sqrt{30}}$$

$$\begin{pmatrix} 1 & 1 & 2 \\ 0 & 1 & -1 \end{pmatrix} = -\frac{1}{\sqrt{10}} \quad \begin{pmatrix} 1 & 1 & 2 \\ 0 & -1 & 1 \end{pmatrix} = -\frac{1}{\sqrt{10}} \quad \begin{pmatrix} 1 & 1 & 2 \\ 1 & 0 & -1 \end{pmatrix} = -\frac{1}{\sqrt{10}}$$

$$\begin{pmatrix} 1 & 1 & 2 \\ -1 & 0 & 1 \end{pmatrix} = -\frac{1}{\sqrt{10}} \qquad \begin{pmatrix} 1 & 1 & 2 \\ 1 & 1 & -2 \end{pmatrix} = \frac{1}{\sqrt{5}} \qquad \begin{pmatrix} 1 & 1 & 2 \\ -1 & -1 & 2 \end{pmatrix} = \frac{1}{\sqrt{5}} \tag{B.0.4}$$

This case also has nine possible transitions: $w_t = 9$. The 2-norm is 1.

Appendix C

Laser Wall Ablation Plume Prohibiting Near-Wall KTV

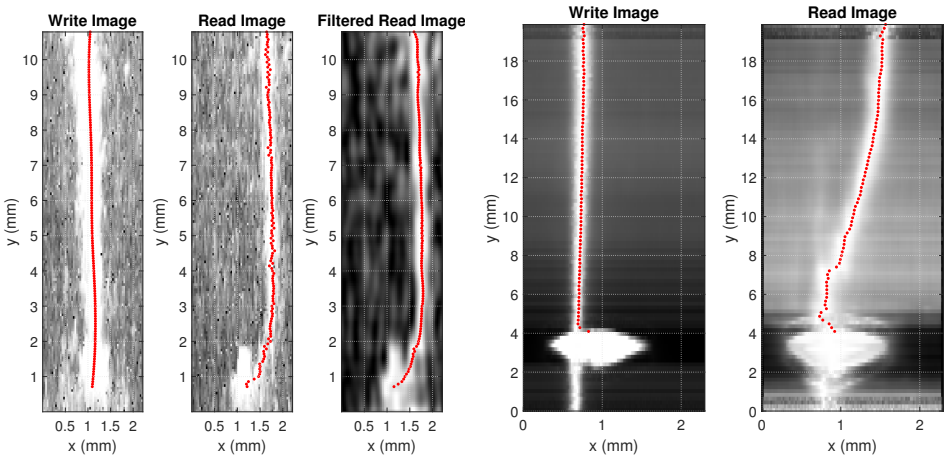

(a) Shot 77: Flat Plate (b) Shot 94: Hollow Cylinder

Figure C.1: Laser Ablation Plumes (a) over a Fused Silica Window mounted on a Sharp Flat Plate in the Stevens Shock Tube with laser pulse energy of 5 mJ, camera delay $\Delta t = 1\ \mu s$, driven section pressure of $P_1 = 3$ torr 99% N_2 1% Kr, and $P_4 = 1$ atm air driver; and (b) over a PVC Hollow Cylinder Pipe in the Stevens Shock Tube (see Ch. 4 Fig. 3.1) with laser pulse energy of 9 mJ, camera delay $\Delta t = 0.660\ \mu s$, driven section pressure of $P_1 = 2$ torr, and $P_4 = 1$ atm helium driver. The filtered image is a low-pass 2D-FFT filtered image.

Insufficient near-wall signal can prevent a study of boundary layers via KTV, so mitigating the effects of the plume is essential. When a 7 ns, 212.556 nm laser beam interacts with a wall interface, thermal heating and multiphoton ionization occur. In Fig. C.1a, laser ablation occurs on a flat plate from a 212.556 nm, 5 mJ, 7 ns beam (normal to the surface), forming a 0.5 mm $\times$ 2 mm plume. In Fig. C.1b, laser ablation occurs on a hollow cylinder from a 212.556 nm, 9 mJ, 7 ns beam (tangential to the surface), forming a 1 mm $\times$ 2 mm plume that obscures the boundary layer. A heat-transfer model is described below to show that commercially-available opaque

materials will vaporize and ionize within nanosecond timescales at an intensity on the order of 10^{11} W/cm^2. In KTV, a laser beam is focused some distance above a test article in order to obtain flow profiles parallel with the wall. During the KTV read step, fluorescence is mostly generated by electron-ion recombination processes and cascade decay. In Fig. C.2, normalized read-step KTV signal, which is approximately proportional to the number density of ionized Kr, is obtained via a closed-form population model for (2+1) REMPI described in Saito et. al [87], using the calculated excitation cross-sections from Ch. 2:

$$\frac{n_e(t)}{n_{Kr,o}} = \frac{ab}{\alpha_1 - \alpha_2}\left[\frac{1}{\alpha_1}(e^{\alpha_1 t} - 1) - \frac{1}{\alpha_2}(e^{\alpha_2 t} - 1)\right], \tag{C.0.1}$$

where $a = \sigma^{(2)}F^2$, $b = \sigma_i F$, $\alpha_{1,2} = -\frac{(a+b)}{2} \pm \sqrt{\frac{(a+b)^2}{4} - ab}$, and $F = \frac{I_o}{\hbar\omega}$ is the photon flux. The two-photon excitation cross-section is $\sigma^{(2)}$; the one-photon ionization cross-section is σ_i; the laser intensity is I_o; the laser angular frequency is ω; $n_e(t)$ is the number density of electrons (or Kr ions); and $n_{Kr,o}$ is the initial number density of ground-state Kr, prior to excitation. This normalized signal is plotted as a function of distance from the focus f_o of a lens and laser intensity.

The beam of the laser is assumed to be Gaussian with a intensity distribution of $I(x,r) = I(x)\exp(-\frac{2r^2}{R_o^2})$, where the beam waist $r^2(x) = R_o^2\left(1 + \left(\frac{\lambda_L x}{\pi R_o^2}\right)^2\right)$. Given a focal length f_o and output laser beam waist r_{beam}, the beam waist at the lens focus R_o is determined by solving $r_{beam}^2 = R_o^2\left(1 + \left(\frac{\lambda_L f_o}{\pi R_o^2}\right)^2\right)$ for R_o [146]:

$$\begin{aligned} R_o &= \sqrt{\frac{\pi^2 r_{beam}^2 - \sqrt{\pi^2 r_{beam}^4 - 4\lambda_L^2 f_o^2 \pi^2}}{2\pi^2}} \\ &\approx \frac{\lambda_L f_o}{\pi r_{beam}}. \end{aligned} \tag{C.0.2}$$

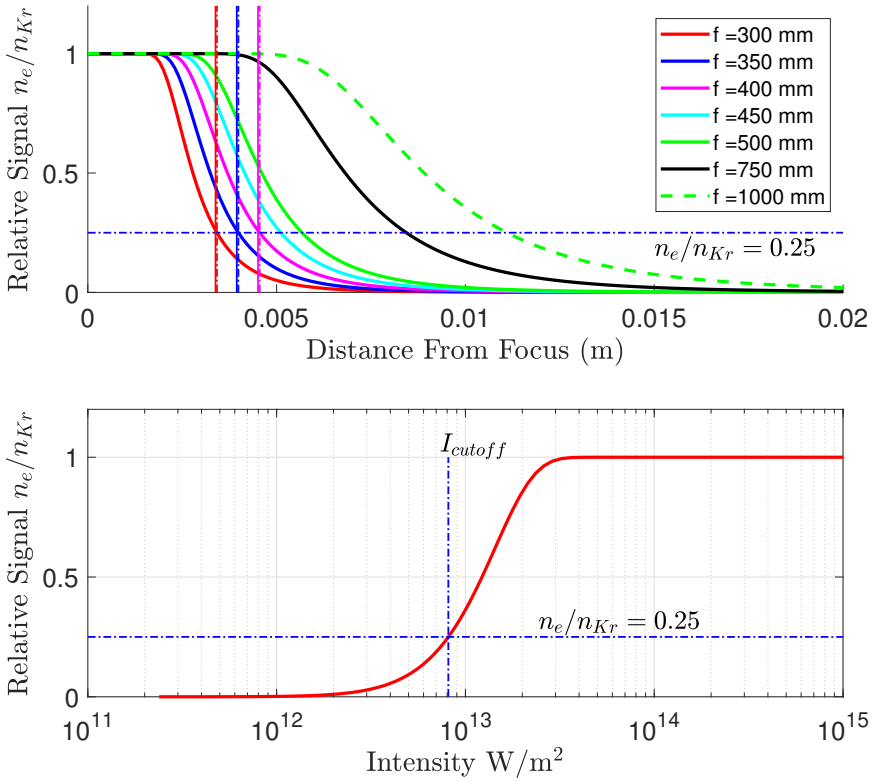

Figure C.2: KTV Fluorescence Signal Parameter Space.

Given an energy E_o per laser pulse, the intensity may be calculated along the laser beam as $I(x) = E_o/(\pi r(x)^2)$. Using the cuttoff intensity I_{cut} for KTV signal from Fig. C.2 and given E_o and laser pulse width τ, the maximum allowable beam waist is $r_{max} = \sqrt{\frac{E_o}{\pi I_{cut}\tau}}$. Thus, the desired location of the test article wall becomes

$$x_{\text{wall}} = \sqrt{\frac{\pi^4 R_o^4}{\lambda_L^2}\left[\left(\frac{r_{max}}{R_o}\right) - 1\right]}. \tag{C.0.3}$$

In the upper plot of Fig. C.2, solid vertical lines denote signal cuttoff wall locations, relative to the lens focus. Dashed lines denote desired wall locations relative to the lens focus, for AF2400 Teflon®at 0.5 J/cm^2. Foci for considered lenses were greater than 300 mm to be able to probe at least 292 mm (11.5 in) into the 610 mm (24 in) diameter test section of the Stevens Shock Tunnel.

C.1 Thermal Modeling

The significance of thermal ablation of a substrate due to laser heating can be determined by solving the 1-D semi-infinite, half-space heat-transfer equation,

$$\frac{\partial T}{\partial t} = D\frac{\partial^2 T}{\partial z^2} + \frac{I_o \alpha (1-R) e^{-\alpha z}}{\rho C}. \tag{C.1.1}$$

Here, T is the temperature of the substrate; $D = k/(\rho C)$ is the thermal diffusivity; k is the bulk thermal conductivity; ρ is the bulk density; C is the bulk specific heat; z is the depth from the surface where the laser beam first makes contact; I_o is the laser intensity; α is the absorptivity of the material (Beer's law); and R is the reflectance of the substrate surface. Laser heating results in volumetric heating for optically penetrating substrates, and as will be proved later, surface heating for opaque substrates. Analytical insight can be gained via application of the Laplace transform on Eq. C.1.1:

$$s\mathcal{T} - D\frac{\partial^2}{\partial z^2}(\mathcal{T}) = T_o + \frac{I_o \alpha (1-R) e^{-\alpha z}}{\rho C s}, \tag{C.1.2}$$

where $\mathcal{L}\{T\} = \mathcal{T}$ is the Laplace transformed temperature. The general solution of Eq. C.1.2 is

$$\mathcal{T} = \frac{T_o}{s} + C_1 \exp\left(-z\sqrt{\frac{s}{D}}\right) + \frac{I_o(1-R)e^{-\alpha z}}{k\alpha}\left[\frac{1}{s - D\alpha^2} - \frac{1}{s}\right]. \tag{C.1.3}$$

If an adiabatic condition is assumed on the surface ($\frac{\partial T}{\partial z} = 0$), then

$$C_1 = \frac{I_o(1-R)\sqrt{D}}{k\sqrt{s}}\left[\frac{1}{s} - \frac{1}{s - D\alpha^2}\right], \tag{C.1.4}$$

and thus,

$$\mathcal{T} = \frac{T_o}{s} + \frac{I_o(1-R)}{k}\left[\frac{\sqrt{D}\exp\left(-z\sqrt{\frac{s}{D}}\right)}{s\sqrt{s}} - \frac{\sqrt{D}\exp\left(-z\sqrt{\frac{s}{D}}\right)}{(s-D\alpha^2)\sqrt{s}} + \frac{e^{-\alpha z}}{\alpha}\left[\frac{1}{s-D\alpha^2} - \frac{1}{s}\right]\right]. \tag{C.1.5}$$

$$= \frac{T_o}{s} + \frac{I_o(1-R)}{k}\left[-\frac{D\alpha^2\sqrt{D}\exp\left(-z\sqrt{\frac{s}{D}}\right)}{s\sqrt{s}(s-D\alpha^2)} + \frac{e^{-\alpha z}}{\alpha}\left[\frac{1}{s-D\alpha^2} - \frac{1}{s}\right]\right], \tag{C.1.6}$$

noting that $\frac{\sqrt{D}\exp\left(-z\sqrt{\frac{s}{D}}\right)}{(s-D\alpha^2)\sqrt{s}} = \frac{\sqrt{D}\exp\left(-z\sqrt{\frac{s}{D}}\right)}{s\sqrt{s}}\left(\frac{s}{s-D\alpha^2}\right) = \frac{\sqrt{D}\exp\left(-z\sqrt{\frac{s}{D}}\right)}{s\sqrt{s}}\left[1-\frac{D\alpha^2}{s-D\alpha^2}\right]$. Eq. C.1.6 describes solutions pertaining to optically opaque (large α), translucent (finite α), and transmissive surfaces (low α). It is very simple to apply limits to α in the Laplace Domain, but it is more interesting to apply them in the time domain to check the validity of the analytical solution. In many works, the analytical solution for the thermal-heating of an optically-penetrating substrate is written as the inverse transform of Eq. C.1.5

$$\begin{aligned} T(z,t) =& T_o + \frac{I_o(1-R)}{k}\left\{2\sqrt{Dt}\,\text{ierfc}\left(\frac{z}{2\sqrt{Dt}}\right) - \frac{1}{\alpha}e^{-\alpha z}\right. \\ &\left. + \frac{e^{\alpha^2 Dt}}{2\alpha}\left[e^{\alpha z}\text{erfc}\left(\alpha\sqrt{Dt} + \frac{z}{\sqrt{Dt}}\right) + e^{-\alpha z}\text{erfc}\left(\alpha\sqrt{Dt} - \frac{z}{\sqrt{Dt}}\right)\right]\right\}, \end{aligned} \tag{C.1.7}$$

but while mathematically correct,[1] this equation is unusable—it is numerically insensitive to low absorptivity ($\mathcal{O}(0)$ 1/m) and unstable for high absorptivity ($\mathcal{O}(9)$ 1/m). MATLAB is unable to evaluate the limits of Eq. C.1.7 for $\alpha \to 0$. For example, direct numerical evaluation for $\alpha = 0$ would yield $T_o + \frac{2I_o(1-R)}{k}\sqrt{Dt}\text{ierf}\left(\frac{z}{2\sqrt{Dt}}\right)$, but analytical calculus correctly yields T_o. Meanwhile, Eq. C.1.6 explicitly conducts the

[1] The author has also derived this equation using a table of Laplace transforms listed in [147].

subtraction of the surface heating term (first term) with optical contributions, resulting in a more numerically stable solution (the only minus being the need to evaluate a convolution integral.). Applying the inverse Laplace transform on Eq. C.1.6 and using table of Laplace Transforms listed in Zill et al. [147], the solution becomes

$$T(z,t) = T_o + \frac{I_o(1-R)}{k}\left[2\sqrt{D}\int_0^t D\alpha^2\sqrt{\tau}\,\text{ierfc}\left(\frac{z}{2\sqrt{D\tau}}\right)e^{D\alpha^2(t-\tau)}d\tau + -\frac{e^{-\alpha z}}{\alpha}\left[1-e^{D\alpha^2 t}\right]\right], \tag{C.1.8}$$

where a convolution integral arises in the second term and $\text{ierfc}(x)$ is the integral of the complementary error function: $\text{ierfc}(x) = e^{-x^2}/\sqrt{\pi} - x\text{erfc}(x)$. For a completely transmissive substrate with $\alpha \to 0$, $T(z,t) = T_o$, implying no laser heating occurs. For completely opaque substrate with $\alpha \to \infty$,

$$\begin{aligned} T(z,t) &= T_o + \frac{I_o(1-R)}{k}\left[2\sqrt{D}\int_0^t \sqrt{\tau}\,\text{ierfc}\left(\frac{z}{2\sqrt{D\tau}}\right)\delta(t-\tau)d\tau\right] \\ &= T_o + \frac{2I_o(1-R)}{k}\sqrt{Dt}\;\text{ierfc}\left(\frac{z}{2\sqrt{Dt}}\right), \end{aligned} \tag{C.1.9}$$

which translates into the case of an incident heat flux $I_o(1-R)$ heating the surface of the substrate. In order to extract the limiting response of surface heat flux, the definition of a nascent Delta Dirac function was used [148, Appendix C]:

$$\lim_{\epsilon\to 0}\frac{1}{\epsilon}\eta_\epsilon(t-\tau) = \lim_{\alpha\to\infty}\frac{1}{\left(\frac{1}{-D\alpha^2}\right)}\exp\left(\frac{-(t-\tau)}{\left(\frac{-1}{D\alpha^2}\right)}\right) \approx \delta(t-\tau). \tag{C.1.10}$$

Eq. C.1.8 is superior to the analytical solution published in Bechtel [149] and Sands [150][2] because it is more numerically stable in the limit of low absorptivity α. From

[2]Note that Sands [150] has a typo in his equations, consisting of an extra factor of α in the factor $2\alpha I_o(1-R)/k$. This factor of α must be removed in equations 14, 17, 18, and 19 to make them dimensionally correct. Otherwise, the review by Sands [150] is comprehensive and informative.

Table C.1: Table of Material Properties for Candidate Materials. Sources include Matweb [151] for densities, specific heats, and thermal conductivities. For optical materials, Cystran Optics [152] was used.

Material	ρ kg/m^3	C J/(kg·K)	k W/(m·K)	R	α 1/m	Φ W·s/m^2·K
PTFE	2172	1000	0.27	0.60 [153]	15800 [154]	1.1×10^2
FEP Teflon®	2172	1000	0.27	0.60 [155, 156]	8300 [156]	4.1×10^2
AF2400 Teflon®	1700 [157]	1000	0.05 [157]	0.10 [158]	260 [158]	3.1×10^5
ETFE Teflon®	1700 [159]	1900 [159]	0.238 [159]	0.085 [159]	1500 [160]	5.6×10^3
Gold	19320	129	314	0.27	8.0×10^7	4.8×10^{-8}
Aluminum	2700	900	205	0.5 [161]	1.5×10^8	2.3×10^{-8}
Copper	8930	400	360	0.35 [161]	7.4×10^7	9.9×10^{-8}
Molybdenum	10200	250	138	0.66	6.4×10^7	2.5×10^{-7}
4000 Steel	7874	460.5	50.2	0.4 [161]	1.0×10^9	1.6×10^{-9}
Fused Silica	2700	840	1.38	0.07	1.0×10^{-4}	3.1×10^{17}
MgF_2	3177	1003	33.6	0.057	4.0	6.5×10^7
CaF_2	3180	854	9.71	0.054	0.078	2.5×10^{11}

Eq. C.1.8, a performance parameter is identified,

$$\Phi = \frac{\sqrt{\rho C k}}{\alpha^2 D(1-R)} = \frac{(\rho C)^{1.5}}{\alpha^2 (1-R)\sqrt{k}} \tag{C.1.11}$$

to determine via maximization which substrate materials are optimal for the mitigation of thermal laser ablation, as shown in Table C.1.

From the table, it is obvious that fused-silica glass is the optimal material to avoid thermal laser ablation. However, it is (1) not feasible to construct a hypersonic test article from glass, and (2) there are other ionization mechanisms, such as multi-photon ionization, which preclude glass (low laser damage threshold of 3.2 J/cm^2 at 212.556 nm and pulsewidth 7 ns[162]). Structural strength of test articles in shock tunnels and impulse facilities requires the use of more robust materials, such as steel and aluminum. However, from Eq. C.1.9, the surface temperature of an opaque ma-

terial at the end of a laser pulse is

$$T(z=0,t=\tau) = To + \frac{2I_o(1-R)}{k\sqrt{\pi}}\sqrt{Dt}, \tag{C.1.12}$$

and thus, for laser pulse-width of $\tau = 7$ ns with an average intensity of 2×10^{12} W/m^2, steel and aluminum will have a surface temperature of 4,800 K and 2400 K, respectively. These temperatures are above the melting point of each material and must be avoided. Note that even mirror-grade UV-enhanced aluminum with $R = 0.93$ [163] is insufficient because the absorptivity α of aluminum is high, and its effect on temperature is higher order than reflectivity R, as shown by Eqs. C.1.8 and C.1.11.

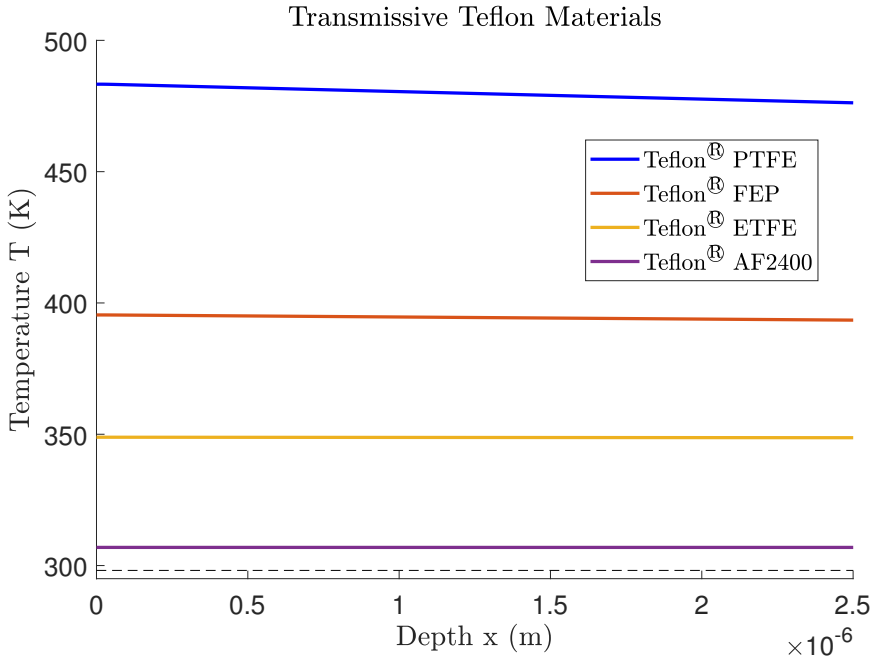

Figure C.3: Temperature Distribution in Four Teflon®Materials at a Pulse Energy of $3mJ$, beam fluence 9.5 J/cm^2, pulsewidth $\tau = 7$ ns, intensity 1.36×10^9 W/cm^2, and beam waist 200 μm produced with an $f = 300$ mm converging lens. These temperature distributions are calculated with Eq. C.1.8 at time $\tau = 7$ ns, with material parameters from Table C.1.

Using the performance parameter *Phi* (Eq. C.1.11) from Table C.1, PTFE,

FEP Teflon®and AF2400 Teflon®are good material candidates for protecting a test article surface. The temperature distribution is plotted for pure substrates in Fig. C.3. It becomes obvious that low absorptivity plays a larger role than reflectivity in reducing temperature within an optically penetrating substrate, like Teflon®. At a wavelength of 212.556 nm, AF2400 has a low absorptivity (high transmissibility) and high reflectivity, but it is not easy to obtain commercially. Therefore, it is necessary to omit it from further consideration.

The problem of thermal laser ablation should be negligible for the three consider Teflon®materials. However, there remains the problem of other nonlinear optical absorption and ionization mechanisms, namely multiphoton ionization at high intensities (10^{13} - 10^{14} J/cm^2 [80]). The Keldysh Parameter [81] for AF2400 exposed to linearly polarized 212.556 nm at an intensity of 1.7×10^9 W/cm^2 is

$$\gamma_K = \frac{\omega_L \sqrt{2 m_e E_{ion}}}{e E_L} = 750 \gg 1, \tag{C.1.13}$$

where ω_L is the laser angular frequency, m_e is the mass of the electron, e is the charge of an electron, E_{ion} is the first ionization energy of AF2400, and E_L is the applied laser electric field. At 1.7×10^9 W/cm^2, a Keldysh parameter much greater than one indicates that laser radiation on and in the substrate is within the perturbative and multiphoton regimes. Thus, experimentally-obtained laser induced damage thresholds (LIDT) should be considered in addition to thermal ablation.

C.2 Experimental Evaluation of Ablation Resistance of Teflon Materials

Three 25.4 μm (0.001 in) thick samples of Teflon®materials (PTFE, ETFE, and FEP Teflon®) were obtained from McMaster-Carr [164–166]. The supplier of AF2400 Teflon®, Random Technology [167], was not responsive, and therefore, AF2400

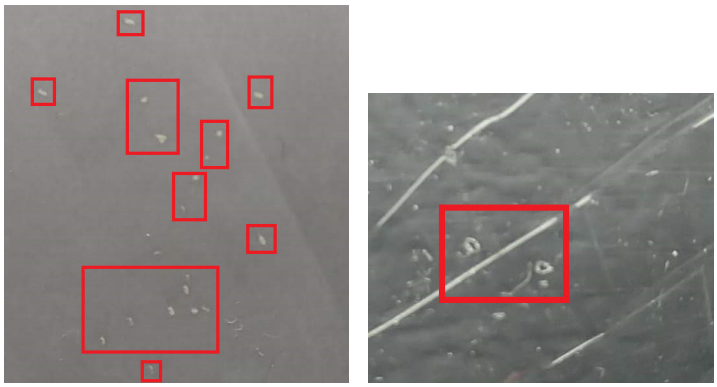

(a) 25.4 μm Thick PTFE

(b) 25.4 μm Thick FEP

(c) 25.4 μm Thick ETFE

(d) 127 μm Thick ETFE

Figure C.4: Ablated Surfaces of Teflon®Materials: (a) 25.4 μm thick PTFE, (b) 25.4 μm thick FEP, (c) 25.4 μm thick ETFE, (d) 127 μm thick ETFE.

Teflon®was excluded from the experimental laser ablation study. The three 25.4 μm (0.001 in) thick Teflon materials, were exposed to pulse trains consisting of twenty pulses of 212.556 nm laser light at 100 kHz focused via a 100 mm lens that generated an intensity of 10^{11} W/cm^2 and a fluence of 12.73 J/cm^2. The laser used was a Spectral Energies optical parametric oscillator (OPO) pumped via a Spectral Energies 100 kHz QuasiModo Pulse Burst Laser. Each pulse was approximately 1 mJ in energy and 7 ns in duration. The sample substrates were placed approximately at

the focus of the 100 mm lens.

Ablation results are displayed in Fig. C.4. The best material of the three was PTFE, which dispersed UV light and successfully mitigated multiphoton laser ablation. From Fig. C.4a, only thermal damage is observed on the surface. As shown by Fig. C.4b, FEP Teflon®was simply vaporized by the laser, as indicated by locations with empty holes, and ETFE Teflon®produced a large laser ablation plume, despite transmitting 20% of the laser pulse. ETFE exhibited chemical damage and burns at the surface, and ablation plumes for ETFE were larger than those for FEP. The inferior performance of ETFE and FEP is in contrast with the literature. Due to PTFE exhibiting the optimal behavior of the three materials, there must be additional dominant physics, which this work fails to model and predict. The scattering of light by PTFE is most interesting because it gives the impression that the material effectively increases the laser beam waist to about 12 mm and thereby decreases the effective fluence on the material substrate. In other words, PTFE diffuses 212.556 nm light. Additionally, the ablation plume over PTFE was notably smaller in diameter ($d < 1mm$) and height ($h < 1mm$) above the substrate than the plumes produced over other Teflon®grades. Negligible laser damage was observed over 25.4 μm thick PTFE material, making it a suitable shielding material for a test article that can help facilitate near-wall KTV investigations of boundary layers.

Bibliography

[1] J. D. Anderson, *Hypersonic and High Temperature Gas Dynamics*, 2nd ed. AIAA, 2011.

[2] L. M. Mack, "Linear stability theory and the problem of supersonic boundary-layer transition," *AIAA Journal*, vol. 13, no. 3, pp. 278–289, 1975.

[3] Y. Ma and X. Zhong, "Receptivity of a supersonic boundary layer over a flat plate. Part 1. Wave structures and interactions," *Journal of Fluid Mechanics*, vol. 488, pp. 31–78, 2003.

[4] J. J. Kuehl, "Thermoacoustic interpretation of second-mode instability," *AIAA Journal*, vol. 56, no. 9, pp. 3585–3592, 2018.

[5] M. S. Holden, T. P. Wadhams, and M. G. MacLean, "Measurements in Regions of Shock Wave/Turbulent Boundary Layer Interaction from Mach 4 to 10 at Flight Duplicated Velocities to Evaluate and Improve the Models of Turbulence in CFD Codes," CUBRC, Tech. Rep., 2014.

[6] J. D. Anderson, *Computational Fluid Mechanics: The Basics with Applications*. McGraw-Hill, Inc., 1995.

[7] F. White, *Viscous Fluid Flow*, 3rd ed. McGraw-Hill, 2006.

[8] C. Tropea, A. L. Yarin, and J. F. Foss, *Springer Handbook of Experimental Fluid Mechanics*. Springer, 2007.

[9] H. G. Hornung, "Experimental Hypervelocity Flow Simulation, Needs, Achievements and Limitations," in *Proceedings of the First Pacific International Conference on Aerospace Science and Technology*, Taiwan, 1993.

[10] F. K. Lu and D. E. Marren, *Advanced Hypersonic Test Facilities*. AIAA, 2002.

[11] S. P. Schneider, "Development of Hypersonic Quiet Tunnels," *Journal of Spacecraft and Rockets*, vol. 45, no. 4, pp. 641–664, 2008.

[12] P. M. Danehy, J. Weisberger, C. Johansen, D. Reese, T. Fahringer, N. J. Parziale, C. Dedic, J. Estevadeordal, and B. A. Cruden, "Non-Intrusive Measurement Techniques for Flow Characterization of Hypersonic Wind Tunnels," in *Flow Characterization and Modeling of Hypersonic Wind Tunnels (NATO Science and Technology Organization Lecture Series STO-AVT 325)*. Brussels, Belgium: NF1676L-31725 - Von Karman Institute, December 3-5 2018.

[13] D. Shekhtman, A. Hameed, B. A. Segall, A. R. Dworzanczyk, and N. J. Parziale, "Initial Shakedown Testing of the Stevens Shock Tunnel," in *Proceedings of AIAA SciTech 2022*. Virtual Event: AIAA 2022-1402, 3-7, January 2022.

[14] G. S. Settles, *Schlieren and Shadowgraph Techniques*, 1st ed. Springer-Verlag Berlin Heidelberg, 2001.

[15] L. Lester and M. Gragston, "Velocity, Mach Number, and Static Temperature Measurements in Supersonic Flows with 10 kHz Laser-Induced Schliere Anemometry," in *Proceedings of 2022 AIAA Scitech Forum*. San Diego, California: AIAA-2009-1287, 2022.

[16] J. S. Jewell, A. Hameed, N. J. Parziale, and S. P. Gogineni, "Disturbance Speed Measurements in a Circular Jet via Double Focused Laser Differential Interferometry," in *Proceedings of AIAA Scitech 2019*. San Diego, California: AIAA-2019-2293, 7-11 January 2019.

[17] A. Hameed and N. J. Parziale, "Focused Laser Differential Interferometry Transfer Functions for Complex Density Disturbance Fields," in *Proceedings of AIAA Aviation Forum 2021*. Virtual Event: AIAA-2021-2907, 2-6 August 2021.

[18] A. Hameed, D. Shekhtman, N. J. Parziale, L. A. Paquin, S. Skinner, S. J. Laurence, W. M. Yu, and J. M. Austin, "Hypersonic Boundary-Layer Instability on a Highly Cooled Cone. Part I: Q-FLDI Measurement and Instability Calculations," in *Proceedings of AIAA Scitech 2022*. San Diego, CA and Virtual Event: AIAA-2022-0734, 3-7 January 2022.

[19] W. G. Vincenti and C. H. Kruger, *Introduction to Physical Gas Dynamics*. Krieger Publishing Company, 1965.

[20] E. Loth, "Compressibility and Rarefaction Effects on Drag of a Spherical Particle," *AIAA Journal*, vol. 46, no. 9, pp. 2219–2228, 2008.

[21] K. T. Lowe, G. Byun, and R. L. Simpson, "The Effect of Particle Lag on Supersonic Turbulent Boundary Layer Statistics," in *Proceedings of AIAA SciTech 2014*. National Harbor, Maryland: AIAA-2014-0233, 2014.

[22] O. J. H. Williams, T. Nguyen, A.-M. Schreyer, and A. J. Smits, "Particle response analysis for particle image velocimetry in supersonic flows," *Physics of Fluids*, vol. 27, no. 7, p. 076101, 2015.

[23] J. M. Brooks, A. K. Gupta, M. S. Smith, and E. C. Marineau, "Particle image velocimetry measurements of Mach 3 turbulent boundary layers at low Reynolds numbers," *Experiments in Fluids*, vol. 59, p. 83, 2018.

[24] N. J. Parziale, M. S. Smith, and E. C. Marineau, "Krypton tagging velocimetry of an underexpanded jet," *Applied Optics*, vol. 54, no. 16, pp. 5094–5101, 2015.

[25] D. Zahradka, N. J. Parziale, M. S. Smith, and E. C. Marineau, "Krypton tagging velocimetry in a turbulent mach 2.7 boundary layer," *Experiments in Fluids*, vol. 57, p. 62, 2016.

[26] M. A. Mustafa, M. B. Hunt, N. J. Parziale, M. S. Smith, and E. C. Marineau, "Krypton Tagging Velocimetry (KTV) Investigation of Shock-Wave/Turbulent Boundary-Layer Interaction," in *Proceedings of AIAA SciTech 2017*. Grapevine, Texas: AIAA-2017-0025, 9-13 January 2017.

[27] M. A. Mustafa, , and N. J. Parziale, "Krypton Tagging Velocimetry in the Stevens Shock Tube," in *Proceedings of 33rd AIAA Aerodynamic Measurement Technology and Ground Testing Conference*. Denver, Colorado: AIAA-2017-3897, 5-9 June 2017.

[28] M. A. Mustafa, N. J. Parziale, M. S. Smith, and E. C. Marineau, "Nonintrusive Freestream Velocity Measurement in a Large-Scale Hypersonic Wind Tunnel," *AIAA Journal*, vol. 55, no. 10, pp. 3611–3616, 2017.

[29] ——, "Two-Dimensional Krypton Tagging Velocimetry (KTV-2D) Investigation of Shock-Wave/Turbulent Boundary-Layer Interaction," in *Proceedings of AIAA SciTech 2018*. Kissimmee, Florida: AIAA-2018-1771, 8-12 January 2018.

[30] M. A. Mustafa and N. J. Parziale, "Simplified read schemes for krypton tagging velocimetry in N_2 and air," *Optics Letters*, vol. 43, no. 12, pp. 2909–2912, 2018.

[31] M. A. Mustafa, N. J. Parziale, M. S. Smith, and E. C. Marineau, "Amplification and structure of streamwise-velocity fluctuations in compression-corner shock-wave/turbulent boundary-layer interactions," *Journal of Fluid Mechanics*, vol. 863, pp. 1091–1122, 2019.

[32] M. A. Mustafa, D. Shekhtman, and N. J. Parziale, "Single-Laser Krypton Tagging Velocimetry Investigation of Supersonic Air and N_2 Boundary-Layer Flows over a Hollow Cylinder in a Shock Tube," *Physical Review Applied*, vol. 11, no. 6, p. 064013, 2019.

[33] D. Shekhtman, M. A. Mustafa, and N. J. Parziale, "Two-photon cross-section calculations for krypton in the 190-220 nm range," *Applied Optics*, vol. 59, no. 34, pp. 10 826–10 837, 2020.

[34] A. G. Hsu, R. Srinivasan, R. D. W. Bowersox, and S. W. North, "Molecular Tagging Using Vibrationally Excited Nitric Oxide in an Underexpanded Jet Flowfield," *AIAA Journal*, vol. 47, no. 11, pp. 2597–2604, 2009.

[35] ——, "Two-component molecular tagging velocimetry utilizing NO fluorescence lifetime and NO_2 photodissociation techniques in an underexpanded jet flowfield," *Applied Optics*, vol. 48, no. 22, pp. 4414–4423, 2009.

[36] R. Sánchez-González, R. Srinivasan, R. D. W. Bowersox, and S. W. North, "Simultaneous velocity and temperature measurements in gaseous flow fields using the venom technique," *Optics Letters*, vol. 36, no. 2, pp. 196–198, 2011.

[37] R. Sánchez-González, R. D. W. Bowersox, and S. W. North, "Simultaneous velocity and temperature measurements in gaseous flowfields using the vibrationally excited nitric oxide monitoring technique: a comprehensive study," *Applied Optics*, vol. 51, no. 9, pp. 1216–1228, 2012.

[38] ——, "Vibrationally excited NO tagging by $NO(A^2\Sigma^+)$ fluorescence and quenching for simultaneous velocimetry and thermometry in gaseous flows," *Optics Letters*, vol. 39, no. 9, pp. 2771–2774, 2014.

[39] N. Dam, R. J. H. Klein-Douwel, N. M. Sijtsema, and J. J. ter Meulen, "Nitric oxide flow tagging in unseeded air," *Optics Letters*, vol. 26, no. 1, pp. 36–38, 2001.

[40] N. M. Sijtsema, N. J. Dam, R. J. H. Klein-Douwel, and J. J. ter Meulen, "Air Photolysis and Recombination Tracking: A New Molecular Tagging Velocimetry Scheme," *AIAA Journal*, vol. 40, no. 6, pp. 1061–1064, 2002.

[41] W. P. N. Van der Laan, R. A. L. Tolboom, N. J. Dam, and J. J. ter Meulen, "Molecular tagging velocimetry in the wake of an object in supersonic flow," *Experiments in Fluids*, vol. 34, no. 4, pp. 531–534, 2003.

[42] R. Miles, C. Cohen, J. Connors, P. Howard, S. Huang, E. Markovitz, and

G. Russell, "Velocity measurements by vibrational tagging and fluorescent probing of oxygen," *Optics Letters*, vol. 12, no. 11, pp. 861–863, 1987.

[43] R. Miles, J. Connors, E. Markovitz, P. Howard, and G. Roth, "Instantaneous profiles and turbulence statistics of supersonic free shear layers by Raman excitation plus laser-induced electronic fluorescence (RELIEF) velocity tagging of oxygen," *Experiments in Fluids*, vol. 8, no. 1-2, pp. 17–24, 1989.

[44] R. B. Miles, D. Zhou, B. Zhang, and W. R. Lempert, "Fundamental Turbulence Measurements by RELIEF Flow Tagging," *AIAA Journal*, vol. 31, no. 3, pp. 447–452, 1993.

[45] R. B. Miles and W. R. Lempert, "Quantitative Flow Visualization in Unseeded Flows," *Annual Review of Fluid Mechanics*, vol. 29, no. 1, pp. 285–326, 1997.

[46] R. B. Miles, J. Grinstead, R. H. Kohl, and G. Diskin, "The RELIEF flow tagging technique and its application in engine testing facilities and for helium-air mixing studies," *Measurement Science and Technology*, vol. 11, no. 9, pp. 1272–1281, 2000.

[47] J. B. Michael, M. R. Edwards, A. Dogariu, and R. B. Miles, "Femtosecond laser electronic excitation tagging for quantitative velocity imaging in air," *Applied Optics*, vol. 50, no. 26, pp. 5158–5162, 2011.

[48] M. R. Edwards, A. Dogariu, and R. B. Miles, "Simultaneous Temperature and Velocity Measurements in Air with Femtosecond Laser Tagging," *AIAA Journal*, vol. 53, no. 8, pp. 2280–2288, 2015.

[49] N. Jiang, B. R. Halls, H. U. Stauffer, P. M. Danehy, J. R. Gord, and S. Roy, "Selective two-photon absorptive resonance femtosecond-laser electronic-excitation tagging velocimetry," *Optics Letters*, vol. 41, no. 10, pp. 2225–2228, 2016.

[50] N. Jiang, J. G. Mance, M. N. Slipchenko, J. J. Felver, H. U. Stauffer, T. Yi, P. M. Danehy, and S. Roy, "Seedless velocimetry at 100 khz with picosecond-laser electronic-excitation tagging," *Optics Letters*, vol. 42, no. 2, pp. 239–242, 2017.

[51] J. L. Mills, "Investigation of Multi-Photon Excitation in Argon with Applications in Hypersonic Flow Diagnostics," Ph.D. dissertation, Old Dominion University, 2016.

[52] J. C. McDaniel, B. Hiller, and R. K. Hanson, "Simultaneous multiple-point velocity measurements using laser-induced iodine fluorescence," *Optics Letters*, vol. 8, no. 1, pp. 51–53, 1983.

[53] R. J. Balla, "Iodine Tagging Velocimetry in a Mach 10 Wake," *AIAA Journal*, vol. 51, no. 7, pp. 1–3, 2013.

[54] P. Barker, A. Bishop, and H. Rubinsztein-Dunlop, "Supersonic velocimetry in a shock tube using laser enhanced ionisation and planar laser induced fluorescence," *Applied Physics B*, vol. 64, no. 3, pp. 369–376, 1997.

[55] W. R. Lempert, N. Jiang, S. Sethuram, and M. Samimy, "Molecular Tagging Velocimetry Measurements in Supersonic Microjets," *AIAA Journal*, vol. 40, no. 6, pp. 1065–1070, 2002.

[56] W. R. Lempert, M. Boehm, N. Jiang, S. Gimelshein, and D. Levin, "Comparison of molecular tagging velocimetry data and direct simulation Monte Carlo simulations in supersonic micro jet flows," *Experiments in Fluids*, vol. 34, no. 3, pp. 403–411, 2003.

[57] T. Handa, K. Mii, T. Sakurai, K. Imamura, S. Mizuta, and Y. Ando, "Study on supersonic rectangular microjets using molecular tagging velocimetry," *Experiments in Fluids*, vol. 55, no. 5, pp. 1–9, 2014.

[58] S. Zhang, X. Yu, H. Yan, H. Huang, and H. Liu, "Molecular tagging velocimetry of NH fluorescence in a high-enthalpy rarefied gas flow," *Applied Physics B*, vol. 123, no. 4, p. 122, 2017.

[59] L. R. Boedeker, "Velocity measurement by H_2O photolysis and laser-induced fluorescence of OH," *Optics Letters*, vol. 14, no. 10, pp. 473–475, 1989.

[60] J. A. Wehrmeyer, L. A. Ribarov, D. A. Oguss, and R. W. Pitz, "Flame Flow Tagging Velocimetry with 193-nm H_2O Photodissociation," *Applied Optics*, vol. 38, no. 33, pp. 6912–6917, 1999.

[61] R. W. Pitz, M. D. Lahr, Z. W. Douglas, J. A. Wehrmeyer, S. Hu, C. D. Carter, K.-Y. Hsu, C. Lum, and M. M. Koochesfahani, "Hydroxyl tagging velocimetry in a supersonic flow over a cavity," *Applied Optics*, vol. 44, no. 31, pp. 6692–6700, 2005.

[62] M. A. André, P. M. Bardet, R. A. Burns, and P. M. Danehy, "Characterization of hydroxyl tagging velocimetry for low-speed flows," *Measurement Science and Technology*, vol. 28, no. 8, p. 085202, 2017.

[63] B. Hiller, R. A. Booman, C. Hassa, and R. K. Hanson, "Velocity visualization in gas flows using laser-induced phosphorescence of biacetyl," *Review of Scientific Instruments*, vol. 55, no. 12, pp. 1964–1967, 1984.

[64] C. P. Gendrich and M. M. Koochesfahani, "A spatial correlation technique for estimating velocity fields using molecular tagging velocimetry (MTV)," *Experiments in Fluids*, vol. 22, no. 1, pp. 67–77, 1996.

[65] C. P. Gendrich, M. M. Koochesfahani, and D. G. Nocera, "Molecular tagging velocimetry and other novel applications of a new phosphorescent supramolecule," *Experiments in Fluids*, vol. 23, no. 5, pp. 361–372, 1997.

[66] B. Stier and M. M. Koochesfahani, "Molecular tagging velocimetry (MTV) measurements in gas phase flows," *Experiments in Fluids*, vol. 26, no. 4, pp. 297–304, 1999.

[67] L. A. Ribarov, J. A. Wehrmeyer, F. Batliwala, R. W. Pitz, and P. A. DeBarber, "Ozone Tagging Velocimetry Using Narrowband Excimer Lasers," *AIAA Journal*, vol. 37, no. 6, pp. 708–714, 1999.

[68] M. A. André, R. A. Burns, P. M. Danehy, S. R. Cadell, B. G. Woods, and P. M. Bardet, "Development of N_2O-MTV for low-speed flow and in-situ deployment to an integral effect test facility," *Experiments in Fluids*, vol. 59, no. 1, p. 14, 2018.

[69] M. K. McIntosh, "Free Stream Velocity Measurements in a High Enthalpy Shock

Tunnel," *The Physics of Fluids*, vol. 14, no. 6, pp. 1100–1102, 1971.

[70] J. L. Wagner, E. P. DeMauro, K. M. Casper, S. J. Beresh, K. P. Lynch, and B. O. Pruett, "Pulse-burst PIV of an impulsively started cylinder in a shock tube for Re > 105," *Experiments in Fluids*, vol. 59, no. 6, p. 106, May 2018.

[71] R. A. Parker, T. Wakeman, M. MacLean, and M. Holden, "Measuring Nitric Oxide Freestream Velocity Using a Quantum Cascade Laser at CUBRC," in *Proceedings of 45th AIAA Aerospace Sciences Meeting and Exhibit*. Kissimmee, Florida: AIAA-2007-1329, 2007.

[72] P. M. Danehy, S. O'Byrne, A. F. P. Houwing, J. S. Fox, and D. R. Smith, "Flow-tagging Velocimetry for Hypersonic Flows using Fluorescence of Nitric Oxide," *AIAA Journal*, vol. 41, no. 2, pp. 263–271, 2003.

[73] P. A. de S. Matos, L. G. Barreta, and C. A. Martins, "Velocity and NO-Lifetime Measurements in an Unseeded Hypersonic Air Flow," *Journal of Fluids Engineering*, vol. 140, no. 12, p. 121105, 2018.

[74] Y. Zhang and R. B. Miles, "Femtosecond laser tagging for velocimetry in argon and nitrogen gas mixtures," *Optics Letters*, vol. 43, no. 3, pp. 551–554, 2018.

[75] C. A. Galea, C. A. Schneider, T. L. Chng, A. Dogariu, and R. B. Miles, "Radar REMPI Diagnostic for Low Neutral Density Measurements of Xenon in Helium Buffer Gas: Experiments and Modeling," in *Proceedings of the AIAA Aviation Forum 2018 Plasmadynamics and Lasers Conference*. Atlanta, Georgia: AIAA 2018-3435, 2018.

[76] N. N. Greenwood and A. Earnshaw, *Chemistry of the Elements*, 2nd ed. Butterworth-Heinemann, 1997.

[77] J. L. Mills, C. I. Sukenik, and R. J. Balla, "Hypersonic Wake Diagnostics Using Laser Induced Fluorescence Techniques," in *Proceedings of 42nd AIAA Plasmadynamics and Lasers Conference*. Honolulu, Hawaii: AIAA 2011-3459, 2011.

[78] R. J. Balla and J. L. Everhart, "Rayleigh Scattering Density Measurements, Cluster Theory, and Nucleation Calculations at Mach 10," *AIAA Journal*, vol. 50, no. 3, pp. 698–707, 2012.

[79] M. A. Mustafa, N. J. Parziale, M. S. Smith, and E. C. Marineau, "Amplification and structure of streamwise-velocity fluctuations in four shock-wave/turbulent boundary-layer interactions," in *Proceedings of AIAA Aviation 2018*. Atlanta, Georgia: AIAA-2018-3704, 25-29 June 2018.

[80] M. Anija, "Investigation of Nonlinear Effects Induced in Condensed Matter by Intense Electric Fields," Ph.D. dissertation, Raman, Research Institute, Jawaharlal Nehru University, Bangalore, India, 2007.

[81] I. V. Keldysh, "Ionization in the Field of a Strong Electromagnetic Wave," *Soviet Physics JETP*, vol. 20, no. 5, pp. 1307–1314, 1965.

[82] D. Shekhtman, W. M. Yu, M. A. Mustafa, N. J. Parziale, and J. M. Austin, "Freestream velocity-profile measurement in a large-scale, high-enthalpy reflected-shock tunnel," *Experiments in Fluids*, vol. 62, no. 118, pp. 1–13, 2021.

[83] M. A. Mustafa, D. Shekhtman, and N. J. Parziale, "Single-Laser Krypton Tagging Velocimetry (KTV) Investigation of Air and N2 Boundary-Layer Flows Over a Hollow Cylinder in the Stevens Shock Tube," in *Proceedings of AIAA Scitech 2019*. San Diego, California: AIAA-2019-1820, 7-11 January 2019.

[84] W. Grochala, L. Khriachtchev, and M. Rasanen, "Noble-gas chemistry," *Physics and Chemistry at Low Temperatures*, pp. 419–446, 2011.

[85] A. Kramida, Yu. Ralchenko, J. Reader, and and NIST ASD Team, NIST Atomic Spectra Database (ver. 5.5.6), [Online]. Available: https://physics.nist.gov/asd [2020, April 16]. National Institute of Standards and Technology, Gaithersburg, MD., 2020.

[86] D. Shekhtman, M. A. Mustafa, and N. J. Parziale, "Excitation Line Optimization for Krypton Tagging Velocimetry and Planar Laser-Induced Fluorescence in the 200-220 nm Range," in *Proceedings of AIAA SciTech 2021*. Virtual Event: AIAA-2021-1300, 11-15, 19-21 January 2021.

[87] N. Saito, Y. Oishi, K. Miyazaki, O. K., J. Nakamura, O. Louchev, M. Iwasaki, and S. Wada, "High-efficiency generation of pulsed Lyman-α radiation by resonant laser wave mixing in low pressure Kr-Ar mixture," *Optics Express*, vol. 24, no. 7, pp. 215–386, 2016.

[88] V. Fonseca and J. Campos, "Lifetimes of Some Levels Belonging to the $4p^5 5p$ and $4p^5 6p$ Configurations of Kr $_I$," *Physical Review A*, vol. 17, no. 3, pp. 1080–1082, 1978.

[89] E. Clementi and C. Roetti, "Roothaan-hartree-fock atomic wavefunctions: Basis functions and their coefficients for ground and certain excited states of neutral and ionized atoms, $z \leq 54$," *Atomic Data and Nuclear Data Tables*, vol. 14, no. 3-4, pp. 177–478, 1974.

[90] V. A. Kostelecký and M. M. Nieto, "Analytical wave functions for quantum-defect theory," *Physical Review A.*, vol. 32, no. 6, pp. 3243–3246, 1985.

[91] P. Lambropoulos, "Topics on Multiphoton Processes in Atoms," *Advances in Atomic and Molecular Physics*, vol. 12, pp. 87–164, 1976.

[92] H. A. Bethe and E. E. Salpeter, *Quantum Mechanics of One- and Two-Electron Atoms*. Springer-Verlag Academic Press, Inc., 1957.

[93] A. C. Eckbreth, *Laser Diagnostics for Combustion Temperature and Species*, 2nd ed. Gordon and Breach Publications, 1996.

[94] N. M. Khambatta, J. A. Oertel, R. Silk, L. J. Radziemski, and J. M. Mack, "Absolute excited state and ion densities from two-and three-photon processes in some 6p levels of atomic krypton," *Journal of Applied Physics*, vol. 64, no. 10, pp. 4809–4814, 1988.

[95] N. M. Khambatta, L. J. Radziemski, and S. N. Dixit, "Upper bound for a three-photon excitation cross section in atomic argon in the ultraviolet regime," *Physical Review A*, vol. 39, pp. 3842–3845, 1989.

[96] B. R. Marx, J. Simons, and L. Allen, "The effect of laser linewidth on two-photon absorption rates," *J. Phys. B: Atom. Molec. Phys*, vol. 11, no. 8, pp.

L273–L277, 1979.

[97] R. L. Liboff, *Introductory Quantum Mechanics*, 4th ed. Pearson Education, 2003.

[98] C. Park, *Nonequilibrium Hypersonic Aerothermodynamics*, 1st ed. John Wiley & Sons, 1990.

[99] O. A. Louchev, N. Saito, K. Miyazaki, K. Okamura, J. Nakamura, M. Iwasaki, and S. Wada, "Photoionization Pathways and Thresholds in Generation of Lyman-α Radiation by Resonant Four-Wave Mixing in Kr-Ar mixture," *AIP Advances*, vol. 6, no. 095018, pp. 1–10, 2016.

[100] W. Demtröder, *Atoms, Molecules, and Photons: An Introduction to Atomic-, Molecular, and Quantum-Physics*. Springer, 2006.

[101] A. Messiah, *Quantum Mechanics*. Dover Publications, Inc., 2014, Originally Published by John Wiley & Sons, NY, 1958.

[102] G. Hunter and I. Schlifer, "Explicit Spin Coordinates," *arXiv: Quantum Physics*, pp. 1–7, 2005.

[103] H. B. Bebb and A. Gold, "Multiphoton Ionization of Hydrogen and Rare-Gas Atoms," *Physical Review*, vol. 143, no. 1, pp. 1–24, 1966.

[104] E. J. McGuire, "Green's-function approach to nonresonance multiphoton absorption in the alkali-metal atoms," *Physical Review A.*, vol. 23, no. 1, pp. 186–200, 1981.

[105] ——, "Two- and three-photon ionization in the noble gases," *Physical Review A.*, vol. 24, no. 2, pp. 835–848, 1981.

[106] D. A. B. Miller, *Quantum Mechanics for Engineers and Scientists*. Cambridge University Press, 2008.

[107] R. C. Hillborn, "Einstein coefficients, cross sections, f values, dipole moments, and all that," *Am. J. of Phys.*, vol. 50, no. 11, pp. 982–986, 1981.

[108] D. R. Richardson, N. Jiang, H. U. Stauffer, S. P. Kearney, S. Roy, and J. R. Gord, "Mixture-fraction imaging at 1 kHz using femtosecond laser-induced fluorescence of krypton," *Optics Letters*, vol. 42, no. 17, pp. 3498–3501, 2017.

[109] S. W. Grib, P. S. Hsu, H. U. Stauffer, C. D. Carter, and S. Roy, "Comparison of femtosecond and nanosecond two-photon-absorption laser-induced fluorescence of krypton," *Applied Optics*, vol. 58, no. 27, pp. 7621–7627, 2019.

[110] M. A. Dakka, G. Tsiminis, R. D. Glover, C. Perrella, J. Moffatt, N. A. Spooner, R. T. Sang, P. S. Light, and A. N. Luiten, "Laser-based metastable krypton generation," *Phys. Rev. Lett.*, vol. 121, p. 093201, Aug 2018.

[111] T. O'Haver, *A Pragmatic Introduction to Signal Processing*. University of Maryland at College Park, 1997.

[112] L. Alves, P. Coche, M. A. Ridenti, and V. Guerra, "Electron Scattering Cross Sections for the Modelling of Oxygen-Containing Plasmas," *European Journal of Physics*, vol. 70, no. 124, pp. 1–9, 2016.

[113] Y. Itikawa, K. Ichimura, O. K. Sakimoto, and K. Takayanagi, "Cross Sections for Collisions of Electrons and Photon with Oxygen Molecules," *Journal of*

Phys. Chem. Ref. Data, vol. 18, no. 1, pp. 23–42, 1989.

[114] R. J. Stalker, "Hypervelocity Aerodynamics with Chemical Nonequilibrium," *Annual Review of Fluid Mechanics*, vol. 21, pp. 37–60, 1989.

[115] G. V. Candler, "Rate-dependent energetic processes in hypersonic flows," *Progress in Aerospace Sciences*, vol. 72, pp. 37–48, 2015.

[116] ——, "Rate Effects in Hypersonic Flows," *Annual Review of Fluid Mechanics*, vol. 51, pp. 379–402, 2019.

[117] I. A. Leyva, "The relentless pursuit of hypersonic flight," *Physics Today*, vol. 70, no. 11, pp. 30–36, 2017.

[118] H. G. Hornung, "Performance Data of the New Free-Piston Shock Tunnel at GALCIT," in *Proceedings of 17th AIAA Aerospace Ground Testing Conference*. Nashville, TN: AIAA 1992-3943, 1992.

[119] D. G. Goodwin, "An Open-Source, Extensible Software Suite for CVD Process Simulation," in *Proceedings of CVD XVI and EuroCVD Fourteen, M Allendorf, F Maury, and F Teyssandier (Eds.)*, 2003, pp. 155–162.

[120] S. Browne, J. Ziegler, and J. E. Shepherd, "Numerical Solution Methods for Shock and Detonation Jump Conditions," Caltech, GALCIT - FM2006-006, 2006.

[121] S. Gordon and B. McBride, "Thermodynamic Data to 20000 K for Monatomic Gases," NASA TP-1999-208523, 1999.

[122] B. J. McBride, M. J. Zehe, and S. Gordon, "NASA Glenn Coefficients for Calculating Thermodynamic Properties of Individual Species," NASA TP-2002-211556, 2002.

[123] M. J. Wright, G. V. Candler, and M. Prampolini, "Data-parallel Lower-upper Relaxation Method for the Navier-Stokes Equations," *AIAA Journal*, vol. 34, no. 7, pp. 1371–1377, 1996.

[124] G. V. Candler, "Hypersonic Nozzle Analysis Using an Excluded Volume Equation of State," in *Proceedings of 38th AIAA Thermophysics Conference*. Toronto, Ontario Canada: AIAA-2005-5202, 2005.

[125] H. B. Johnson, "Thermochemical interactions in hypersonic boundary layer stabity," Ph.D. dissertation, University of Minnesota, Minneapolis , Minnesota, 2000.

[126] R. M. Wagnild, "High enthalpy effects on two boundary layer disturbances in supersonic and hypersonic flow," Ph.D. dissertation, University of Minnesota, Minnesota, 2012.

[127] N. Sudani and H. G. Hornung, "Gasdynamical Detectors of Driver Gas Contamination in a High-Enthalpy Shock Tunnel," *AIAA*, vol. 36, no. 3, pp. 313–319, 1998.

[128] N. Sudani, B. Valiferdowsi, and H. G. Hornung, "Test Time Increase by Delaying Driver Gas Contamination for Reflected Shock Tunnels," *AIAA*, vol. 38, no. 9, pp. 1497–1503, 2000.

[129] MathWorks, "Matlab wiener2," www.mathworks.com, 2022, accessed: 2022-02-

13.

[130] S. Kumar, P. Kumar, M. Gupta, and A. K. Nagawat, "Performance comparison of median and wiener filter in image de-noising," *International Journal of Computer Applications*, vol. 14, no. 4, pp. 27–31, 2010.

[131] M. S. Rzeszotarski, F. L. Royer, and G. C. Gilmore, "Review and assessment of turbulence models for hypersonic flows," *Behavior Research Methods & Instrumentation*, vol. 15, no. 2, pp. 308–318, 1983.

[132] L. G. Shapiro and G. C. Stockman, *Computer Vision*, 1st ed. Pearson Education, 2001.

[133] B. F. Bathel, P. M. Danehy, J. A. Inman, S. B. Jones, C. B. Ivey, and C. P. Goyne, "Velocity Profile Measurements in Hypersonic Flows Using Sequentially Imaged Fluorescence-Based Molecular Tagging," *AIAA Journal*, vol. 49, no. 9, pp. 1883–1896, 2011.

[134] R. B. Hill and J. C. Klewicki, "Data reduction methods for flow tagging velocity measurements," *Experiments in Fluids*, vol. 20, no. 3, pp. 142–152, 1996.

[135] C. K. Chui and Q. Jiang, "Data Compression," in *Applied Mathematics: Data Compression, Spectral Methods, Fourier Analysis, Wavelets, and Applications*, ser. Mathematics Textbooks for Science and Engineering, C. K. "Chui, Ed. Springer Nature: Atlantis Press, 2013, vol. 2.

[136] W. A. H. Jumiawi and A. El-Zaart, "Image Spectrum Segmentation for Low-pass and Highpass Filters," in *4th International Conference on Applied and Theoretical Computing and Communication Technology (iCATccT)*. Chicago, Illinois: IEEE, 2018, pp. 1–6.

[137] A. González-Díez, J. A. Barreda-Argüeso, L. Rodríguez-Rodríguez, and J. Fernández-Lozano, "The use of filters based on the fast fourier transform applied to dems for the objective mapping of karstic features," *Geomorphology*, vol. 385, pp. 1–19, 2021.

[138] N. J. Parziale, J. E. Shepherd, and H. G. Hornung, "Free-stream density perturbations in a reflected-shock tunnel," *Experiments in Fluids*, vol. 55, no. 2, p. 1665, 2014.

[139] J. S. Jewell, N. J. Parziale, I. A. Leyva, and J. E. Shepherd, "Effects of Shock-Tube Cleanliness on Hypersonic Boundary Layer Transition at High Enthalpy," *AIAA Journal*, vol. 55, no. 1, pp. 332–338, 2017.

[140] P. F. Logan, R. J. Stalker, and M. K. McIntosh, "A shock tube study of radiative energy loss from an argon plasma," *Journal of Physics D: Applied Physics*, vol. 10, no. 3, pp. 323–337, 1977.

[141] C. E. Wittliff, M. R. Wilson, and A. Hertzberg, "The Tailored-Interface Hypersonic Shock Tunnel," *Journal of the Aerospace Sciences*, vol. 26, no. 4, pp. 219–228, 1959.

[142] N. J. Parziale, "Slender-Body Hypervelocity Boundary-Layer Instability," Ph.D. dissertation, California Institute of Technology, 2013.

[143] J. S. Jewell, "Boundary-layer transition on a slender cone in hypervelocity flow

with real gas effects," Ph.D. dissertation, California Institute of Technology, 2014.

[144] S. W. Grib, N. Jiang, P. S. Hsu, H. U. Stauffer, J. J. Felver, S. Roy, and S. A. Schumaker, "100 khz krypton-based flow tagging velocimetry in a high-speed flow," *Applied Optics*, vol. 60, no. 6, pp. 1615–1622, 2021.

[145] L. Pauling and J. Wilson, E. B. *Introduction to Quantum Mechanics with Applications to Chemistry.* Dover Publications, Inc., 1985.

[146] Newport Corporation. (2021) Gaussian beam optics. Accessed: 2022-01-12. [Online]. Available: https://www.newport.com/n/gaussian-beam-optics

[147] D. G. Zill and W. S. Wright, *Differential Equations with Boundary-Value Problems*, 8th ed. Cenage Learning, 2013.

[148] C. Mack, *Fundamental Principles of Optical Lithography: The Science of Microfabrication.* John Wiley & Sons, 2007.

[149] J. H. Bechtel, "Heating of solid targets with laser pulses," *Journal of Applied Physics*, vol. 46, no. 4, pp. 1585–1593, April 1975.

[150] D. Sands, "Pulsed Laser Heating and Melting," *InTechOpen*, pp. 47–70, 2011.

[151] Matweb, LLC. Matweb: Material Property Data. [Online]. Available: http://www.matweb.com/

[152] Cystran: UV, Visible, IR Specialist, Optics. (2021) Optical materials. [Online]. Available: https://www.crystran.co.uk/optical-materials

[153] C. Silva, ""PTFE Reflectance Measurements, Modeling and Simulation for Xenon Detectors"," in *Proceedings of LIP.* Chicago, USA: "CERN", 2011.

[154] S. Küper and M. Stuke, "Ablation of polytetrafluoroethylene (Teflon) with femtosecond UV excimer laser pulses," *App. Phys. Lett.*, vol. 54, no. 1, pp. 4–6, 1989.

[155] *Teflon FEP: Fluoropolymer Resin Product and Properties Handbook*, DuPont, USA, 2018.

[156] J. A. Dever and C. A. McCracken, "Effects of Various Wavelength Ranges of Vacuum Ultraviolet Radiation on Teflon ®FEP Film," in *Proceedings of the 9th International Symposium on Materials in a Space Environment*, no. ESA SP-540. Noordwijk, The Netherlands: ESA, 2003.

[157] P. Resnick and W. H. Buck, *Teflon® AF Amorphous Fluoropolymers.* Berlin, Heidelberg: John Wiley and Sons Ltd, 2008, pp. 397–419.

[158] M. K. Yang, R. H. French, and E. W. Tokarsky, "Optical Properties of Teflon ®AF Amorphous Fluoropolymers," *J. MicroNanolith. MEMS MOEMS*, vol. 7, no. 3, pp. 1–9, 2008.

[159] Fluorotherm. (2022) Etfe properties. [Online]. Available: https://www.fluorotherm.com/technical-information/materials-overview/etfe-properties/

[160] R. H. French, J. M. Rodréguez-Parada, M. K. Yang, R. A. Derryberry, M. F. Lemon, M. J. Brown, C. R. Haegar, S. L. Samuel, E. C. Romano, and R. E. Richardson, "Optical Properties of Materials for Concentrator Photovoltaic Systems," in *2009 34th IEEE Photovoltaic Specialists Conference (PVSC)*, vol. 17,

no. 3. Philadelphia, PA, USA: IEEE, 2009, pp. 00 394–00 399.

[161] M. M. Quazi, M. A. Fazal, A. S. M. A. Haseeb, M. Yusof, H. H. Masjuki, and A. Arslan, "Laser-based Surface Modifications of Aluminum and its Alloys," *Critical Reviews in Solid State and Material Sciences*, vol. 41, pp. 106–131, 2015.

[162] Thorlabs. (2021) UV Fused Silica High-Precision Windows. Accessed: 2022-01-12. [Online]. Available: http://www.https://www.thorlabs.com/

[163] Edmund Optics. (2021) Metallic mirror coatings. [Online]. Available: https://www.edmundoptics.com/knowledge-center/application-notes/optics/metallic-mirror-coatings/

[164] McMaster-Carr. (2022) Chemical-Resistant Slippery Film Made from Teflon®PTFE. Accessed: 2022-01-12. [Online]. Available: https://www.mcmaster.com/ptfe/shape~film/

[165] ——. (2022) Clear High-Strength High-Temperature ETFE Film. Accessed: 2022-01-12. [Online]. Available: https://www.mcmaster.com/etfe/

[166] ——. (2022) Clear Slippery High-Temperature FEP Film. Accessed: 2022-01-12. [Online]. Available: https://www.mcmaster.com/fep/

[167] Random Technology. (2021) Teflon®AF: Random Technologies LLC is a Manufacturer of Teflon AF products and is a DuPont licensed Teflon AF fabricator. [Online]. Available: http://www.randomtechnologies.com/

Vita

David Shekhtman

Address 250 Gorge Road Apt. 6-F, Cliffside Park, NJ 07010

Place of birth NJ, USA

Contact Email: davshe98@gmail.com

Education

Stevens Institute of Technology, Hoboken, NJ
Doctoral Candidate in Mechanical Engineering
expected date of graduation, May 2022

The Cooper Union for the Adv. of Science and Art, NY, NY
Masters of Engineering in Mechanical Engineering
Master's thesis: Preventing Ship Capsize with a Pendulum Actuator
May, 2018. GPA: 4.00
Bachelor of Engineering in Mechanical Engineering
May, 2016. GPA: 3.88

Experience

Stevens Ph.D. Researcher (July 2018-Present):
-Conducted Krypton-Tagging-Velocimetry (KTV) experiments in freestream and boundary layer flow in supersonic and hypersonic impulse facilities: over a sectioned hollow cylinder (1200 m/s); and in the T5 Caltech Freestream (16 MJ/kg enthalpy and 4700 m/s).
-Designed a hollow cylinder flare in the Stevens Shock Tunnel with instrumentation for over 50 transducers for KTV and transition experiments at Stevens and NASA LARC.
-Designed support structure, diaphragm rupturing mechanisms, and the 24 in diameter test section of the Mach 6, 1.8 MJ/kg Stevens Shock Tunnel.

NASA LARC NEA Scout Internship in Systems Integration
Intern (Summer 2016):
-Participated in all levels of the design process: design, assembly, testing, diagnostics
-Assembled and tested a solar sail deployer;
conducted thermal expansion analyses for drive train;
described length discrepancy between sail booms;
learned Creo Parametric

Teaching Assistant at The Cooper Union
(Spring 2015, Spring 2017):
Developed a key curriculum activity for Design and Prototyping
Enhanced the skills of students with a sheet metal design project

Publications

Shekhtman, D. and Luchtenburg, D. M., "Seven Degrees-of-Freedom Model for the Roll Stabilization of Unstable Ships," Journal of Dynamic Systems, Measurement and Control, Transactions of the ASME, Vol. 141, No. 8, pp. 1–9, 2019. doi: 10.1115/1.4042950.

Mustafa, M. A., Shekhtman, D., and Parziale, N. J., "Single-Laser Krypton Tagging Velocimetry Investigation of Supersonic Air and N2 Boundary-Layer Flows over a Hollow Cylinder in a Shock Tube," Physical Review Applied, Vol. 11, No. 6, 2019, pp. 064013. doi: 10.1103/PhysRevApplied.11.064013.

Shekhtman, D., Mustafa, M. A., and Parziale, N. J., "Two-photon cross-section calculations for krypton in the 190-220 nm range," Applied Optics, Vol. 59, No. 34, 2020, pp. 10826–10837. doi: 10.1364/AO.410806.

Shekhtman, D., Yu, W. M., Mustafa, M. A., Parziale, N. J., and Austin, J. M., "Freestream velocity-profile measurement in a large-scale, high-enthalpy reflected-shock tunnel," Experiments in Fluids, Vol. 62, No. 118, 2021, pp. 1–13. doi: 10.1007/s00348-021-03207-6.

Confer. Papers

Shekhtman, D., Mustafa, M. A., and Parziale, N. J., "Excitation Line Optimization for Krypton Tagging Velocimetry and Planar Laser-Induced Fluorescence in the 200-220 nm Range," Proceedings of AIAA SciTech 2021, AIAA-2021-13001300, Virtual Event, 11-15, 19-21 January 2021.

Shekhtman, D., Mustafa, M. A., Parziale, N. J., Yu, W. M., and Austin, J. M.,"Krypton Tagging Velocimetry (KTV) Investigation in the Caltech T5 Reflected-Shock Tunnel," Proceedings of AIAA SciTech 2021, AIAA-2021-1302, Virtual Event, 11-15, 19-21 January 2021.

Shekhtman, D. and Parziale, N. J.,
"Input-Output Stability Analysis of a Flat-Plate, High-Speed Flow," Proceedings of AIAA Aviation Forum 2021, AIAA-2021-2934, Virtual Event, 2-6 August 2021.

Shekhtman, D., Hameed, A., Segall, B. A., Dworzanczyk, A. R., and Parziale, N. J. "Initial Shakedown Testing of the Stevens Shock Tunnel," Proceedings of AIAA SciTech 2021, AIAA-2022-1402, Virtual Event, 3-7 January 2022.

Honors

Mechanical Engineering Design Prize for Excellence in Mechanical Design, Cooper Union, May, 2016